



저작자표시-비영리-변경금지 2.0 대한민국

이용자는 아래의 조건을 따르는 경우에 한하여 자유롭게

- 이 저작물을 복제, 배포, 전송, 전시, 공연 및 방송할 수 있습니다.

다음과 같은 조건을 따라야 합니다:



저작자표시. 귀하는 원저작자를 표시하여야 합니다.



비영리. 귀하는 이 저작물을 영리 목적으로 이용할 수 없습니다.



변경금지. 귀하는 이 저작물을 개작, 변형 또는 가공할 수 없습니다.

- 귀하는, 이 저작물의 재이용이나 배포의 경우, 이 저작물에 적용된 이용허락조건을 명확하게 나타내어야 합니다.
- 저작권자로부터 별도의 허가를 받으면 이러한 조건들은 적용되지 않습니다.

저작권법에 따른 이용자의 권리는 위의 내용에 의하여 영향을 받지 않습니다.

이것은 [이용허락규약\(Legal Code\)](#)을 이해하기 쉽게 요약한 것입니다.

[Disclaimer](#)

공학박사 학위논문

Investigation of Generalized Bohm Sheath Criterion for Collisional, Magnetized and RF Plasmas

충돌성, 자화, RF 플라즈마에 대한
일반화된 Bohm 쉬스 경계조건 해석

2019 년 2 월

서울대학교 대학원

에너지시스템공학부

김 남 균

Investigation of Generalized Bohm Sheath Criterion for Collisional, Magnetized and RF Plasmas

지도 교수 김 곤 호

이 논문을 공학박사 학위논문으로 제출함
2018 년 12 월

서울대학교 대학원
에너지시스템공학부
김 남 균

김남균의 박사 학위논문을 인준함
2018 년 12 월

위 원 장 _____ 황 용 석 _____ (인)

부위원장 _____ 김 곤 호 _____ (인)

위 원 _____ 정 경 재 _____ (인)

위 원 _____ 노 태 협 _____ (인)

위 원 _____ 김 영 철 _____ (인)

Abstract

Investigation of Generalized Bohm Sheath Criterion for Collisional, Magnetized and RF Plasmas

Nam-Kyun Kim

Department of Energy Systems Engineering

The Graduate School

Seoul National University

Investigations of generalized Bohm sheath criterion have been carried out for collisional, magnetized and RF plasmas. Near the almost every surface that faces the quasi-neutral plasma, there forms a plasma sheath in between the plasma and the plasma-facing wall. A strong electric field is formed in the region in the direction from the plasma to the wall, and the losses of the electrons and the ions form a balance to maintain the quasi-neutral plasma condition. In order to form the plasma sheath, Bohm suggested a criterion that the ion fluid velocity should be larger than $V_{Bohm} = \sqrt{k_B T_e / m_i}$ at the sheath entrance. The criterion is called the Bohm criterion and it is widely used to determine the ion flux toward the wall surface. But the criterion was derived under the assumptions of collision-less, singly-ionized, single-ion-species, cold ions, and magnetic-field free conditions. In various practical plasmas, those assumptions are not applicable. In this study we have generalized the Bohm sheath criterion without any artificial approximation on the plasma conditions. Collisions between the ions and the neutral species, collision between two-different ion species, existence of oblique magnetic fields, and

the change of the ion velocity distribution itself have been considered. By using a fluid moment approach, the Bohm sheath criterion can be modified to more generalized form that considers general ion dynamic characteristic and the effect of external magnetic field. To investigate the effect of the above-mentioned conditions on the generalized Bohm sheath criterion, we observed the ion dynamic properties and the electric potential distribution in the ion-neutral / ion-ion collisional, magnetized and RF plasma, especially near the sheath boundary region, which is called the presheath. For the observation of the ion motion, a laser-induced-fluorescence method is utilized. The space potential distribution is measured by using the emissive probe. From the observation we have characterized the ion dynamic properties and the role of the presheath potential drop on the formation of the sheath entrance condition. By considering the ion dynamic characteristics we observed in this thesis, the generalized Bohm sheath criterion have been qualitatively analyzed. The analysis reveals that in order to form a plasma sheath in a highly collisional, strongly magnetized, or highly damped plasma the ion velocity at the sheath edge must have modified from the original Bohm velocity.

Keywords: generalized Bohm criterion, plasma sheath, presheath, collision, magnetic field, radio-frequency electrostatic wave
Student Number: 2013-30993

Contents

Abstract.....	i
Contents	iii
List of tables.....	vi
List of figures	vii
Chapter 1. Introduction	1
1.1. Bohm criterion for sheath formation	1
1.2. Universal sheath condition on charge density	4
1.3. Previous studies on generalization of Bohm criterion	8
1.4. Generalization of Bohm sheath criterion by ion dynamics ...	12
1.5. Ion dynamics in presheath of collisional, magnetized, and RF plasmas	16
Chapter 2. Previous studies on ion dynamics in collisional, magnetized and RF sheath	18

2.1. Effect of two-stream-instability-enhanced (TSI) ion-ion collision on Bohm sheath criterion	18
2.1.1. Effect of two-stream-instability on ion motion in presheath	18
2.1.2. Generalized occurrence condition of two-stream-instability under ion-neutral collision	22
2.2. Effect of oblique magnetic field on ion motion in sheath and presheath	25
2.2.1. Fluidic description of ion motion in magnetic sheath and presheath	28
2.2.2. Magnetized and weakly-collisional presheath	31
2.2.3. Debye Sheath	32
2.3. Landau damping of electrostatic wave travelling against ion flow	33
Chapter 3. Experimental Setup	37
3.1. Plasma sources	37
3.1.1. Multi-dipole plasma source	37
3.1.2. Electron-cyclotron-resonance plasma source	42
3.2. Emissive probe for sheath potential measurement	48
3.3. Laser-induced-fluorescence ion velocity measurement	57
3.4. Material probe for ion incident angle measurement	69

3.5. Ion acoustic wave measurement for ion concentration	72
Chapter 4. Characteristics of ion dynamics in presheath of collisional plasmas	75
4.1. Characteristic of ion dynamics in ion-neutral collisional presheath	75
4.2. Characteristic of ion dynamics in ion-ion collisional presheath under existence of ion-neutral collision	81
4.3. Characteristic of electric potential in collisional presheath...	87
4.4. Summary	88
Chapter 5. Characteristics of ion dynamics in presheath of magnetized plasmas	89
5.1. Validation of theoretical magnetic sheath model	89
5.2. Characteristic of ion dynamics in magnetic presheath	91
5.3. Characteristics of electric potential of magnetic presheath...	97
5.5. Summary	100

Chapter 6. Characteristics of ion dynamics in presheath of RF plasmas	101
6.1. Variation of IVDF under DC presheath electric field	101
6.2. Variation of longitudinal IVDF by electrostatic wave in presheath	105
6.3. Characteristic of ion dynamics and electric potential in RF presheath	108
6.4. Summary	110
 Chapter 7. Conclusion	 111
 Bibliography	 118
 국문초록	 125

List of Tables

Table 1.1.	Meaning of ion-dynamic-related modification terms on Bohm criterion.....	17
Table 3.1.	Summary on the characteristics of multi-dipole plasma source	41
Table 3.2.	Plasma parameters of ECR plasma source used in this study	45
Table 3.3.	Characteristics of the floating-point method and inflection-point method	54
Table 3.4.	Various LIF schemes used for ion velocity measurement [57]	58
Table 3.5.	Lifetime of argon ion metastable state	59
Table 3.6.	Comparison between dye laser and diode laser	60
Table 4.1.	Plasma parameters	82
Table 7.1.	Characteristics of ion dynamic, spatial and electric properties in presheaths of collisional, magnetized and rf plasmas.	114

**Table 7.2. Scale laws for characterization of the generalized Bohm criterion by ion dynamic properties.
..... 116**

List of Figures

- Figure 1.1.** Shielding positive sheath in front of a negative wall [1] 1
- Figure 2.2.** Schematic diagram of ion fluid velocity profiles through the presheath. When the relative velocity between two-ion-species becomes larger than a critical relative velocity, the instability-enhanced friction modifies the ion motion near the sheath edge. Therefore, the ions have a modified Bohm velocity at the sheath edge [14] 20
- Figure 2.3.** Modified ion velocity at the sheath edge of Ar/Xe mixture plasmas. As the argon and xenon ion densities become comparable, the two-stream-instability-enhanced-collisional-friction significantly modifies the sheath entrance velocity of each ion-species. 21
- Figure 2.4.** Pressure threshold of the instability with respect to the electron temperature calculated from Eq. (2.4), considering ion-neutral collisions (red-solid line). The region above the line is a stable region where the instability does not occur and the region below the line is the unstable region where the instability occurs. Experimental conditions, which are taken in the investigation (chapter 4) are marked with crosses. .. 24
- Figure 2.5.** (a) The reference frame, Oxyz, used in the model and the configuration of the magnetic field. The incident angle of the magnetic field is defined as the angle between the magnetic field line and the surface normal. (b) A schematic configuration of the plasma structure near a wall surface.

	The origin, O, of the reference frame in (a) corresponds to the position, PE (plasma edge), in (b).	28
Figure 2.6.	Comparison of the ion density of argon plasma with the ion plasma frequency.	34
Figure 3.1.	A multi-dipole plasma source. Energetic electrons emitted from hot filament wires are confined by the magnetic cusp fields around the chamber and forms a homogeneous density region. A RF or DC biased target is located at one edge of the homogeneous region to form a sheath configuration.	38
Figure 3.2.	Radial density profile of electron and ions in the multi-dipole chamber. The experiment region was assigned to the uniform-density region of $r < 8$ cm.	40
Figure 3.3.	A schematic diagram of electron-cyclotron-resonance (ECR) plasma source. A 2.45 GHz microwave is injected through the upper window and makes resonance at $B = 875$ gauss surface. There exists a uniform density region at $r < 2$ cm and a 3.5-cm-diameter target holder is located in the region.	43
Figure 3.4.	A configuration of typical magnetic field line in ECR plasma source. The geometrical divergence of the central ($r < 2$ cm) field line is less than 2 degree near the source chamber – diffusion chamber interface.	44
Figure 3.5.	A side view and a front view of the target holder. In this figure, the magnetic field angle, ψ , is 80° which forms an	

grazing angle with the tangential direction of the target surface. .. 46

- Figure 3.6. Equipotential contours near a 0.5-cm-diameter planar Langmuir probe biased at 0 V. The probe was positioned 0.6 cm from a plate biased at -50 V. It shields out the sheath electric field of the plate and perturb the potential profile. [51] 49
- Figure 3.7. Typical I-V (current-voltage) characteristic curve obtained by an emissive probe. The curve consists of the collection current, originated from the incidental flux of the charged particles in the plasma, and the emission current. [55] 50
- Figure 3.8. Floating-point method for the measurement of space potential. As the emission increases, the floating potential of the I-V characteristic curve of the emissive probe goes toward and saturates at the space potential. [56] 51
- Figure 3.9. The inflection-point method (IPM) for the determination of the plasma potential. The inflection-point of the derivative of the I-V characteristic curve tend to decrease as the emission current increases. 53
- Figure 3.10. The inflection-point method operated in the limit of zero-emission [55]. As the saturation current of emission current (I_{e0}) to the saturation current of collection current (I_{c0}) decreases, the inflection point goes toward the plasma potential. 53
- Figure 3.11. Circuit diagram of (lower) the heating current supplier for the emissive probe and (upper) the I-V characteristic measurement circuit board. All the control of heating current, sweeping voltage and measurement of I-V were

controlled by a Labview®-based lab-made software. A noise reduction filter was used to supply a noise-free power to the operational amplifiers.

..... 55

Figure 3.12. Examples of typical curve obtained by emissive probes. By applying a noise reduction circuit to the power supplier for operational amplifier, much higher signal-to-noise ratio can be achieved even at lower emission current. 56

Figure 3.13. Ar+ ion LIF scheme used in this research. 62

Figure 3.14. Xe+ LIF scheme used in this research [60]. 62

Figure 3.15. Efficiency of dye laser with using a combination of Rhodamine B and Rhodamine 640 dye solution 63

Figure 3.16. Experimental apparatus for the laser-induced-fluorescence ion velocity measurement by using a tunable diode laser. Because of the weak laser power (~ 10 mJ), the laser is modulated to the chopper frequency and the modulated LIF signal is amplified by using a lock-in-amplifier.65

Figure 3.17. Experimental apparatus for the laser-induced-fluorescence ion velocity measurement by using a tunable dye laser. For the use of a high-power pulsed dye laser the LIF signal was averaged in a oscilloscope to achieve high signal-to-noise ratio, which corresponds to the boxcar average method....66

Figure 3.18. Optical detection module used for LIF measurement in our experiment. By using aspheric lenses, spatial resolution can

be achieved. A slit (0.3 mm × 3 mm) can be used instead of pinhole and it enhances signal-to-noise ratio without changing 1-dimensional spatial resolution along the target axis. 67

Figure 3.19. Scanning electron microscope (SEM) images of the surface of (a) pristine, (b) helium ion irradiated, and (c) hydrogen ion irradiated graphite targets. Images are taken with the tilt angle of 30° with respect to surface normal direction.69

Figure 3.20. Scanning electron microscope images taken in two orthogonal directions. The tilt angle of nano-scaled tips, can be obtained from the seeming tilt angles that are taken at two orthogonal imaging directions. 71

Figure 3.21. A schematic diagram of the multi-dipole plasma source and the ion acoustic wave measurement system. The plasma is generated by the energetic primary electrons, emitted from negatively biased hot filaments. The ion acoustic wave launcher and receiver are installed inside the uniform bulk plasma. 73

Figure 3.22. Ion acoustic wave measurement. (a) The signal of the ion acoustic wave received at various positions near the wave launcher and (b) the arrival time of the ion acoustic wave vs. the position of the receiver from the wave launcher. Data were obtained from the Ar/Xe (= 50/50) mixture gas discharged plasma. The arrival time of the ion acoustic wave was determined by the arrival time of the peak signal. The common system sound velocity is obtained from the

	slope of the graph. 74
Figure 4.1.	Spatial profile of the ion drift velocity and space potential obtained in a pure argon plasma. 77
Figure 4.2.	Normalized potential versus kinetic energy of ions in presheath. 80
Figure 4.3.	Spatial distribution of argon and xenon ions' velocity and their relative velocity for pressure conditions of ((a) and (b)) 0.52 mTorr, ((c) and (d)) 0.73 mTorr, ((e) and (f)) 1.04 mTorr, and ((g) and (h)) 2.1 mTorr. 84
Figure 4.4.	Drift velocities of argon and xenon ions normalized by individual own Bohm velocity. 86
Figure 4.5.	Characteristic wavelength of the instability with (solid-red- line) and without (dotted-blue-line) the consideration of the ion-neutral collisions. Unfilled (-black) squares represent the experimental length of the instability region. 87
Figure 5.1.	Ion incident angle on a target surface with respect to the geometrical oblique magnetic field angle between the magnetic field line and the surface normal direction. Experimental data are taken from the inclined angle of nano-tips (dots). Model-estimated ion incident angle (dashed line) is calculated with corresponding plasma parameters used in the experiments. 91

- Figure 5.2.** Variation of ion velocity at the sheath edge and the wall surface vs. geometrical magnetic field angle with respect to surface normal direction. Ions can only gain energy toward surface normal direction inside the sheath region (from the sheath edge to the wall surface). 93
- Figure 5.3.** Ion velocity for $\psi = 60^\circ$ and $\Lambda_{cm} = 0.01, 0.1, 0.5, 1, 5, 10, 100$. The velocities are normalized over the Bohm's velocity, C_s . The sheath edge is where $V_x/C_s = 1$ 95
- Figure 5.4.** Variation of the ion incident angle vs. geometrical magnetic field angle with various Λ_{cm} (a) at the sheath edge and (b) at the negatively biased wall. As the collisionality increases (smaller Λ_{cm}), the ion incident angle decreases. (i.e., ions enter the surface following the surface normal direction). .97
- Figure 5.5.** (a) potential drop in presheath for various Λ_{cm} . (b) total length of the presheath (black-solid line), length of the presheath where $E \times B$ motion dominates (red-short-dashed line), and the ratio between the two lengths (blue-dashed line) versus ion-neutral collisional mean-free-path 99
- Figure 5.6.** (a) Potential drop in presheath for various magnetic field angle, ψ . (b) Total length of the presheath (black-solid line), length of the presheath where $E \times B$ motion dominates (red-short-dashed line), and the ratio between the two lengths (blue-dashed line) versus magnetic field angle. Lengths are normalized over the ion-neutral mean free path. 100

Figure 6.1.	Ion velocity distribution in front of DC biased target immersed in xenon plasma. $p = 0.18$ mTorr, $n_e \sim 3 \times 10^9$ cm⁻³, $T_e \sim 1.1$ eV, $Cs, Xe \sim 900$ m/s, $V_{bias,DC} = -100$ V, $V_p \sim 3$ V	102
Figure 6.2.	Variation of (a) ion drift velocity, (b) FWHM of IVDF in longitudinal direction, (c) FWHM of IVDF in perpendicular direction in front of DC-biased target	105
Figure 6.3.	Variation of IVDF at various positions in a presheath formed in front of a rf-biased target. The Landau damping of the electrostatic wave changes the IVDF at the phase velocity of the wave.	109
Figure 6.4.	Spatial variation of the ion velocity distribution in front of the radio-frequency biased target	109
Figure 6.5.	Spatial variation of full width at half maximum (FWHM) in presheaths formed in front of DC (black-hollow-square) and RF (blue-hollow-circle) biased targets.	110
Figure 6.6.	Space potential profiles versus distance from the radio-frequency biased target at various bias frequencies.	112

Chapter 1. Introduction

1.1. Bohm criterion for sheath formation

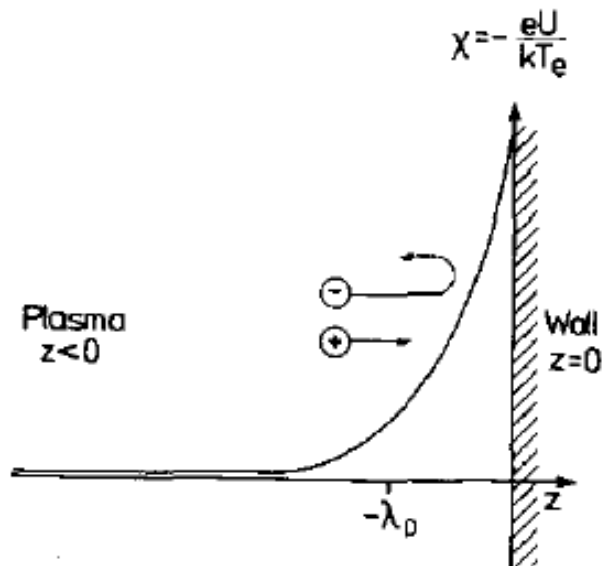


Figure 1.1. Shielding positive sheath in front of a negative wall [1].

The plasma sheath is a unique and universal structure that is formed between the plasma and the plasma-facing wall. Because the mass of an electron, m_e , is much smaller than the mass of an ion, M_i , the mobility of the electron is much higher than that of the ion. Therefore, the electrons near the plasma-facing wall usually hit the plasma-facing wall much faster than the ions and the quasi-neutrality breaks in the region between the wall and the plasma. This region where the charge-neutrality is broken is called the plasma sheath. After the quasi-neutrality is broken, an electric field is

formed in the region in the direction, from the plasma to the wall, and the field retards the loss of electrons and accelerates the ion loss until the losses of two charged species form an equilibrium. For the equilibrium state, Bohm [2] theoretically derived a condition that ions should have at the entrance of the sheath region, and the condition is called the Bohm sheath criterion for the sheath formation.

For a singly-charged, one-ion-species, collision-less, and non-magnetized plasma, the Bohm criterion can be derived as follow. For a convenience, normalized quantities are introduced as

$$y = \frac{m_i V_i^2}{2kT_e}, c = -\frac{eU}{kT_e}, n_{e,i} = \frac{N_{e,i}}{N_0}, \text{ and } x = \frac{z}{l_D}. \quad (1.1)$$

Here, T_e is the electron temperature, N_0 is the density of charged particle at the sheath entrance, U is the space potential, and $l_D = (e_0 k T_e / N_0 e^2)^{1/2}$ is the Debye length defined at the sheath entrance. Then the governing equations that describe the sheath characteristic can be written as follows.

$$\text{Ion continuity: } n_i y^{1/2} = y_0^{1/2} \quad (1.2)$$

$$\text{Energy conservation: } y = y_0 + c \quad (1.3)$$

$$\text{Boltzmann relation: } n_e = \exp(-c) \quad (1.4)$$

$$\text{Poisson } \frac{d^2 c}{dx^2} = n_i - n_e \quad (1.5)$$

With an appropriate boundary condition, $c, dc/dx \rightarrow 0$ as $x \rightarrow \infty$, the spatial derivative of the space potential can be obtained by

$$\frac{dc}{dx} = 4y_0^{1/2} \left(\frac{c}{y_0} - 1 + 2(e^{-c} - 1) \right)^{1/2} = \frac{1}{2y_0} c^2 + o(c^3). \quad (1.6)$$

Since the left-hand side of Eq. (1.6) should be positive, the first term in the right-hand side becomes positive and thus $y_0 \geq 1/2$. With dimensional variable, it can be expressed as

$$V_i \geq \frac{\sqrt{e T_e}}{m_i} V_{Bohm} \quad (1.7)$$

Eq. (1.7) is generally called as the Bohm criterion for the formation of the sheath. It means that for the formation of the sheath, the ion velocity should be larger than the Bohm velocity V_{Bohm} at the sheath entrance. Later [3], the Bohm velocity is found to be the boundary condition for the quasi-neutral plasma from the analysis of the dispersion relation of ion acoustic waves. The phase velocity of the ion acoustic wave, C_s , equals to the Bohm velocity and the notation, C_s , is more widely used in various researches.

Since the ion velocity should be larger than the Bohm velocity at the sheath edge as shown in Eq. (1.7), the need of a region between the sheath the plasma was brought up, in which the ions could get the kinetic energy that corresponded to the Bohm velocity. Because the region should lie before the sheath, the region is called the ‘pre’-sheath. Under the collision-less limit, the potential drop of the presheath region was supposed to be $0.5 T_e$, which is comparable to the kinetic energy of ion at the Bohm velocity as

$$E_{k,SE}/e = \frac{1}{2} m_i V_{Bohm}^2 / e = 0.5 T_e. \quad (1.8)$$

By assuming that the potential difference in the presheath region is $0.5 T_e$, the density at the sheath edge can also be determined from the Boltzmann relation for the electron density in the presheath region as

$$n_{SE} = n_0 \exp\left\{-\frac{eD U_{pr}}{kT_e}\right\} = n_0 \exp(-0.5) = 0.61n_e. \quad (1.9)$$

Here, The conditions for the sheath edge, Eq. (1.7) and Eq. (1.9), make up the sheath edge criterion used for many practical applications.

1.2. Universal sheath condition on charge density

The final form of the Bohm sheath criterion shown in Eq. (1.7) defines the entrance velocity of ions at the sheath edge for the formation of sheath. It is easily considered that the Bohm criterion is a velocity criterion which the ion velocity should satisfy. But it is not certain that the ions will have the velocity at any circumstance they meet near the plasma boundary, because the assumptions which is considered in the Bohm's original derivation is not practical. The sheath criterion for many practical conditions including, for example, the existence of ion-neutral collisions, magnetic fields, or the effect of ion temperatures, should be studied. The criterion for the more general plasmas is called the generalized Bohm criterion (GBC).

For the generalization of Bohm sheath criterion, the hidden meaning of the original Bohm sheath criterion should be noted. We derived the Bohm criterion from the assumption, $(dc/dx)^2 > 0$ in Eq. (1.6). Although dc/dx can be both positive and negative, because the condition $dc/dx < 0$ is not physical, the Bohm criterion for the sheath formation is re-written as

$$dc/dx > 0. \quad (1.10)$$

Eq. (1.10) means that the spatial density gradient of ion is smaller than the spatial density gradient of electron. Compare to the original form of the Bohm criterion of Eq. (1.7), Eq. (1.10) is more general form of the sheath criterion. In other words, the Bohm criterion can be expressed as a condition for the charge density that the net charge gradient at the starting point of the sheath should positive for the formation of the sheath as

$$\frac{dn_i}{dx} < \frac{dn_e}{dx}. \quad (1.11)$$

From the sheath condition for the space charge density of Eq. (1.11), we can also reach the original Bohm criterion. The spatial gradient of the ion density can be obtained from the continuity equation, and the spatial gradient of the electron density is obtained from the Boltzmann relation and the energy conservation for the ions as follows.

$$\frac{dn_i}{dx} = -\frac{n_i}{v_i} \frac{dv_i}{dx} \quad (1.12)$$

$$\frac{dn_e}{dx} = n_0 \frac{e}{kT_e} \frac{d\phi}{dx} \quad (1.13)$$

$$\frac{d\phi}{dx} = -\frac{m_i v_i}{e} \frac{dv_i}{dx} \quad (1.14)$$

By substituting Eqs. (1.12) - (1.14) into Eq. (1.11), the original form of the Bohm sheath criterion is obtained as

$$v_i^2 > \frac{eT_e}{M}. \quad (1.15)$$

Eq. (1.15) is the same to the Bohm criterion on the formation of the sheath. Therefore, it can be concluded that the position, where the sheath begins (i.e., the sheath edge), is

where the charge-neutrality breaks and the ions enter the Bohm velocity. Therefore, the charge density condition, Eq. (1.10) or Eq. (1.11), can be called the universal charge density condition for the sheath formation.

Here, a more rigorous derivation on the universal charge density condition for the sheath formation will be introduced. It starts from the Poisson's equation,

$$\frac{d^2\Phi}{dx^2} = -\frac{\rho}{\epsilon_0}. \quad (1.16)$$

By multiplying $E = -d\Phi/dx$ and integrating the Poisson's equation for distance, x , we can get following relation.

$$\int \frac{d\Phi}{dx} \frac{d^2\Phi}{dx^2} dx = -\int \frac{\rho}{\epsilon_0} \frac{d\Phi}{dx} dx \quad (1.17)$$

Applying the chain-rule on the left-hand side of Eq. (1.17) and the integration over the distance from the sheath edge to a certain position x in the sheath region one can get the relation regarding the electric field as

$$\int \frac{1}{2} \frac{d}{dx} \left(\left(\frac{d\Phi}{dx} \right)^2 \right) dx = \int \frac{1}{2} d \left(\left(\frac{d\Phi}{dx} \right)^2 \right) = \frac{1}{2} E^2 - \frac{1}{2} E_{SE}^2. \quad (1.18)$$

The integration on the right-hand side of Eq. (1.17) can be simplified by integrating over x and expanding the charge density term with respect to the potential difference.

For small potential difference near the sheath edge, one can expand the integrand as

$$\begin{aligned} -\int \frac{\rho}{\epsilon_0} \frac{d\Phi}{dx} dx &= -\frac{1}{\epsilon_0} \int \rho_{SE} + \left. \frac{d\rho}{d\Phi} \right|_{SE} (\Phi - \Phi_{SE}) + \dots d\Phi \\ &\approx -\frac{1}{2} \frac{1}{\epsilon_0} \left. \frac{d\rho}{d\Phi} \right|_{SE} (\Phi^2 - \Phi_{SE}^2) \end{aligned} \quad (1.19)$$

The net charge density at the sheath edge, r_{SE} , is nearly zero because of the quasi-

neutrality as $\rho_{SE} = \sum_i q_i n_{i,SE} - e n_{e,SE} \approx 0$. Here, the multi-ion-species condition has

been assumed. As a result of the above calculation, the integration of Eq. (1.17) yields Eq.(1.20).

$$-\frac{d\rho}{d\Phi}\Big|_{SE} (\Phi^2 - \Phi_{SE}^2) \approx \varepsilon_0 (E^2 - E_{SE}^2) \quad (1.20)$$

Because the square of the potential and electric field inside the sheath is much larger than those at sheath edge, one can notice that the density gradient with respect to the space potential should be negative for the formation of the sheath. That is

$$q_s \sum_{s=e,i} \frac{dn_s}{d\Phi}\Big|_{SE} \leq 0. \quad (1.21)$$

Eq. (1.21) is the universal charge density condition for the sheath formation which can be re-written as

$$\boxed{\sum_{s=e,i} q_s \frac{dn_s}{dx}\Big|_{SE} \geq 0}. \quad (1.22)$$

In the derivation of the Eq. (1.22) we have assumed that the spatial gradient of the space potential at the sheath edge is $dF/dx \neq 0$.

1.3. Previous studies on generalization of Bohm criterion

Riemann [3-5] greatly contributed on the generalization of the Bohm sheath criterion from 1970s. Unlike the Bohm's original form of the sheath criterion, which is limited to the single-ion-species, collision-less, magnetic-field-free, and electro-static conditions with fluid description, he tried to generalize those constraint conditions. Here, we briefly introduce his effort to generalize the Bohm sheath criterion.

The first try regarding the generalization of the Bohm sheath criterion is for the kinetic expansion of the criterion. Since the Bohm's original derivation [2] considered the ion motion in a fluidic view, the ion distribution was assumed as mono-energetic or drifting Maxwellian with an extremely small ion temperature. Therefore, a role of kinetic effects on the formation of the sheath, which might exist, could not be considered in the criterion. The consideration of the kinetic effect starts from the 1-dimensional Vlasov equation, which is so called as the collision-less Boltzmann equation for charged species, under the magnetic-field-free condition.

$$v_x \frac{\partial f_s}{\partial X} + \frac{q_s}{m_s} E \frac{\partial f_s}{\partial v_x} = 0 \quad (1.23)$$

The universal charge density condition for the sheath formation of Eq. (1.22) can be expressed as an integration form as

$$\sum_{s=e,i} q_s \int d^3v \left. \frac{\partial f_s}{\partial X} \right|_{SE} \geq 0. \quad (1.24)$$

By substituting the spatial derivation $\frac{\partial f_s}{\partial X}$ in Eq. (1.24) to a derivation in the velocity space, $\frac{\partial f_s}{\partial v_x}$ using the Vlasov equation, one can obtain the kinetic form of the generalized Bohm criterion as

$$\boxed{\sum_{s=i} \frac{q_s^2}{m_s} \int d^3v \frac{E}{v_x} \frac{\partial f_s}{\partial v_x} \leq -\frac{e^2}{m_e} \int d^3v \frac{E}{v_x} \frac{\partial f_e}{\partial v_x}}. \quad (1.25)$$

Eq. (1.25) can be more simplified by applying integration by parts on the left-hand side of the equation as

$$\sum_{s=i} \frac{q_s^2}{m_s} \int d^3v \frac{1}{v_x^2} f_s \leq -\frac{e^2}{m_e} \int d^3v \frac{1}{v_x} \frac{\partial f_e}{\partial v_x}. \quad (1.26)$$

Eq. (1.26) is the final form of the kinetic form of the generalized Bohm criterion. Here, one can find that two constraints of the original Bohm criterion have been generalized; that are the existence of multiple-ion-species and the consideration of kinetic distribution.

It should be noted that this form does not generalize all the constraints that Bohm assumed. i.e., the effect of collisions, magnetic fields and effect of the variation of ion velocity distribution are not yet considered.

Later, however, some authors [6-7] have been mentioned that Eq. (1.25) and Eq. (1.26) have some problems. One is the fact that the integrand in Eq. (1.25), $v^{-1} \frac{\partial f}{\partial v}$, is not a differentiable function at $v = 0$. Thus, the integration by parts over the whole velocity plane cannot be applied. Or, the term, $v^{-1} \frac{\partial f}{\partial v}$ in the integrand of Eq. (1.25), should be defined only for $v > 0$, which cannot be true, physically. Therefore, it has been pointed out that Eq. (1.25), rather than Eq. (1.26) should be a kinetic generalized Bohm criterion. The second is that the above forms of the criterion place an undue importance on the slow ions from the ion velocity distribution. For the drifting Maxwellian distribution of ions, as an example, there are always non-zero but very sparse particles at and near $v = 0$. Physically, their role might not have a great importance on the criterion. However, mathematically, their role

has a significant importance since the integration over velocity space becomes infinity due to the slow ions.

Riemann introduced another method to generalize the Bohm sheath criterion. From the momentum and continuity equations describing the ion motion in the presheath and by assuming Boltzmann distribution for electron density, one can obtain the governing equation for the ion density distribution in the presheath region as follows.

$$\left(e - \sum_{s=i} q_s^2 n_s (m_s V_s^2 - T_s)^{-1} \frac{T_e}{en_e} \right) \frac{\partial n_e}{\partial X} = \sum_{s=i} q_s (m_s V_s^2 - T_s)^{-1} \left(-q_s n_s (\mathbf{V} \times \mathbf{B})_x + n_s \frac{\partial T_s}{\partial X} + \frac{\partial \pi_{s,xx}}{\partial X} - R_{s,x} \right) \quad (1.27)$$

As shown in Eq. (1.27), the left-hand side of the equation has as a singularity at

$$\boxed{\sum_{s=i} \frac{n_s q_s^2}{m_s V_s^2 - T_s} = \frac{e^2 n_e}{T_e}}, \quad (1.28)$$

unless the right-hand side of Eq. (1.27) equals to zero at the condition of Eq. (1.28).

The meaning of the singularity is that the quasi-neutrality breaks at the sheath edge because $\frac{\partial n_e}{\partial X}$ should be infinite if the condition of Eq. (1.28) satisfies.

Analogous to the discussion in section 1.2, in which the breaking condition of the quasi-neutrality is argued as the criterion for the sheath formation, the condition of Eq. (1.28) is the Bohm criterion for multiple-ion-species plasmas.

For a singly-charged, single-ion-species condition, one can observe that Eq. (1.28) is simplified into

$$V_i^2 = \frac{T_e + T_i}{m_i}, \quad (1.29)$$

which is identical to the original Bohm sheath criterion except that the ion temperature was considered additionally. Because the ion drift velocity starts from a small drift velocity at the position far from the sheath entrance in the quasi-neutral plasma, the ion fluid velocity is always smaller than $\sqrt{(T_e + T_i)/m_i}$ in the quasi-neutral presheath region. This fact that the original Bohm criterion can be obtained again from Eq. (1.28) confirms that the Bohm sheath criterion can be considered as the breaking condition of the quasi-neutrality as we discussed in the section 1.2. For the formation of the sheath, the ion fluid velocity should be larger than the Bohm velocity (Eq. (1.7)), and the quasi-neutral condition maintains while the ion fluid velocity is smaller than the Bohm velocity (Eq. (1.29)).

It is quite interesting that the singularity comes from the assumption that the electrons satisfies a Boltzmann distribution as $n_e = n_{SE} \exp(ef/kT_e)$. On the contrary, the ion follows the continuity equation and the ion density varies proportional to $(-f)^{-1/2}$, which is much slower variation than the exponential variation of electron density. When the quasi-neutrality is treated as

$$e \frac{dn_e}{dx} = \sum_{s=i} q_s \frac{dn_s}{dx}, \quad (1.30)$$

there must be a position where the ion density cannot make an equilibrium with electron density and the effect is represented as a sheath criterion for the ion velocity. However, whenever we make constraint of the quasi-neutrality between electrons and ions by simply assuming the equality between ion continuity and Boltzmann distribution for electrons, we lose the property of ion dynamic effect on the sheath criterion. In other words, imperfect idealization on the dynamic properties of charged

particles make us reach a simple but not rigorous condition for the sheath formation. If we do not simplify the distributions of ions and electrons, we might reach another form of generalized Bohm sheath criterion.

1.4. Generalization of Bohm sheath criterion by ion dynamics

Here, another generalized form of the Bohm sheath criterion that fully considers ion and electron dynamic properties will be introduced [6-7]. The main idea is that the universal charge density condition for the sheath formation of Eq. (1.22) is maintained while the kinetic dynamic properties of electrons and ions are fully considered by using the Boltzmann equation,

$$\mathbf{v} \cdot \frac{\partial f_s}{\partial \mathbf{r}} + \frac{q_s}{m_s} (\mathbf{E} + \mathbf{v} \times \mathbf{B}) \cdot \frac{\partial f_s}{\partial \mathbf{v}} = C(f_s) = \sum_{s'} C(f_s, f_{s'}). \quad (1.31)$$

Here, the subscript s denotes the species of the charged particles including electrons and ions.

The process to generalize the Bohm sheath criterion is quite similar to the Riemann's plasma-side approach on the generalization of the Bohm criterion, in which the singularity condition was obtained (section 1.3). First, the zeroth and first moments of Eq. (1.31) can be obtained as

$$\frac{\partial n_s}{\partial t} + \nabla \cdot (n_s \mathbf{V}_s) = 0 \quad (1.32)$$

and

$$m_s n_s \left(\frac{\partial \mathbf{V}_s}{\partial t} + (\mathbf{V}_s \cdot \nabla) \mathbf{V}_s \right) - q_s n_s (\mathbf{E} + \mathbf{V}_s \times \mathbf{B}) + \nabla p_s + \nabla \cdot \boldsymbol{\pi}_s = \mathbf{R}_s. \quad (1.33)$$

Here, the pressure of a charged species is defined as $p_s = \int d\mathbf{v} \frac{1}{3} m_s w_s^2 f_s = n_s T_s$, the

viscosity is defined as $\boldsymbol{\pi}_s = \int d\mathbf{v} m_s \left(\mathbf{w}_s \mathbf{w}_s - \frac{1}{3} w_s^2 \mathbf{I} \right) f_s$, and the collisional friction

term is defined as $R_s = \int d\mathbf{v} m_s \mathbf{v} C(f_s)$. For the next step, the steady-state limit of

Eq. (1.32) was expanded to obtain

$$V_{s,x} \frac{\partial n_s}{\partial x} + n_s \frac{\partial V_{s,x}}{\partial x} = 0 \quad (1.34)$$

and the spatial gradient of the charged species of Eq. (1.34) was substituted into the universal charge density condition for the sheath formation of Eq. (1.22) to yield

$$\sum_{s=e,i} q_s \frac{n_s}{V_{s,x}} \frac{\partial V_{s,x}}{\partial x} \Big|_{x=SE} \leq 0. \quad (1.35)$$

Eq. (1.35) is a universal sheath condition expressed in terms of fluid velocity of charged species.

The spatial derivation of the fluid velocity in Eq. (1.35) can be obtained from the time-independent momentum equation,

$$m_s n_s V_{s,x} \frac{\partial V_{s,x}}{\partial x} - q_s n_s (E_x + (\mathbf{V}_s \times \mathbf{B})_x) + \frac{\partial p_a}{\partial x} + \frac{\partial \pi_{a,xx}}{\partial x} = R_{a,x}, \quad (1.36)$$

as

$$\frac{\partial V_{s,x}}{\partial x} = \frac{q_s n_s (E_x + (\mathbf{V}_s \times \mathbf{B})_x) - n_s \frac{\partial T_s}{\partial x} - \frac{\partial \pi_{s,xx}}{\partial x} + R_{s,x}}{\left(m_s n_s V_{s,x} - \frac{n_s T_s}{V_{s,x}} \right)}. \quad (1.37)$$

Finally, by substituting Eq. (1.37) into Eq. (1.35), the generalized Bohm sheath criterion, which fully considers the dynamic effects of charged particles regarding the effect of collisions, magnetic-fields, and temperature non-homogeneity has been obtained as

$$\sum_{s=e,i} q_s \left[\frac{q_s n_s - \left(n_s \frac{\partial T_s}{\partial x} + \frac{\partial \pi_{s,xx}}{\partial x} - q_s n_s (\mathbf{V}_s \times \mathbf{B})_x - R_{s,x} \right) / E_x}{(m_s V_{s,x}^2 - T_s)} \right]_{SE} \leq 0. \quad (1.38)$$

If the x -direction is defined as an anti-normal direction of the plasma-facing surface and the magnetic field lies in xy -plane as $\mathbf{B} = (B_x, B_y, 0) = B(\cos y, \sin y, 0)$, the Eq. (1.38) can be expressed as

$$\sum_{s=e,i} q_s \left[\frac{q_s n_s - \left(n_s \frac{\partial T_s}{\partial x} + \frac{\partial \pi_{s,xx}}{\partial x} - q_s n_s V_z B \sin \psi - R_{s,x} \right) / E_x}{(m_s V_{s,x}^2 - T_s)} \right]_{SE} \leq 0. \quad (1.39)$$

Here, the electric field is assumed to be formed along the surface normal direction as $\mathbf{E} = (E_x, 0, 0)$.

The generalized form of Eq. (1.38) and Eq. (1.39) is quite different from the above-mentioned criteria derived in section 1.1 ~ 1.3. The first thing is that this form of generalized sheath criterion includes all the kinetic and magnetic-field-induced effects that charged particles can have. The seemingly artificial assumption on the density distribution of the charged particle, which leads to the singularity, are not adopted. The second is that this consists of positive moments of the Boltzmann equation thus there is no pole at $v = 0$. Only the fluidic motions of the charged particles are considered. The last is that although this form of the criterion is expressed by using fluidic moments, kinetic effects regarding the ion velocity distribution is fully integrated in the equation. In addition, when the ion dynamic effects like the spatial temperature variation, existence of the magnetic field, or the collisional effects are not considered, the above equation is reduced to the original form of the Bohm criterion. Therefore, it can be concluded that Eq. (1.38) and Eq. (1.39) can be used to

represent the sheath edge condition in the existence of collisions, oblique magnetic fields and variation of the velocity distribution.

Lastly, it should be noted that the potential drop in the presheath of single-ion-species plasmas can be explained as

$$\left(1 + \frac{T_i}{T_e}\right) \Delta\Phi_{pr} \approx \int \left[\frac{\partial E_K}{\partial x} + V_z B_y + \frac{\partial T_i}{\partial x} + \frac{1}{n_i} \frac{\partial \pi_{i,xx}}{\partial x} - \frac{R_{i,x}}{en_i} \right] dx, \quad (1.40)$$

when all the effects of collisions, oblique magnetic fields and variation of the velocity distribution. In the derivation of the Eq. (1.40), it is assumed that the average velocity of the electron is zero and all the additional dynamic effects on the electrons is neglectable. The terms in the right-hand side are the spatial variation of the ion kinetic energy, $\frac{\partial E_K}{\partial x}$, the drift velocity of the gyrating ions, $V_z B_y$, the spatial variation of the ion temperature, $\frac{\partial T_i}{\partial x}$, the spatial variation of the ion viscosity, $\frac{1}{n_i} \frac{\partial \pi_{i,xx}}{\partial x}$, and the collisional friction, $\frac{R_{i,x}}{en_i}$.

1.5. Ion dynamics in presheath of collisional, magnetized, and RF plasmas

The generalized Bohm sheath criterion and the generalized presheath potential drop are summarized in Eq. (1.41) and Eq. (1.42).

Generalized sheath criterion:

$$\sum_{s=e,i} q_s \left[\frac{q_s n_s - \left(n_s \frac{\partial T_s}{\partial x} + \frac{\partial \pi_{s,xx}}{\partial x} - q_s n_s V_z B \sin \psi - R_{s,x} \right) / E_x}{(m_s V_{s,x}^2 - T_s)} \right] \Bigg|_{SE} \leq 0 \quad (1.41)$$

Generalized presheath potential drop:

$$\left(1 + \frac{T_i}{T_e} \right) \Delta \Phi_{pr} \approx \int \left[\frac{\partial E_K}{\partial x} + V_z B_y + \frac{\partial T_i}{\partial x} + \frac{1}{n_i} \frac{\partial \pi_{i,xx}}{\partial x} - \frac{R_{i,x}}{en_i} \right] dx \quad (1.42)$$

As shown in those equations, many terms regarding the ion dynamics in the presheath were added, which were neglected in the original form of the Bohm criterion. The terms and the meaning of the equations are summarized in table 1.1. In order to characterization of the generalized Bohm criterion, the characteristic of the ion dynamics in the presheath should be investigated.

In this thesis, the characteristics of the ion dynamics will be investigated. For the collisional friction term, the effects of ion-neutral collisions and the effect of ion-ion collisions are considered. Although the effect of ion-neutral collisions on the Bohm sheath criterion have been studied in weakly-collisional plasmas, the characteristic of the presheath potential in the condition have not yet been clearly understood. The ion-ion collision in weakly-ionized plasmas is usually very weak, therefore the two-stream-instability-enhanced collisional friction in the presheath of two-ion-species plasmas

will be analyzed. For the investigation of the effect of oblique magnetic fields, we will introduce a fluid model that describes the ion motion near a wall-surface, which forms an oblique angle with the external magnetic fields. The characteristic of the ion motion and the presheath potential distribution under the oblique magnetic fields near the wall-surface will be analyzed with the consideration of ion-neutral collision. For the investigation of the effect of spatial variation of the ion temperature, we will firstly observe the intrinsic variation of the spatial variation of the ion velocity distribution in a presheath in front of the DC biased target. Then by applying an oscillating bias voltage to the electrode with various frequencies in radio-frequency range, we will observe the effect of radio-frequency wave on the heating of the ions in the region of presheath. By observing those effects on the ion dynamics in the presheath region, we can characterize the generalized Bohm sheath criterion of Eq. (1.41).

Table 1.1. Meaning of ion-dynamic-related modification terms on Bohm criterion

Terms	Related Physical Properties
Frictional force, $R_{s,x}$	Collisional friction
Lorentz force, $q_s n_s (\mathbf{V}_s \times \mathbf{B})_x$	Presence of external B-field
Spatial derivative of temperature, $n_s \partial T_s / \partial x$	Variation of ion velocity distribution
Spatial derivative of viscosity, $\partial \pi_{s,xx} / \partial x$	

Chapter 2. Previous studies on ion dynamics in collisional, magnetized and RF sheath

2.1. Effect of two-stream-instability-enhanced (TSD) ion-ion collision on Bohm sheath criterion

2.1.1. Effect of two-stream-instability on ion motion in presheath

The speed of ions leaving the plasma boundary, or the sheath edge is a key factor in understanding plasma-wall interaction and even the plasma itself, because it provides an ion flux on the surface that touches the plasma. For single-ion-species plasmas, Bohm [2] predicted that the ions become supersonic at the sheath edge where their velocity is given by $c_i = \sqrt{k_B T_e / M_i}$, which is now referred to as the Bohm velocity. For plasmas containing multiple ion species, Riemann [3-5] generalized the Bohm criterion as $\sum_i (n_i c_i^2 / n_e V_i^2) \leq 1$. However, the criterion does not determine the specific value of each ion's drift velocity at the sheath edge, even for the simplest two-ion-species condition. Regarding this issue, many researchers [8,9] suggested that all ion species exit the plasma boundary with their *individual Bohm velocities*, in that they fall through the same potential difference before they enter the sheath. However, some experiments [10-12] have shown that ions do not exit plasma with their individual Bohm velocities, but with a velocity closer to a system common sound velocity, $C_s = \{\sum_{i=1,2} [c_i^2 (n_i / n_e)]\}^{1/2}$, in two-ion-species plasmas.

Baalrud *et al.* [13-15] provided a theoretical framework for determining the ion speed at the sheath edge in collision-less two-ion-species plasmas. They suggested that the mutual interaction between the two-ion species brings about the two-stream-instability inside the presheath. The instability then causes a brisk momentum transfer between the different ion species, forcing the drift speed of each ion species at the sheath edge to be closer to the system common sound velocity, which is referred to as *the modified Bohm velocity* and given by,

$$V_1 \approx C_s + \left(n_2 c_2^2 / n_e C_s^2 \right) \Delta V_c \quad (2.1)$$

and

$$V_2 \approx C_s - \left(n_1 c_1^2 / n_e C_s^2 \right) \Delta V_c. \quad (2.2)$$

Here, ΔV_c denotes the critical relative velocity at which the instability onset occurs (see reference [14] for more information). A schematic diagram of the ion fluid velocity profiles through the presheath region is shown in figure 2.2. It is worth noting that this instability occurs when the densities of all ion species are similar as shown in figure 2.3. For other conditions, such as $n_1 \gg n_2$ or $n_1 \ll n_2$, it has been observed that the instability does not occur, and each ion species has its own Bohm velocity [16,17].

In weakly ionized plasmas, however, there always exist some amount of ion-neutral collisions, and the collision can disturb the instability to occur by interrupting the momentum transfer between the different ion species even when the relative ion density is close to unity. It agrees with Baalrud's prediction [18] that there is a pressure threshold above which the ion-neutral collisions disrupt the instability. If the

occurrence of the instability is disturbed by the ion-neutral collisions, it is expected that the fluid velocities of the two-ion-species would be the conventional Bohm velocity at the sheath edge. Later in this thesis, we will show an experimental investigation the ion-neutral collisional effect on the occurrence of the instability and thus on the ion drift velocities at the sheath edge of two-ion-species Ar/Xe mixture plasmas.

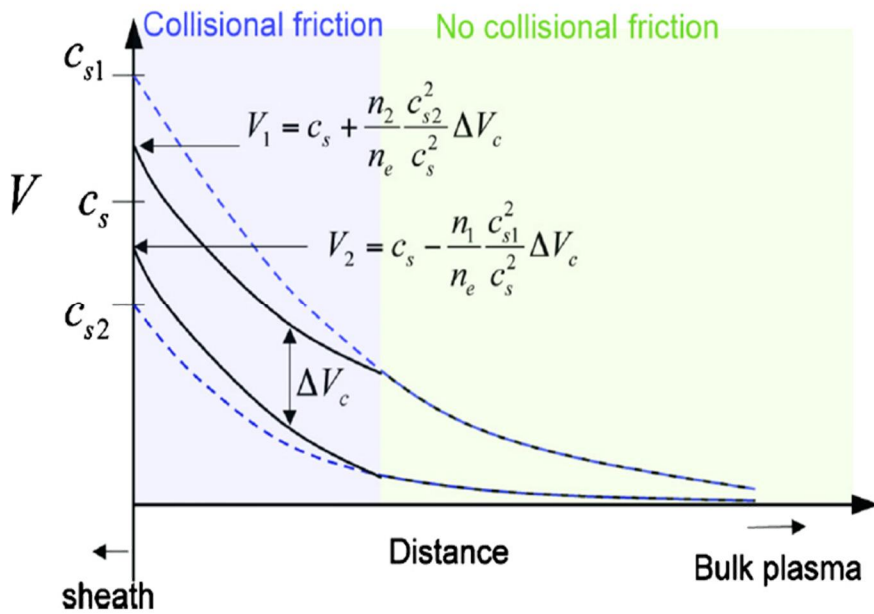


Figure 2.1. Schematic diagram of ion fluid velocity profiles through the presheath. When the relative velocity between two-ion-species becomes larger than a critical relative velocity, ΔV_c , the instability-enhanced friction modifies the ion motion near the sheath edge. Therefore, the ions have a modified Bohm velocity at the sheath edge [14].

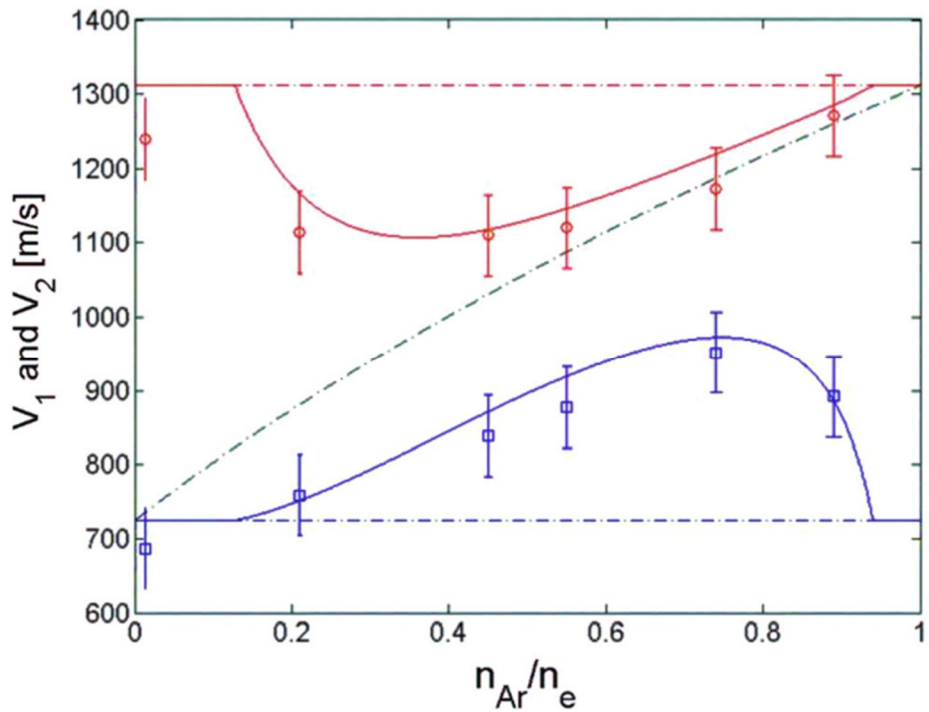


Figure 2.2. Modified ion velocity at the sheath edge of Ar/Xe mixture plasmas. As the argon and xenon ion densities become comparable, the two-stream-instability-enhanced-collisional-friction significantly modifies the sheath entrance velocity of each ion-species.

2.1.2. Generalized occurrence condition of two-stream-instability under ion-neutral collision

The pressure threshold of two-stream-instability can be estimated by solving a plasma dispersion relation which is modified to consider the ion-neutral collisional effect [19]. For the Maxwellian distributions of electrons and two ion species, the dispersion relation of wave fluctuation can be written as follows,

$$D(k, \omega) = 1 - \frac{1}{k^2 \lambda_D^2} - \sum_s \frac{\omega_{ps}^2}{k^2 V_{Ts}^2} \frac{-2(1 + \xi_s Z(\xi_s))}{1 + i \frac{v_{s-n}}{k V_{Ts}} Z(\xi_s)}. \quad (2.3)$$

In Eq. (2.3), s denotes ion species, $\xi_s = (\omega - \mathbf{k} \cdot \mathbf{V}_s + i v_{s-n}) / k V_{Ts}$, $V_{Ts} = \sqrt{2k_B T_s / M_s}$, ω_{ps}^2 is ion plasma frequency, and $Z(\xi)$ is the plasma dispersion function. The frequency, ω , is a complex variable as, $\omega = \omega_R - i\gamma$, and the wavenumber vector \mathbf{k} is real. For simplicity, the ion-neutral collision frequency, $\nu_{s-n} = n_g \langle \sigma_{s-n} V_s \rangle$, is calculated as $\nu_{s-n} \approx n_g \sigma_{s-n} C_s$. The neutral gas density is given as $n_g = p / k_B T_g$, and the collision cross section for both Ar^+ and Xe^+ is approximated as $\sigma \sim 1 \times 10^{-20} \text{ m}^2$, considering the elastic [20] and resonant/asymmetric charge exchange collisions [21] between the two ion species and the two neutral species. The growth rate of instability, $\gamma(\mathbf{k})$, can be obtained by solving $D(k, \omega) = 0$.

By accounting ion-neutral collisions, the complex frequency, ω , is modified as $\omega + i v_{s-n}$. Therefore, the growth rate of instability becomes, $\gamma - \nu_{s-n}$, and the instability occurs when $\gamma_{\max}(\mathbf{k}) > \nu_{s-n}$. From this inequality, a pressure threshold for the onset of instability is given as

$$p \lesssim \frac{\gamma k_B T_g}{\sigma C_s} = \frac{\gamma_{\max}(\mathbf{k}, p)}{3.2 \times 10^{19} \sigma C_s}. \quad (2.4)$$

Here, T_g is assumed as room temperature. It is worth noting that Eq. (2.4) should be solved iteratively using a numerical method regarding the pressure, because γ is also a function of pressure. In figure 2.4. the pressure criterion for the onset of the two-stream-instability is depicted as a solid-red line. The region above the line is a stable region where the instability does not occur and the region below the line is the unstable region where the instability occurs. For the same electron temperature, the instability cannot occur as the neutral pressure becomes higher. For the same pressure, the instability cannot occur at low electron temperatures because the critical relative velocity cannot be achieved in a weakly-collisional presheath. The relative ion velocity is proportional to the potential drop in the presheath, however, the presheath potential drop is proportional to the electron temperature, thus enough relative ion velocity cannot be achieved in low- T_e plasmas.

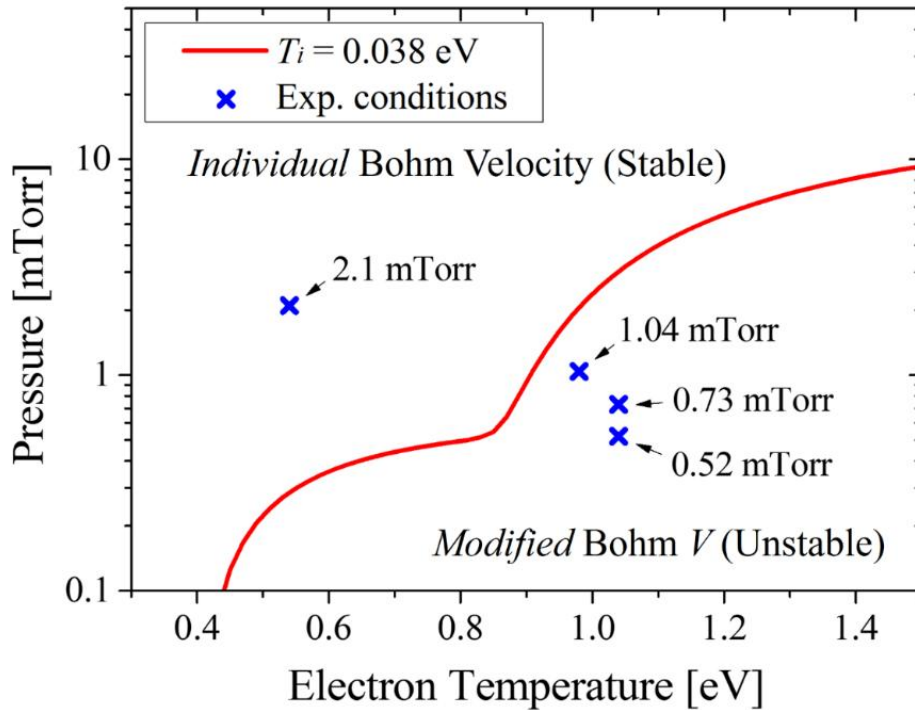


Figure 2.3. Pressure threshold of the instability with respect to the electron temperature calculated from Eq. (2.4), considering ion-neutral collisions (red-solid line). The region above the line is a stable region where the instability does not occur and the region below the line is the unstable region where the instability occurs. Experimental conditions, which are taken in the investigation (chapter 4) are marked with crosses.

2.2. Effect of oblique magnetic field on ion motion in sheath and presheath

The ion incident angle on a plasma-facing surface is a key parameter to understand the plasma-surface interaction phenomena. The tilt angle of etched patterns on a silicon wafer [22], the erosion rate of wall materials of a thermo-nuclear fusion reactor [23], and particle reflection on a plasma-facing surface [24] are all relevant to the ion incident angle on the plasma-facing surface at the time of impact. For nuclear fusion devices, however, some researchers have simply assumed that the ion incident angle on a plasma-facing surface would be comparable to the geometrical angle between the magnetic field line and the surface because magnetic fields in the devices are strong enough to confine ions to their field lines. However, due to strong electric fields formed in the plasma-wall boundary region, the ion incident angle can largely deviate from the magnetic field line.

To understand how much the angle deviates from the magnetic field line, physical characteristics of the plasma boundary region and ion motion in the region have been investigated. Various researches have been carried out for a few decades, considering plasma density, electron and ion temperature, magnetic field angle, ion-neutral collisionality, and so on [25-30]. Chodura [25-27] has proposed a 1-D collision-less model in which the transition layer between a plasma and a wall consists of a triple structure comprising quasi-neutral plasma presheath, magnetic presheath (the Chodura layer), and space-charge (Debye) sheath. He has performed a particle-in-cell simulation considering electrons and ions. He numerically found the transition condition from the plasma presheath to the magnetic presheath, also known as ion drift velocity, should be

supersonic along the magnetic field line at the entrance of the magnetic presheath. The thickness of the magnetic presheath is postulated as $\lambda_{mp} = \sqrt{6}r_{cs} \sin \psi$, where $r_{cs} = C_s / \omega_{ci}$ with $C_s = \sqrt{k_B(T_i + T_e) / M_i}$ and $\omega_{ci} = eB / M_i$. However, the collision-less condition is unachievable in practical plasmas. Riemann [28,29] has included effects of ion-neutral collisions and performed a three-dimensional analysis in which the $E \times B$ drift motion of ions is considered. With a finite collisionality, his model predicted a double structure of the plasma boundary region consisting of presheath and space-charge sheath. Unlike Chodura's model, no special entrance condition of the presheath was needed. Ahedo [30] has suggested the first comprehensive model which includes both Chodura's model and Riemann's model on the plasma-boundary region. In the collision-less limit, his model recovers the Chodura's model of a triple structure, and naturally covers the entrance condition of the magnetic presheath as a singular velocity characteristic at the position between the plasma presheath and the magnetic presheath. With a finite ion-neutral collisionality, his model recovers Riemann's model of double structure comprising presheath and space-charge sheath.

However, these plasma sheath models considering oblique magnetic fields are poorly supported by experimental verifications. Contrary to various theoretical approaches, experimental investigations on plasma-wall transition with an oblique magnetic field, especially on ion incident angle at a surface, have not been actively carried out. This might be because density of magnetized plasma is usually too high to form a plasma sheath structure of measurable size, making observation of ion motion directly inside the plasma-wall transition region difficult.

Until now, a few experimental investigations have been reported [31-33]. Kim *et al.* [31] have measured the spatial structure of electric potential in front of a negatively

biased target in weakly-magnetized, weakly-collisional plasmas in the presence of oblique magnetic fields. They observed that the plasma-wall boundary region consisted of three distinct regions: a weakly collisional-magnetized presheath, a collisional presheath, and a space-charge sheath having λ_m , λ_c , and λ_d as characteristic length scale, respectively. Here, λ_m is the ion gyro-radius, λ_c is the ion-neutral collisional mean-free-path, and λ_d is the Debye length. The first direct measurement of ion motion was carried out by Siddiqui *et al.* [32-33]. They measured 3-dimensional ion velocity distribution by using a laser-induced-fluorescence technique in front of an obliquely installed target in a helicon plasma source and demonstrated that the $E \times B$ motion could affect the ion incidental motion in the presheath, and the drift made ion trajectory 3-dimensional. They observed that the $E \times B$ motion occurred within a few ion Larmor radii of a target surface. Thus, the characteristic length of the region where the $E \times B$ motion occurred was characterized to be an ion Larmor radii. However, their fluid model calculation showed un-neglectable difference with the experimental data and because their measurements were only performed inside the presheath, the role of 3-dimensional motion on the sheath criterion or the effect of sheath electric field on ion incident characteristic at the surface could not be identified. Until now, there exists no robust description which is fully evaluated by experimental data regarding the ion motion in the whole sheath and presheath region under the existence of magnetic fields.

In the next subsections, Ahedo's [30] fluid description of the magnetic sheath will be introduced. So far, his model is the only one that includes all the magnetic and collisional characteristics regarding the magnetic sheath phenomenon. The model includes effects of $E \times B$ motion in the plasma boundary region and ion-neutral collisional effect on the motion of ions.

2.2.1. Fluidic description of ion motion in magnetic sheath and presheath

Figure 2.5 (a) shows a schematic configuration of the magnetic field and the plasma-facing wall. In a Cartesian coordinate O_{xyz} , the surface is placed at $x = x_W$. A perfectly absorbing wall is assumed to be negatively biased with respect to the electric potential of the bulk plasma as $U = U_W < 0$. The external magnetic field near the surface is assumed to be uniform. The field line forms an angle, ψ , with the surface normal direction. Thus, the magnetic field can be expressed as $\mathbf{B} = B(\cos\psi, \sin\psi, 0)$.

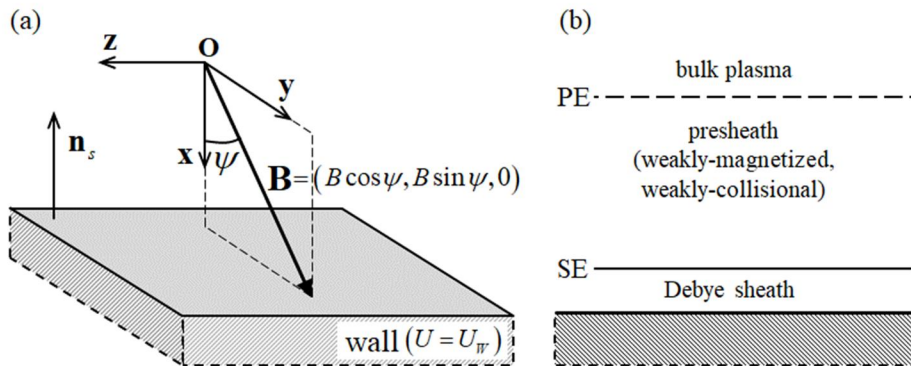


Figure 2.4. (a) The reference frame, O_{xyz} used in the model and the configuration of the magnetic field. The incident angle of the magnetic field is defined as the angle between the magnetic field line and the surface normal. (b) A schematic configuration of the plasma structure near a wall surface. The origin, O, of the reference frame in (a) corresponds to the position, PE (plasma edge), in (b).

The motion of ions and the spatial distribution of the electric potential near the surface are assumed to be governed by the following four equations: the Poisson equation, the Boltzmann relation for electrons, the continuity equation for ions, and the momentum equation along the x-direction:

$$\frac{d^2U}{dx^2} = \frac{e}{\varepsilon_0}(n_e - n_i) \quad (2.5)$$

$$k_B T_e \ln n_e - eU = \text{const.} \quad (2.6)$$

$$n_i V_x = \text{const.} \quad (2.7)$$

$$m_i V_x \frac{d\mathbf{V}}{dx} = e\mathbf{V} \times \mathbf{B} - \left(e \frac{dU}{dx} + \frac{k_B T_i}{n_i} \frac{dn_i}{dx} \right) \hat{\mathbf{x}} - \nu_c m_i \mathbf{V} \quad (2.8)$$

where n , m , and T are density, mass, and temperature, respectively, and $\mathbf{V} = (V_x, V_y, V_z)$ is the drift velocity of ions. Here, we assume that the charge number of ions is $Z=1$ and the collision frequency between the ions and the background neutral species, ν_c , is simply constant.

To solve equations without considering detailed plasma parameters, the following dimensionless parameters can be introduced as

$$\phi = -\frac{eU}{k_B T_e}, \quad N_i = \frac{n_i}{n_0}, \quad N_e = \frac{n_e}{n_0}, \quad \mathbf{v} = \frac{\mathbf{V}}{\sqrt{k_B T_i / m_i}}, \quad \text{and} \quad t = \frac{T_e}{T_i} \quad (2.9)$$

which normalizes the electric potential energy of ions (eU) with the thermal energy of electron ($k_B T_e$), densities of ions and electrons with charged particle density of the bulk plasma (n_0), the ion drift velocity with ion thermal velocity ($V_{th,i} = \sqrt{k_B T_i / m_i}$), and electron temperature with ion temperature, respectively. With these parameters, Eqs. (2.5) - (2.8) can be simplified as

$$\frac{d^2\phi}{dx^2} = \frac{(N_i - N_e)}{\lambda_d^2}, \quad (2.10)$$

$$\ln N_e + \phi = \text{const.}, \quad (2.11)$$

$$N_i = \frac{1}{v_x}, \quad (2.12)$$

$$x: \left(v_x - \frac{1}{v_x} \right) \frac{dv_x}{dx} = -\frac{v_z \sin \psi}{\lambda_m} + t \frac{d\phi}{dx} - \frac{v_x}{\lambda_c}, \quad (2.13)$$

$$y: v_x \frac{dv_y}{dx} = \frac{v_z \cos \psi}{\lambda_m} - \frac{v_y}{\lambda_c}, \quad (2.14)$$

$$\text{and } z: v_x \frac{dv_z}{dx} = \frac{v_x \sin \psi}{\lambda_m} - \frac{v_y \cos \psi}{\lambda_m} - \frac{v_z}{\lambda_c}. \quad (2.15)$$

Here, three characteristic lengths are introduced, including collision mean free path of ions, $\lambda_c = (k_B T_i / m_i)^{1/2} / v_c$, ion magnetic gyro-radius, $\lambda_m = (k_B T_i m_i)^{1/2} / eB$, and Debye length, $\lambda_d = (\epsilon_0 k_B T_e / e^2 n_0)^{1/2}$. By solving Eqs. (2.10) - (2.15), one can obtain spatial distribution of the ion drift velocity, densities of electrons and ions, and electric potential.

Further modification of Eqs. (2.13) - (2.15) is achieved by normalizing the spatial variable, x , with one of the above three characteristic lengths with respect to physical characteristics of a specific region. For Debye sheath, for example, the Debye length is appropriate as the characteristic length scale since the electric field is high inside the region enough to repel electrons flowing from the plasma which is also called Debye shielding. For the presheath, however, the other two characteristic lengths, λ_c and λ_m , can be candidates that represent the region. For a weakly magnetized presheath where the collision mean-free-path, λ_c , is comparable or smaller than the

gyro-radius, λ_m , λ_c is appropriate for the characteristic length scale of the region. When the collision is very sparse or the magnetic field is high enough, λ_m is smaller than λ_c and λ_m would be the characteristic length scale of the region. Depending on the value of $\Lambda_{cm} = \lambda_c / \lambda_m$, the presheath can have distinctive characteristics. An un-magnetized/collisional presheath ($\Lambda_{cm} \rightarrow 0$) and a magnetized/collision-less presheath ($\Lambda_{cm} \rightarrow \infty$) are two extreme cases.

2.2.2. Magnetized and weakly-collisional presheath

We considered magnetized but weakly-collisional presheath where Λ_{cm} was finite because the above two extreme cases would not be practical in many plasma conditions. Here, we call the presheath as magnetized and weakly-collisional presheath. Inside the presheath, it is commonly assumed that the quasi-neutrality is universally satisfied, i.e., $N_i \approx N_e$. With Eqs. (2.11) - (2.12) and $\eta = x/\lambda_c$, Eqs. (2.13) - (2.15) can be further simplified as

$$\left(v_x - \frac{c_s^2}{v_x} \right) \frac{dv_x}{d\eta} = -\Lambda_{cm} v_z \sin\psi - v_x, \quad (2.16)$$

$$v_x \frac{dv_y}{d\eta} = \Lambda_{cm} v_z \cos\psi - v_y, \quad (2.17)$$

$$\text{and } v_x \frac{dv_z}{d\eta} = \Lambda_{cm} (v_x \sin\psi - v_y \cos\psi) - v_z. \quad (2.18)$$

In Eq. (2.16), one can easily notice that it becomes singular at $v_x = c_s$ where the Debye sheath begins. It means that, under the magnetized and weakly-collisional

condition, the plasma boundary region consists of two distinct regions: presheath and the Debye sheath.

2.2.3. Debye Sheath

The model equations that govern the Debye sheath region can be obtained by using a normalized variable $\xi = x/\lambda_d$. Thus, $dx = \lambda_d d\xi$. The Debye length, λ_d , can be commonly considered much smaller than λ_c and λ_m ($\lambda_d/\lambda_{c,m} \rightarrow 0$) in a low-pressure, magnetized plasma condition. By substituting $\xi = x/\lambda_d$ for x and taking the limit $\lambda_d/\lambda_{c,m} \rightarrow 0$, Eq. (2.10) and Eqs. (2.13) - (2.15) become

$$\frac{d^2\phi}{d\xi^2} = (N_i - N_e) \quad (2.19)$$

$$\left(v_x - \frac{1}{v_x} \right) \frac{dv_x}{d\xi} = t \frac{d\phi}{d\xi}, \quad \frac{dv_y}{d\xi} = 0, \quad \text{and} \quad \frac{dv_z}{d\xi} = 0. \quad (2.20)$$

The second and the third equations in Eq. (2.20) show that ions are not accelerated along the y - or z - direction. It means that ions are accelerated only along the x - direction inside the Debye sheath region. Integrating the first equation of Eq. (2.20) over ξ gives the relation between v_x and ϕ as

$$\phi = \phi_{SE} + \frac{(v_x^2 - c_s^2)}{2t} - \frac{1}{t} \ln \left(\frac{v_x}{c_x} \right) \quad (2.21)$$

The spatial variation of ϕ and v_x can be obtained by solving Eqs. (2.19) - (2.20) with Eqs. (2.11) - (2.12) and appropriate initial conditions at the edge of the Debye sheath ($v_x = c_s$, $\phi = \phi_{SE}$). It can be written as

$$\frac{t}{2} \left(\frac{d\phi}{d\xi} \right)^2 = v_x + \frac{1}{v_x} + \frac{t}{c_s} \exp(\phi_{SE} - \phi) - 2c_s. \quad (2.22)$$

2.3. Landau damping of electrostatic wave travelling against ion flow

Radio-frequency power supplies are widely used to generate plasma or to accelerate ions toward an electrode in various industrial plasma sources. When a radio-frequency-biased planar electrode are immersed in the plasma, the voltage oscillation at the electrode surface can launches electrostatic wave toward the plasma by making the ions or electrons move back and forth following the potential oscillation. In many previous studies [34-36] various researchers have focused on the ion motional characteristics, especially regarding how the ion energy distribution at the target surface forms with respect to the target bias frequencies. For very a low frequency, $\omega_{rf} = \omega_{pi}$, the ion immediately responds to the potential oscillation, thus the time-averaged ion energy distribution becomes a double-peaked distribution, of which the energy difference between the two peaks correspond to the $\sqrt{V_{rf}^0}$ on the target surface. For a very high frequency, $\omega_{rf} \gg \omega_{pi}$, the ion cannot respond to the potential oscillation and only the time-averaged potential effectively acts on the ion motion. Thus, the incident ion energy distribution on the electrode becomes a single-peaked distribution at the time-averaged or the self-bias potential of the target surface.

It is interesting that the frequency range of radio-frequency wave, 0.1 ~ 100 MHz, forms a similar range of the ion plasma frequency, $f_{pi} = \omega_{pi}/2\pi = \sqrt{ne^2/m_i e_0}/2\pi$,

of typical argon plasmas as shown in figure 2.6. Thus, we have postulated that the wave-ion interaction, like the ion-heating phenomenon, can be occurred in the plasma. Therefore, we tried to observe the interaction of ion and radio-frequency electrostatic waves.

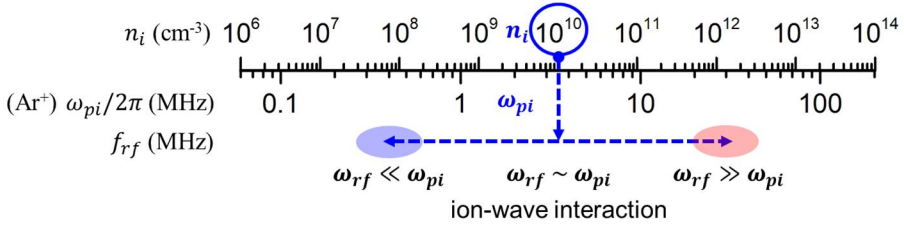


Figure 2.5. Comparison of the ion density of argon plasma with the ion plasma frequency.

Before the experimental observation, here, we introduce a theoretical background on the ion-wave interactions. For an electrostatic wave travelling the plasma medium, the wave propagation characteristics can be obtained from the plasma dispersion relation,

$$1 - \frac{1}{k^2 \epsilon_0} \left(\frac{q_i^2}{m_i} \int \frac{k \partial f_{i0} / \partial v}{kv - \omega} dv + \frac{q_e^2}{m_e} \int \frac{k \partial f_{e0} / \partial v}{kv - \omega} dv \right) = 0. \quad (2.23)$$

By solving Eq. (2.23) one can find the relation between the frequency and the wavenumber, k . By assuming that the ion velocity distribution forms a 1-dimensional drifting Maxwellian in the presheath region with an average velocity,

$$V = \int v f(v) dv$$

$$f_{a0} = n_{a0} \frac{1}{\sqrt{\pi} v_{Ta}} \exp \left(-\frac{(v - V)^2}{v_{Ta}^2} \right) \quad (2.24)$$

and

$$\frac{\partial f_{a0}}{\partial v} = n_{a0} \frac{1}{\sqrt{\pi} v_{Ta}^3} (-2(v-V)) \exp\left(-\frac{(v-V)^2}{v_{Ta}^2}\right), \quad (2.25)$$

Eq. (2.23) can be reduced to a more simplified form. Here, the thermal velocity of species a is defined as $v_{Ta} = \sqrt{2k_B T_a / m_a}$.

First, by substituting Eq. (2.25) into the ion contribution term in Eq. (2.23), one can obtain,

$$\begin{aligned} & -\frac{1}{k^2 e_0} \frac{q_i^2}{m_i} \hat{\Omega} \frac{\omega_{pi0}^2 / v}{v - w/k} dv \\ & \quad (v-V) \exp\left(-\frac{(v-V)^2}{v_{Ti}^2}\right) \\ & = \frac{1}{k^2 l_i^2} \frac{1}{v_{Ti}} \frac{1}{\sqrt{\rho}} \hat{\Omega} \frac{(v-V) \exp\left(-\frac{(v-V)^2}{v_{Ti}^2}\right)}{v - w/k} dv \end{aligned} \quad (2.26)$$

Here, l_i is defined as $l_i = \sqrt{e k_B T_i / n_{i0} q_i^2}$. With, $w \equiv v - V$, Eq. (2.26) can

be written as

$$\frac{1}{k^2 \lambda_i^2} \frac{1}{v_{Ti}} \frac{1}{\sqrt{\pi}} \int \frac{\left(w - (\omega/k - V) + (\omega/k - V)\right) \exp\left(-\frac{w^2}{v_{Ti}^2}\right)}{w - (\omega/k - V)} dw. \quad (2.27)$$

Utilizing $\int \exp(-ax^2) dx = \sqrt{\pi/a}$ into Eq. (2.27) yields

$$\frac{1}{k^2 l_i^2} \frac{1}{v_{Ti}} \frac{1}{\sqrt{p}} \sqrt{p} v_{Ti} + (w/k - V) \int_0^\infty \frac{\exp\left(-\frac{w^2}{v_{Ti}^2} x\right)}{\frac{w}{v_{Ti}} - \frac{(w/k - V)}{v_{Ti}}} \frac{1}{v_{Ti}} dw \quad (2.28)$$

Introducing normalized variables, $a = (w/k - V)/v_{Ti}$ and $x = w/v_{Ti}$, and the plasma dispersion function,

$$Z_C(a) = \frac{1}{\sqrt{p}} \int_0^\infty dx \frac{e^{-x^2}}{x - a} \quad (2.29)$$

The ion contribution on the plasma dispersion relation, Eq. (2.23) is finally reduced as

$$- \frac{1}{k^2 e_0} \frac{q_i^2}{m_i} \int_0^\infty \frac{k v_{i0} / v}{k v - w} dv = \frac{1}{k^2 l_i^2} \int_0^\infty a_i Z_C(a_i) da_i \quad (2.30)$$

Likewise, the electron contribution can be also reduced and the Eq. (2.23) finally re-written as

$$1 + \frac{1}{k^2 l_i^2} \int_0^\infty a_i Z_C(a_i) da_i + \frac{1}{k^2 l_e^2} \int_0^\infty a_e Z_C(a_e) da_e = 0. \quad (2.31)$$

Chapter 3. Experimental Setup

3.1. Plasma sources

In this section, two plasma sources that were utilized to investigate the ion dynamic effect on sheath criterion will be introduced. Those are a multi-dipole plasma source (section 3.1.1) and an electron-cyclotron-resonance plasma source (section 3.1.2).

3.1.1. Multi-dipole plasma source

Experiment was carried out in the 40-cm-diameter by 35-cm-length filament discharged multi-dipole plasma source. A simplified schematic diagram of the chamber is shown in figure 3.1. By a turbo molecular pump connected to a bottom port, the base pressure was kept 2×10^{-6} Torr. Three lines of ϕ 0.43-mm, 8-cm-long thoriated tungsten filaments were installed on the one side of the middle plane of the chamber and heated to emit energetic electrons to generate plasma. The electron is called the primary electron. The emission current of the primary electron was varied ranging from 0.1 to 0.8 A. The bias voltage of the filament set to - 60 V with respect to the electrically-grounded wall so that the primary electrons have mono-energy of ~ 60 eV. Argon, helium, or xenon gas were injected into the chamber controlled by mass flow controllers. Plasma is generated by the impact ionization process of the primary electrons with neutral gas atoms. The electron density and temperature of the generated plasma were in the range of $1 \times 10^8 \sim 1 \times 10^{10} \text{ cm}^{-3}$ and $0.5 \sim 2$ eV, which were measured by using the Langmuir probe measurement.

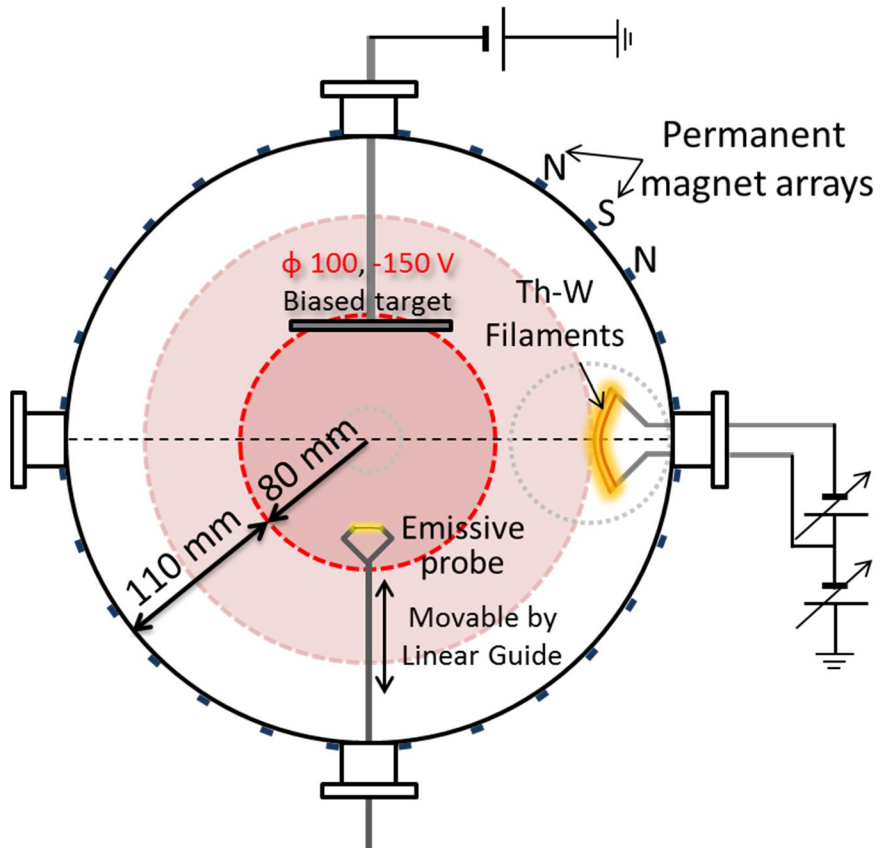


Figure 3.1. A multi-dipole plasma source. Energetic electrons emitted from hot filament wires are confined by the magnetic cusp fields around the chamber and forms a homogeneous density region. A RF or DC biased target is located at one edge of the homogeneous region to form a sheath configuration.

The cylinder chamber made of stainless-steel were covered by arrays of permanent neodymium magnets to confine the primary electrons and plasma itself [37-40]. The magnets produced a maximum magnetic cusp field of 0.1 T inside the chamber wall. Since the ion loss width of a line cusp is proportional to the hybrid Larmor radius ($W_c \sim 4\sqrt{r_e r_i}$), the loss area for the charged particle is much smaller than the actual area of the chamber, the plasma density can be achieved even for weak emission current. Although the cusp field effectively confines charged species, too much use of cusp magnet yields larger total leak area and larger plasma volume since the penetration length of the magnetic field into the plasma volume becomes shorter when the distance between permanent magnets becomes shorter. In this study, we experimentally confirmed that the use of 24 arrays of permanent magnets around the chamber yielded maximum electron density at the center of the chamber. Total length of the cusp was around 900 cm. Because the cusp magnetic field decays exponentially inside the chamber and becomes less than 1 gauss at a position 4-cm apart from the chamber inner wall, the plasma volume was limited inside the field-penetration region of the chamber. Figure 3.2 shows a typical radial distribution of the plasma electron and ion. As shown in the figure, there exists a homogeneous or uniform-density region at $r < 8$ cm. A negatively biased target was installed at one end of the uniform region. For an investigation of the effect of radio-frequency electrostatic waves on the kinetic characteristics of ions, a lab-made RF matching network was connected to the target.

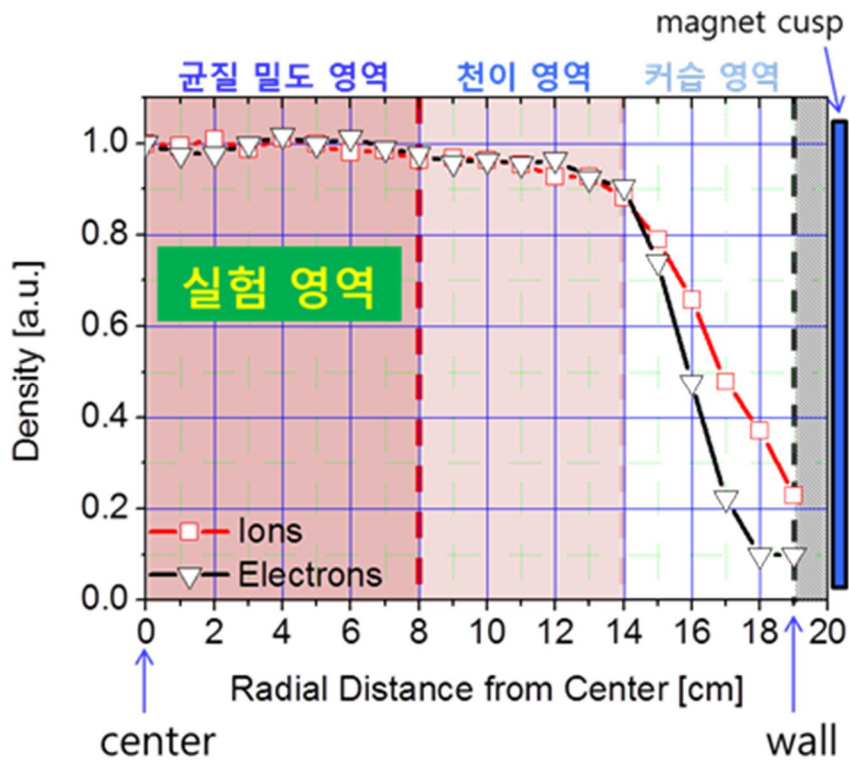


Figure 3.2. Radial density profile of electron and ions in the multi-dipole chamber.

The experiment region was assigned to the uniform-density region of $r < 8$ cm.

Table 3.1. Summary on the characteristics of multi-dipole plasma source

System	Characteristics	Chamber	Stain-less steel
		Volume	38 L (I.D.=380 mm, H=330 mm)
		Operation Pressure	0.15 ~ 2 mTorr (base: 0.001 mTorr)
		Filament	2 % Thoriated Tungsten
Plasma	Property	Discharge Mechanism	Mono-high energy e-impact
		Discharge Gas	Argon / Xenon / Helium
		Primary Electron Energy	~ 60 eV
		Confinement	Permanent Magnet Cusp (1 kG)
		Electron Density	$10^8 \sim 10^{10} \text{ cm}^{-3}$
		Electron Temperature	0.5 ~ 2 eV

3.1.2. Electron-cyclotron-resonance plasma source

To investigate the effect of oblique magnetic field on the 3-dimensional ion motion while the ions traversing a presheath and sheath, an electron-cyclotron-resonance (ECR) plasma source was utilized. A schematic diagram of the plasma source is shown in figure 3.3. A pair of current coils, located at the top side of the plasma chamber, forms a magnetic field inside the chamber. A microwave whose frequency is 2.45 GHz is injected into the chamber through the upper quartz glass and resonate electrons where the magnetic field is 875 gauss. The zone where the resonance occurs is called the ECR zone or the resonant surface. The plasma chamber consists of two parts. One is the upper source chamber in which the ECR zone exists and the other is the diffusion chamber located below the source chamber. Ions and electrons generated inside the source region diffuses toward the diffusion region along the magnetic field line. The magnetic field line slightly diverges into the diffusion chamber, but the central magnetic field at $r < 2$ cm, near the interface between the source chamber and the diffusion chamber, the angular divergence of the magnetic field line is less than 2 degree (see figure 3.4). The radial density profile shown in figure 3.3 shows that the density inhomogeneity of the region, $r < 2$ cm, is less than 10 %. A graphite target, which formed a sheath structure in the uniform plasma region, was installed right below the source chamber. Details of the target and the ion incident angle measurement method with using the target will be introduced in the section 3.4. The magnetic field at the position was about 600 gauss.

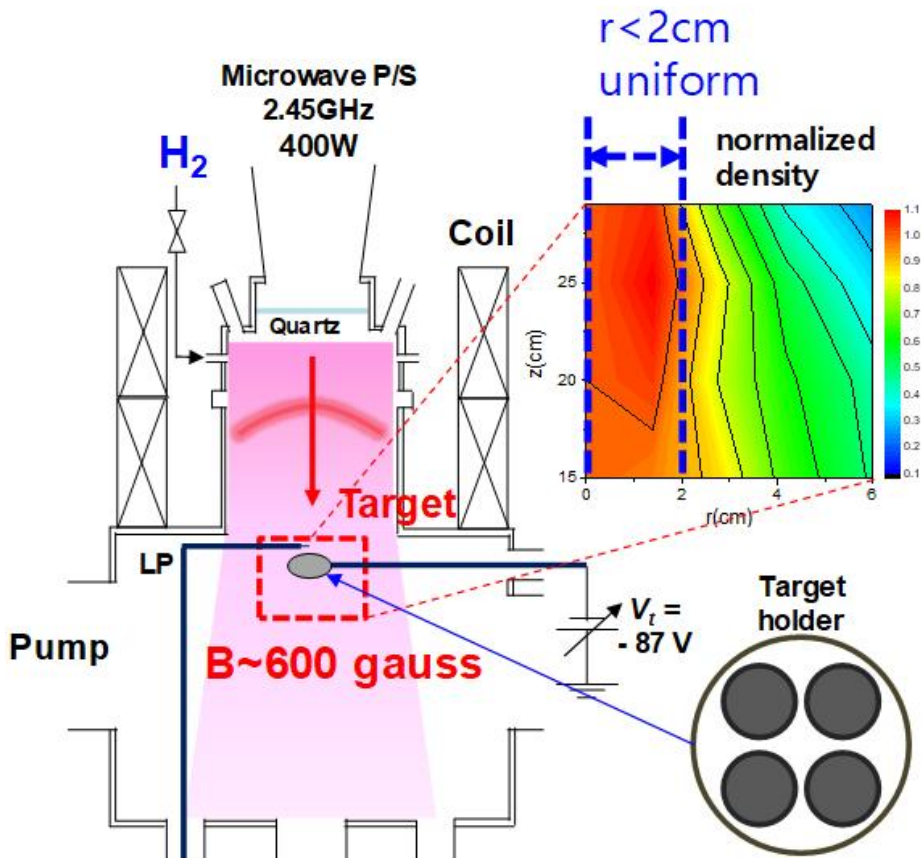


Figure 3.3. A schematic diagram of electron-cyclotron-resonance (ECR) plasma source. A 2.45 GHz microwave is injected through the upper window and makes resonance at $B = 875$ gauss surface. There exists a uniform density region at $r < 2$ cm and a 3.5-cm-diameter target holder is located in the region.

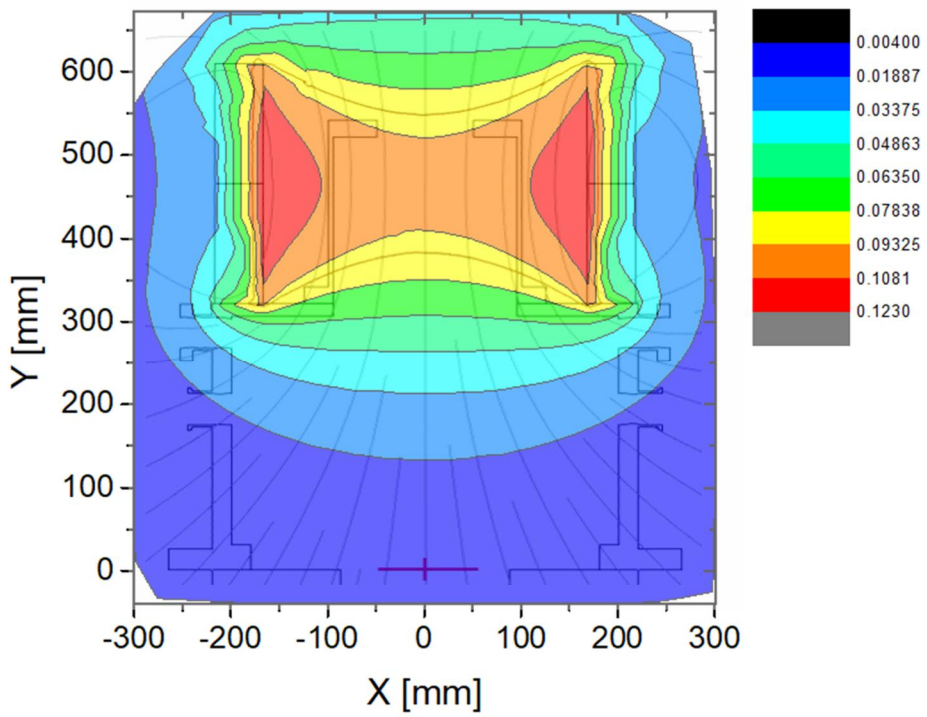


Figure 3.4. A configuration of typical magnetic field line in ECR plasma source. The geometrical divergence of the central ($r < 2$ cm) field line is less than 2 degree near the source chamber – diffusion chamber interface.

Hydrogen gas was injected into the chamber through the gas feedthrough located at the top plate of the source chamber and the operational neutral gas pressure was set to be 2.5 mTorr (base pressure was below 2×10^{-6} Torr). Electron density, n_e , and electron temperature, T_e , measured by using a Langmuir probe were $2.1 \times 10^{17} \text{ cm}^{-3}$ and 5 eV, respectively, at a delivered microwave power of 400 W. Hydrogen ions consist of three kinds of ion species: H^+ , H_2^+ , and H_3^+ . Concentrations of those ion species were calculated using a global balance model [42] for the given chamber geometry and input power. It was found that the concentration of H_2^+ ion dominated at the given operational condition. Some important parameters for the above experimental conditions are summarized in the table 3.2.

Table 3.2. Plasma parameters of ECR plasma source used in this study

λ_c	λ_m	r_{cs}	λ_d	Λ_{cm}	Λ_{dm}
col. MFP	ion gyro-radi.	gyro-radi. with Cs	Debye length	λ_c / λ_m	λ_d / λ_m
61 (mm)	0.76 (mm)	5.4 (mm)	43 (μm)	80 Weakly- collisional	0.057 $\ll 1$

Four graphite targets were installed in the chamber carried by a target holder made of stainless steel (see, figure 3.3). Since, the plasma potential was typically ~ 13 V, the target was negatively biased at - 87 V with respect to the ground potential so that ions could gain 100 eV at the target surface while traversing the sheath and presheath. Because the geometrical configuration of the magnetic field line of the plasma source

cannot be tilted, the target was tilted in order to change the magnetic field angle on a target surface. The geometrical tilt angle of the target, ψ , which was the angle between the surface normal direction of the target \vec{n} and the magnetic field \vec{B} , was controlled over 0° , 20° , 40° , 60° , 80° , and 85° . The angle, $\psi = 0^\circ$, indicates that the magnetic field line is parallel to the surface normal direction and the angle, $\psi = 85^\circ$, indicates a grazing configuration of the magnetic field line to the surface tangential. Figure 3.5 shows the oblique tilt angle of 80° to the magnetic field line as an example.

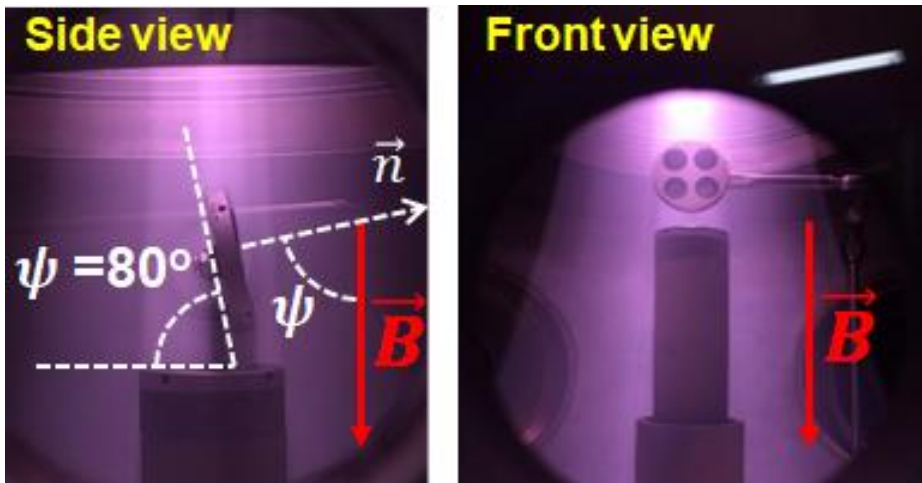


Figure 3.5. A side view and a front view of the target holder. In this figure, the magnetic field angle, ψ , is 80° which forms an grazing angle with the tangential direction of the target surface.

Although the ion flux along the magnetic field, $G_{B//}$, is identical for all tilt angles, the depositional ion flux, G_{dep} , which is defined as

$$G_{dep} = G_{B//} \cos \psi, \quad (3.1)$$

varies for each geometrical tilt angle of the target. Because the etch rate of the graphite surface is proportional to the depositional ion flux, the irradiation time, t_{irr} , was controlled to maintain depositional ion fluence to be constant as

$$\Gamma_{dep} \times t_{irr} = \Gamma_{B//} \times \cos \psi \times t_{irr} = \text{const.} \quad (3.2)$$

Therefore, the irradiation time was controlled to be proportional to $1/\cos \psi$ for each geometrical tilt angle of the target. In this study, the irradiation time for $\psi = 85^\circ$ (grazing incident) condition is controlled approximately 11 times larger than the irradiation time for $\psi = 0^\circ$ (vertical incident) condition.

3.2. Emissive probe for sheath potential measurement

Although the electron density, temperature and plasma potential can be successfully measured by using the Langmuir probes (LPs), the potential distribution inside the sheath region cannot be measured by using the Langmuir probe because the potential distribution is severely perturbed by the insertion of the Langmuir probe in the sheath region. When the Langmuir probe is immersed into the plasma sheath, formed by a larger wall as shown in figure 3.6, the electric field of the sheath region is concentrated in between the probe tip and the wall, so that the sheath structure is broken. At the same time, for the measurement of potential distribution in the presheath region where the spatial gradient of the space potential is weak, the Langmuir probe measurement cannot also achieve a fine resolution for the space potential distribution because there always exists an uncertainty in the reading of space potential from the current-voltage characteristic curve that is obtained from the Langmuir probe measurement.

In this study, the potential distribution of the sheath structure formed in front of the negatively-biased target was measured by using emissive probes (EPs). It has been reported that the emissive probe is the only available diagnostic method that can measure the space potential distribution in DC plasmas, RF plasmas [44], pulsed plasmas [45], magnetized plasmas [31], tokamak plasmas [46], etching/ashing plasmas [47,48], and even in the vacuum space [49,50]. It also has been used widely to measure the subtle distribution of the sheath potential in numerous researches.

The emissive probe utilizes the electron emission characteristic from the heated tungsten wire (> 2000 K) with respect to the potential difference between the wire and the space potential near the probe. The electrons are emitted from the wire when the

space potential (V_s) is higher than the bias potential of wire (V_b). Then the space potential is lower than the bias potential, the electrons are not emitted from the probe. Therefore, by scanning the probe bias voltage and measuring the step-wise emission current, the space potential can be detected in principle. In reality, on the other hand, it is quite difficult to determine space potential. The current signal formed by the collection of plasma electrons and ions distorts the emission current signal. The thermal energy of emitted electrons (~ 0.2 eV) makes the stepwise characteristic of the emission current to a continuously-varying characteristic (see, figure 3.7). The potential difference between two ends of the electron-emitting filament that forms the heating current of the filament also contributes to form an un-stepwise emission current characteristic.

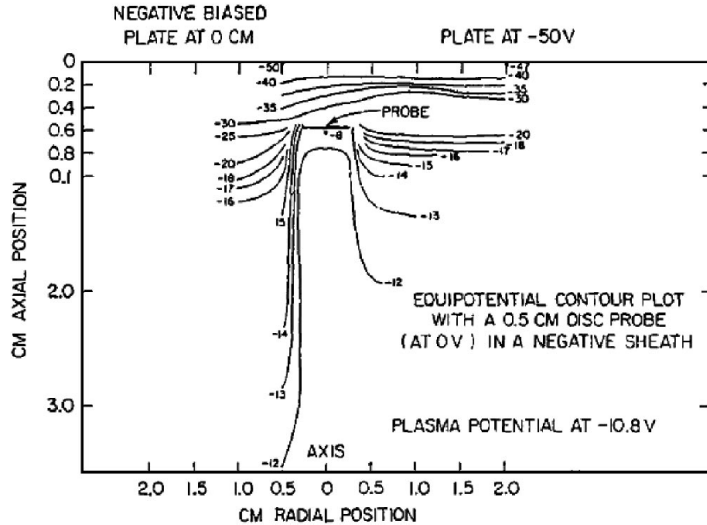


Figure 3.6. Equipotential contours near a 0.5-cm-diameter planar Langmuir probe biased at 0 V. The probe was positioned 0.6 cm from a plate biased at -50 V.

It shields out the sheath electric field of the plate and perturb the potential profile.

[51]

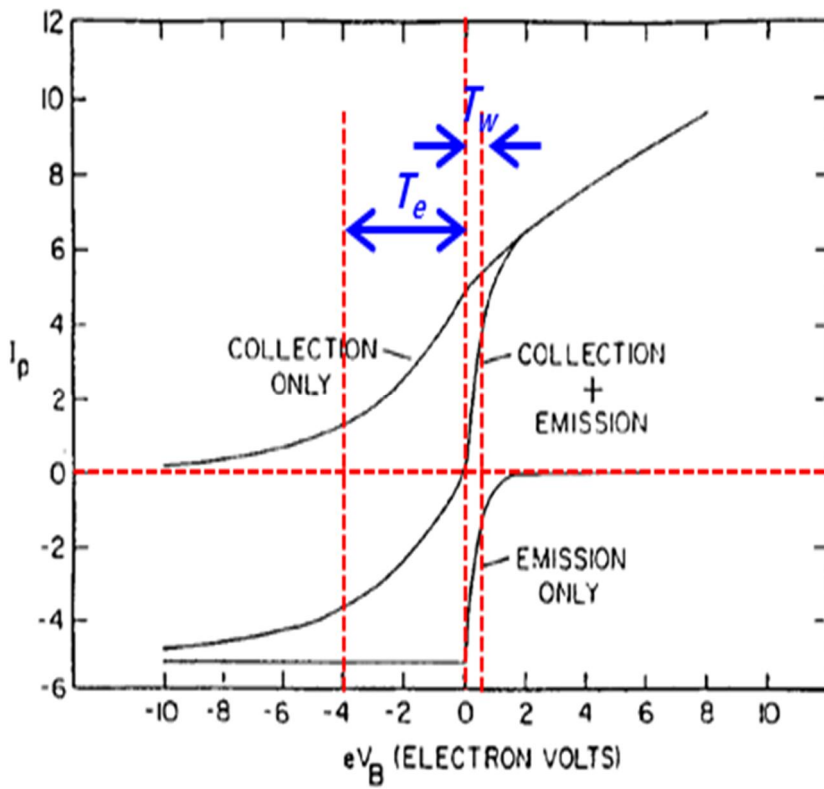


Figure 3.7. Typical I-V (current-voltage) characteristic curve obtained by an emissive probe. The curve consists of the collection current, originated from the incidental flux of the charged particles in the plasma, and the emission current. [55]

Two distinctive methods were developed to measure the space potential. The one is called the floating-point method (FPM). As shown in figure 3.8, the floating-point method utilizes the characteristic that the floating potential of I-V characteristic curve goes toward and saturates at the space potential (or plasma potential) as the emission current increases (i.e. as the temperature of the filament increases by increasing the heating current).

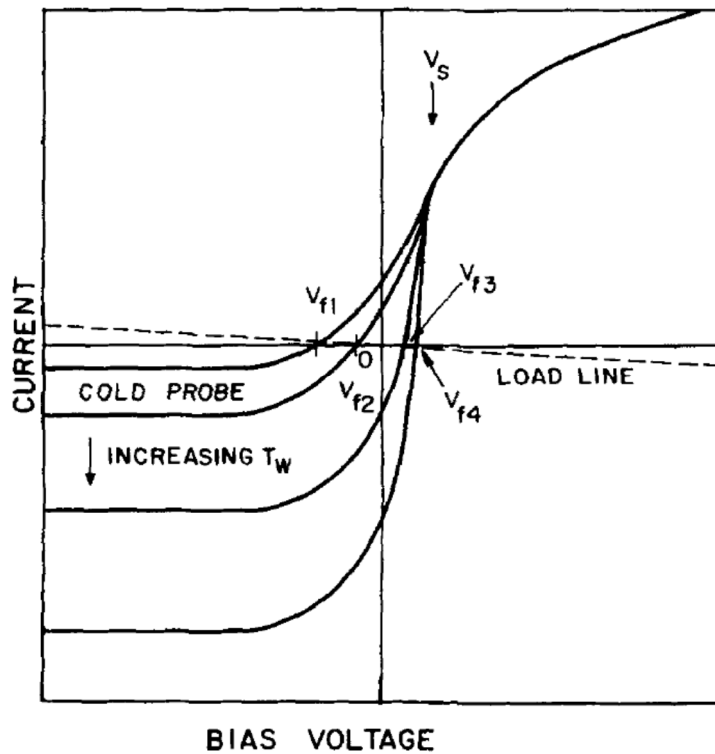


Figure 3.8. Floating-point method for the measurement of space potential. As the emission increases, the floating potential of the I-V characteristic curve of the emissive probe goes toward and saturates at the space potential. [56]

In the practical use of this method, the emission current is usually fixed to a high value enough to the floating potential saturate at the plasma potential and it is used to measure the temporal fluctuation of the plasma potential. But because the strong emission from the probe changes the local space potential near the probe, this method is not proper for the measurement of the spatial potential distribution. The accuracy for the potential measurement of this method is known to be as small as $T_{e,eff}/e$ [53,54]. The electrical resolution is known to be 0.1 V [55] but physically T_w/e is appropriate [53]

The other one is the inflection-point method (IPM). As shown in the figure 3.9 and figure 3.10, the space potential near the emissive probe is slightly decreased as the emission current from the probe is increased and the inflection point of the I-V characteristic curve tend to be decreased. By measuring the potential of the inflection point at several different emission currents and fitting those points to a line, one can find the plasma potential that is not affect by the emission current at the intersection of the x-axis as shown in figure 3.10. Therefore, this method is called as the inflection-point method operated in the limit of zero emission. Because of this characteristic, the inflection-point method is widely used to measure the delicate spatial variation of the space potential distribution, especially the spatial potential distribution of plasma sheath region. The accuracy and resolution of this method is known to be $T_w/e \sim 0.2$ V [53]. These characteristics of the floating-point method and the inflection-point method are summarized in the table 3.3.

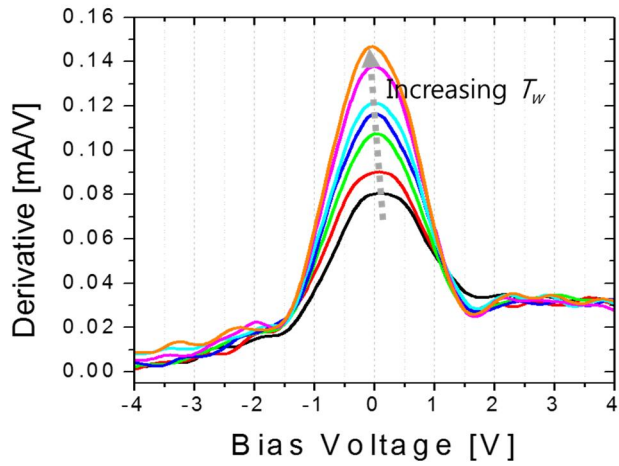


Figure 3.9. The inflection-point method (IPM) for the determination of the plasma potential. The inflection-point of the derivative of the I-V characteristic curve tend to decrease as the emission current increases.

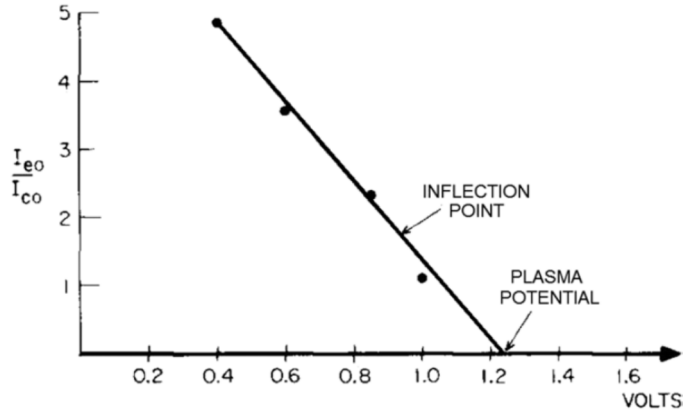


Figure 3.10. The inflection-point method operated in the limit of zero-emission [55]. As the saturation current of emission current (I_{e0}) to the saturation current of collection current (I_{c0}) decreases, the inflection point goes toward the plasma potential.

Table 3.3. Characteristics of the floating-point method and inflection-point method

Method	Uncertainty (Resolution)	Characteristics
Inflection Point Method	$T_w/e \sim 0.2 \text{ V}$ $(T_w/e \sim 0.2 \text{ V})$	* fast ($\tau > \tau_{RC}$) measurement (time-resolved measurement) * operation in the limit of large emission
Floating Point Method	Few $T_{e,eff}/e$ $(T_w/e \sim 0.2 \text{ V})$	* accurate measurement * steady state sheath measurement * operation in the limit of zero emission

In this study, we utilized the inflection-point method limited in a zero-emission to measure the electric potential distribution in the plasma sheath and presheath region. The probe tip was made with a 2 % thoriated tungsten wire of which the diameter is about 0.025 mm (1 mil.) and the length is 5 mm. The thoriated tungsten has a small work function and it makes the filament emit thermionic electrons at colder wire temperature. The emissive probe was installed on a linear motion guide rail and the position in front of the negatively biased target was controlled by using the step motor (see, figure 3.1). The absolute resolution of the linear motion guide rail was $< 100 \mu\text{m}$. The heating current of the filament was controlled over 6 steps in order to change the emission current. The heating current was supplied from a lab-made current supplier, shown in figure 3.11, and controlled by the Labview based DAQ software.

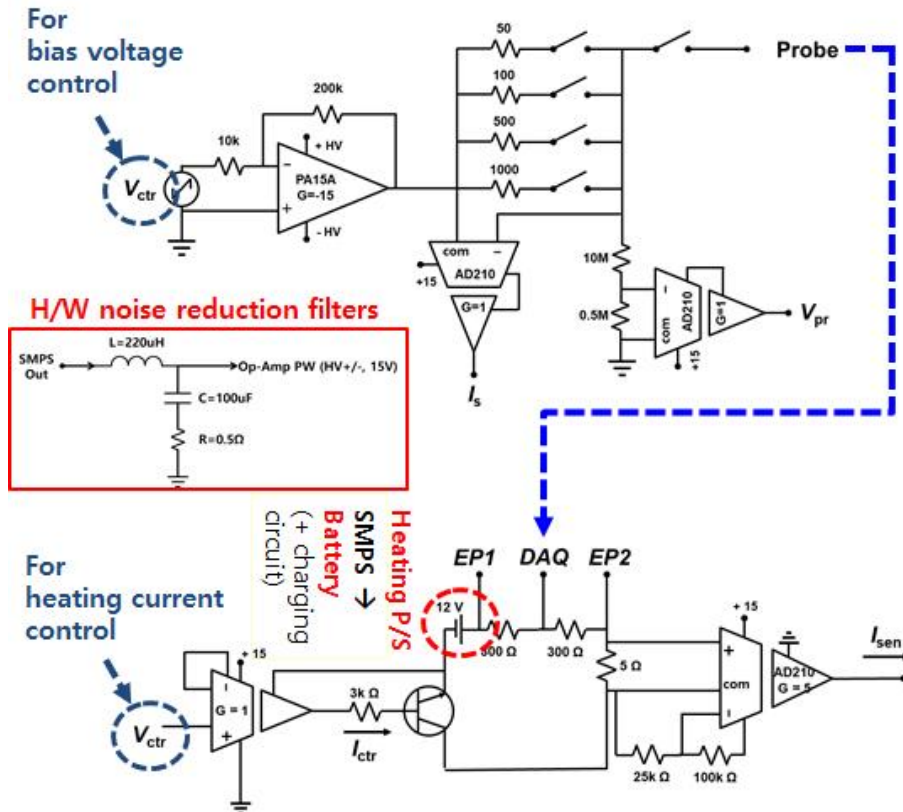


Figure 3.11. Circuit diagram of (lower) the heating current supplier for the emissive probe and (upper) the I-V characteristic measurement circuit board. All the control of heating current, sweeping voltage and measurement of I-V were controlled by a Labview®-based lab-made software. A noise reduction filter was used to supply a noise-free power to the operational amplifiers.

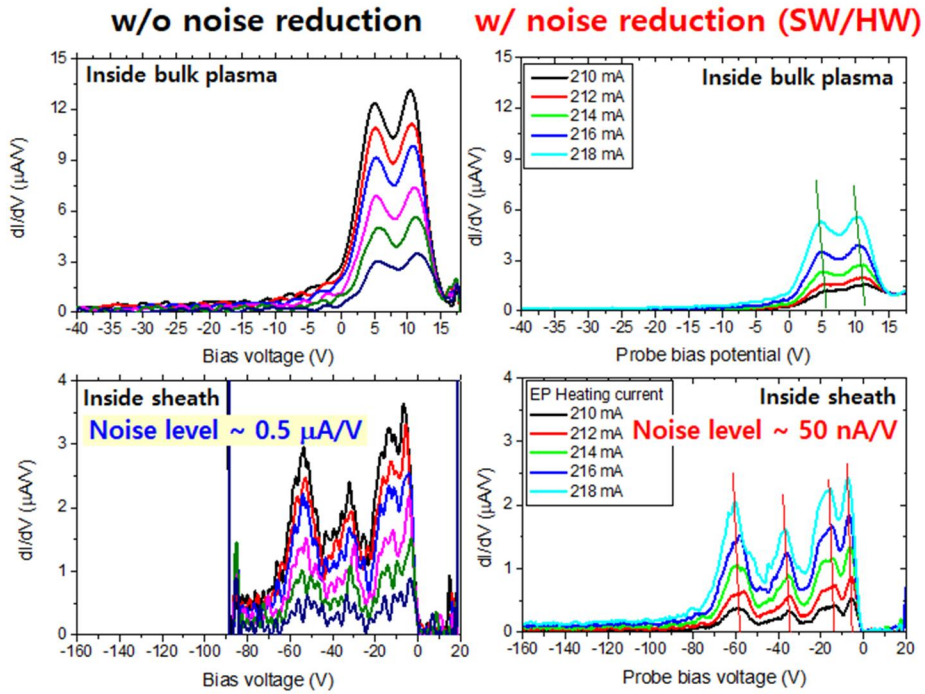


Figure 3.12. Examples of typical dI/dV curve obtained by emissive probes. By applying a noise reduction circuit to the power supplier for operational amplifier, much higher signal-to-noise ratio can be achieved even at lower emission current.

3.3. Laser-induced-fluorescence ion velocity measurement

The laser-induced-fluorescence (LIF) method was utilized to measure the ion fluid velocity and the ion velocity distribution function itself. Like the emissive probes that can measure the distribution of space potential in the sheath region without perturbing the potential structure, the laser-induced-fluorescence method is a non-invasive method that can measure the ion velocity distribution function without perturbing the ion dynamic characteristics.

The LIF method uses a characteristic that an ion excited to an upper level by a laser light of wavelength, λ_1 , is spontaneously decayed into a lower level with emitting different wavelength, λ_2 . For an ion that moves with velocity, \vec{v} , in the direction of laser incidence, \vec{k} , however, the wavelength of the laser should be shifted in order to excite the ion to the upper level. The wavelength shift needed to excite the moving ion is determined as following Doppler shift relation.

$$2\pi\Delta\nu = 2\pi(v_1^* - \nu_1) = 2\pi c \left(\frac{1}{\lambda_1^*} - \frac{1}{\lambda_1} \right) = \vec{v} \cdot \vec{k} = v_{\parallel} k \quad (3.3)$$

In Eq. (3.3), λ_1 and ν_1 denote a laser wavelength and frequency to excite ions at rest to a upper level and λ_1^* and ν_1^* denote the Doppler-shifted wavelength and frequency to excite moving ions. Therefore, by measuring the fluorescence signal with respect to the wavelength of the laser, the ion velocity distribution can be measured.

Because the laser-induced excitation from the ground state of ion species needs a wavelength in ultra-violet range, there have been developed several LIF schemes that utilize laser wavelengths in visible-range. They utilize ion species in metastable state.

Various laser-induced-fluorescence schemes for argon ion metastables that utilize visible wavelengths are summarized in Table 3.4 [57].

Table 3.4. Various LIF schemes used for ion velocity measurement [57]

Scheme No.	Metastable state	Fluorescence transition	λ_{12} (nm)	λ_{23} (nm)	A_{12} (10^8 s^{-1})	A_{23} (10^8 s^{-1})	β_{23}	Δv (m/s)
1	$3d' \ ^2G_{9/2}$	$4p' \ ^2F_{7/2}^0 - 4s' \ ^2D_{5/2}$	611.66	461.08	0.200	0.789	0.665	12.2
2	$3d \ ^4F_{7/2}$	$4p \ ^4D_{5/2}^0 - 4s \ ^4P_{3/2}$	668.61	442.72	0.107	0.817	0.616	7.2
3	$3d \ ^4F_{9/2}$	$4p \ ^4D_{7/2}^0 - 4s \ ^4P_{5/2}$	664.55	434.93	0.147	1.171	0.810	9.8
4	$3d \ ^4F_{7/2}$	$4p \ ^4D_{7/2}^0 - 4s \ ^4P_{5/2}$	688.85	434.93	0.009	1.171	0.810	0.6
5	$3d' \ ^2G_{7/2}$	$4p' \ ^2F_{7/2}^0 - 4s' \ ^2D_{5/2}$	612.51	461.08	0.009	0.789	0.665	0.5
6	$3d \ ^4D_{7/2}$	$4p \ ^4P_{5/2}^0 - 4s \ ^4P_{5/2}$	440.22	480.74	0.304	0.780	0.574	13.4

A_{12}, A_{23} : absolute spontaneous transmission probability

β_{23} : branching ratio for the fluorescence transition

Δv : intrinsic minimum velocity resolution

The selection of LIF scheme relies on various considerations. The first is population of the target metastable state ion. The population is determined by the equilibrium between the generation and loss but those may be different for different discharge sources. For the DC filament discharged multi-dipole sources, the lifetimes of argon metastable ions are summarized in Table 3.5. In the table, it can be found that the lifetime of the metastable state ions are quite similar to each other, because of similar threshold energy between each other. Because the excitation transition to metastable states is done by mono-energetic ($\sim 60 \text{ eV}$) primary electrons in multi-dipole plasma source, small ($< 3 \text{ eV}$) difference in threshold energy can be neglected.

Table 3.5. Lifetime of argon ion metastable state

Ground state	Metastable state	Threshold energy (eV)	Lifetime (μsec)	Ref.
$3p^5 \ ^2P^0_{3/2}$		15.8		
	$3p^5 \ ^2P^0_{1/2}$	16.0	18.9×10^6	28
	$3d \ ^4D_{7/2}$	32.2	> 10	36
	$3d \ ^4F_{9/2}$	33.4	> 10	36
	$3d \ ^4F_{7/2}$	33.5	> 10	36
	$3d \ ^2F_{7/2}$	34.3	> 10	36
	$3d' \ ^2G_{9/2}$	34.9	> 10	36
	$3d' \ ^2G_{7/2}$	34.9	> 10	36
	$3d' \ ^2F_{7/2}$	36.1	> 10	36

The second consideration is the transmission probability, or the Einstein coefficient for spontaneous decay, A_{12} . The suffix 1 denotes the ground level of metastable state ions and the suffix 2 denotes the laser-induced excited state from the metastable state. Although the coefficient, A_{12} is for the decay from the upper level, the larger the coefficient is, the more possible the laser-induced excitation (reversal process) happens.

The third consideration are the decay coefficient, A_{23} , and the branching ratio b_{23} . Those determines how many excited ions decay while emitting expected fluorescence wavelength in short decaying time. Because there are other branches of the decay from the laser-induced excited state, the larger the branching ratio is, the better signal-to-noise level of the fluorescence light. When the decay coefficient, A_{23} (sec^{-1}), is small (or smaller than target radio-frequency, for example), light emission happens quite later than the time when laser-induced excitation happens, and therefore the fluorescence signal may be delayed both temporally and spatially (especially for

moving ions). Therefore, the larger the decay coefficient, A_{23} is, the easier the spatial/temporal velocity properties can be determined.

The last consideration is the laser availability. Two tunable laser systems are commonly used for LIF ion velocity measurement. One is the dye laser system pumped by a pulsed Nd:YAG laser and the other is the tunable diode laser system. The two systems have quite different characteristics. The dye laser system utilizes dye solution that can lasing various wavelengths. By changing the grating angle between laser cavity, one can tune the wavelength. The tuning range for a single dye solution is around 10 nm, but the total tuning range of the laser can be achieved upto 500 nm by changing the dye. The linewidth of the dye laser, however, is quite large, which is around 2 pm. Because the Doppler broadening width of the ion velocity distribution is similar to the linewidth of the laser, the LIF signal obtained by using the dye laser system shows convoluted characteristic of laser broadening and Doppler broadening. On the other hand, the tunable diode laser the laser linewidth is $\sim 1/100$ times smaller than the ion velocity distribution, the LIF signal directly corresponds to the ion velocity distribution. The characteristics of the laser systems are summarized in Table 3.6.

Table 3.6. Comparison between dye laser and diode laser

	Operation	Wavelength selectivity	Tuning range	Linewidth
Dye laser	Pulsed	Selectable	~ 500 nm (Dye)	large
pulsed Nd:YAG	~ 10 nsec	by use of different dye	~ 30 nm (grating)	~ 2 pm

				Small
Diode laser	CW	Fixed	< 10 nm	~ 0.001 pm
				~ 100 kHz

In our experiments, we utilized the tunable dye laser system for the ion fluid velocity measurement. Goekner [58,59] showed that if the ion velocity distribution is not severely different from the drifting Maxwellian distribution, the fluid velocity can be measured from the peak wavelength of the LIF signal. For the investigation of the RF field effect on the ion temperature, we utilized the tunable diode laser system.

The LIF schemes for the argon ion velocity measurement used in our experiments are represented in figure 3.13. For the use of dye laser, we tuned laser wavelength near 611.662 nm and detected the fluorescence light of 461.086 nm. For the use of diode laser, we tuned laser wavelength near 668.614 nm and detected the fluorescence light of 442.724 nm. The LIF schemes for xenon ion velocity measurement used in our experiments are represented in figure 3.14. A laser centered at 605.1 nm excites ion metastables to upper level and fluorescence signal of 529.2 nm was detected. By using a dye complex of Rhodamine B and Rhodamine 640, which can emit laser light from 598 nm to 636 nm, velocities of both argon ion and xenon ions can be measured without changing dye solution (figure 3.15).

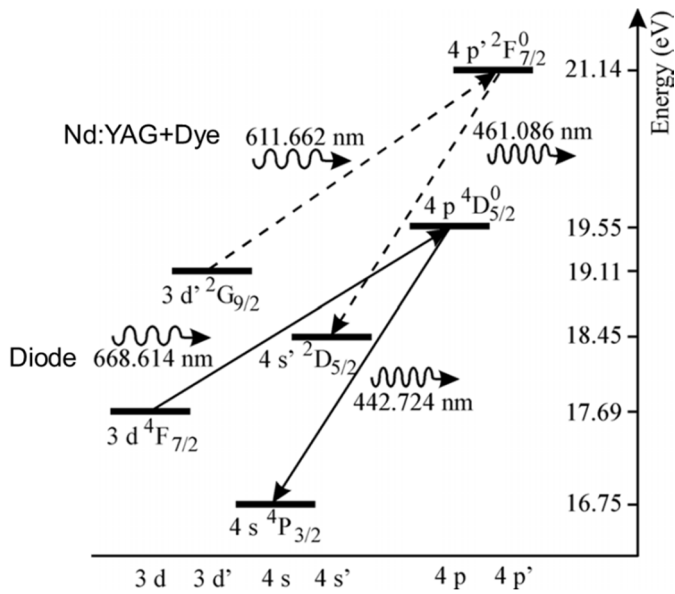


Figure 3.13. Ar^+ ion LIF scheme used in this research.

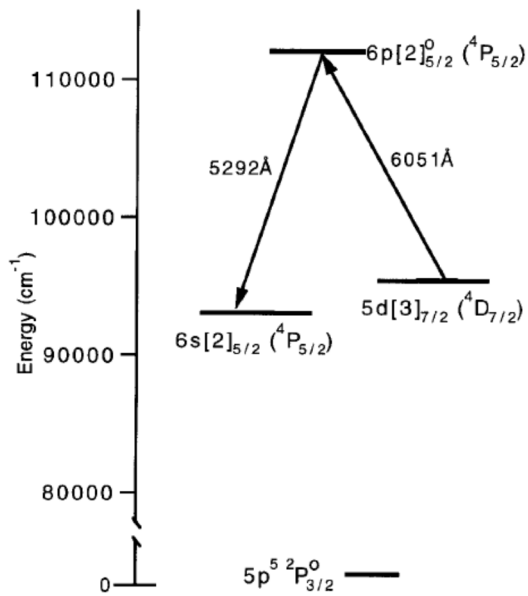


Figure 3.14. Xe^+ LIF scheme used in this research [60].

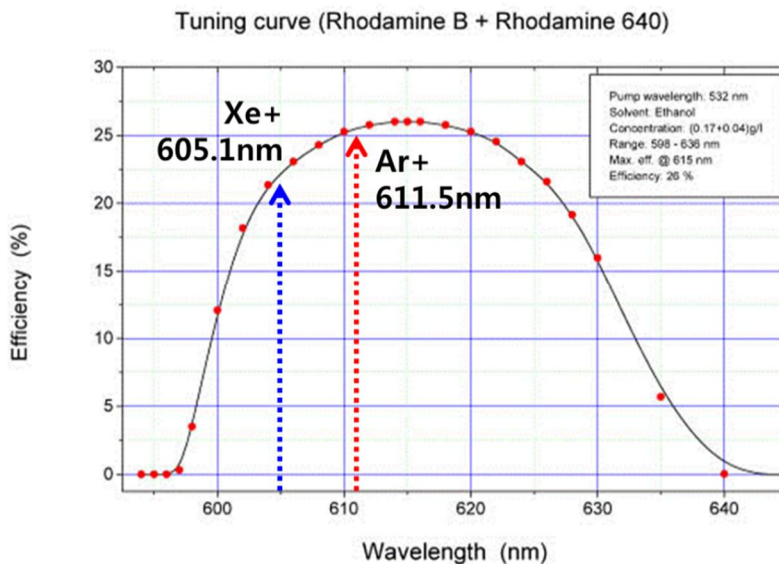


Figure 3.15. Efficiency of dye laser with using a combination of Rhodamine B and Rhodamine 640 dye solution

In figure 3.16, detailed experimental setup for tunable diode laser-induced-fluorescence measurement method is represented. The laser light is emitted from the laser head and sampled into wavelength meter by 2 % beam sampler. The main beam is expanded by passing through a couple of planar-concave and planar-convex lenses in order to enlarge reaction volume in the plasma. The beam expander was installed to make a focal point outside the chamber and a pinhole was installed at the focal point in order to eliminate peripheral light and to remain the main laser beam. The laser light beam after passing through the pinhole was slightly expanded but the expansion angle was less than 1° . A window was installed to form an oblique angle to reduce the scattered light from the window. Some scattered light from the window, even using the angled window, were reduced by using baffle configure. A stack of razor blades was

installed at the center of the target to prevent the reflection from the target. The LIF signal was detected at the perpendicular direction so the Doppler shift effect of the fluorescence light can be neglected. Because the LIF light intensity is extremely weak, the light was picked up and converted into an electrical signal by using the photo-multiplier tube. After the light was picked up by the photo-multiplier tube, the signal to noise level was enhanced by using the lock-in-amplifier which was triggered at the laser chopper frequency. A viewing dump, consist of a stack of cutter blades was installed at the bottom of the chamber to prevent picking up the reflected fluorescence light. All control of the wavelength tuning of the laser, moving the detection module, and the data acquisition including oscilloscope control was done by lab-made software by using Labview ®. In figure 3.17, an experimental setup for laser-induced-fluorescence by using the pulsed Nd:YAG and dye laser source was represented. The apparatus was the same to figure 3.16, except for the use of Nd:YAG and Dye lasers. Because the energy of the pulsed laser (Pulsed, ~ mJ per 10 nsec pulse) is much larger than that of the diode laser (CW, ~ mW) the LIF signal was averaged over 300 times at the oscilloscope (Boxcar-average-relevant). A beam dump was installed behind the target to prevent reflection of the laser.

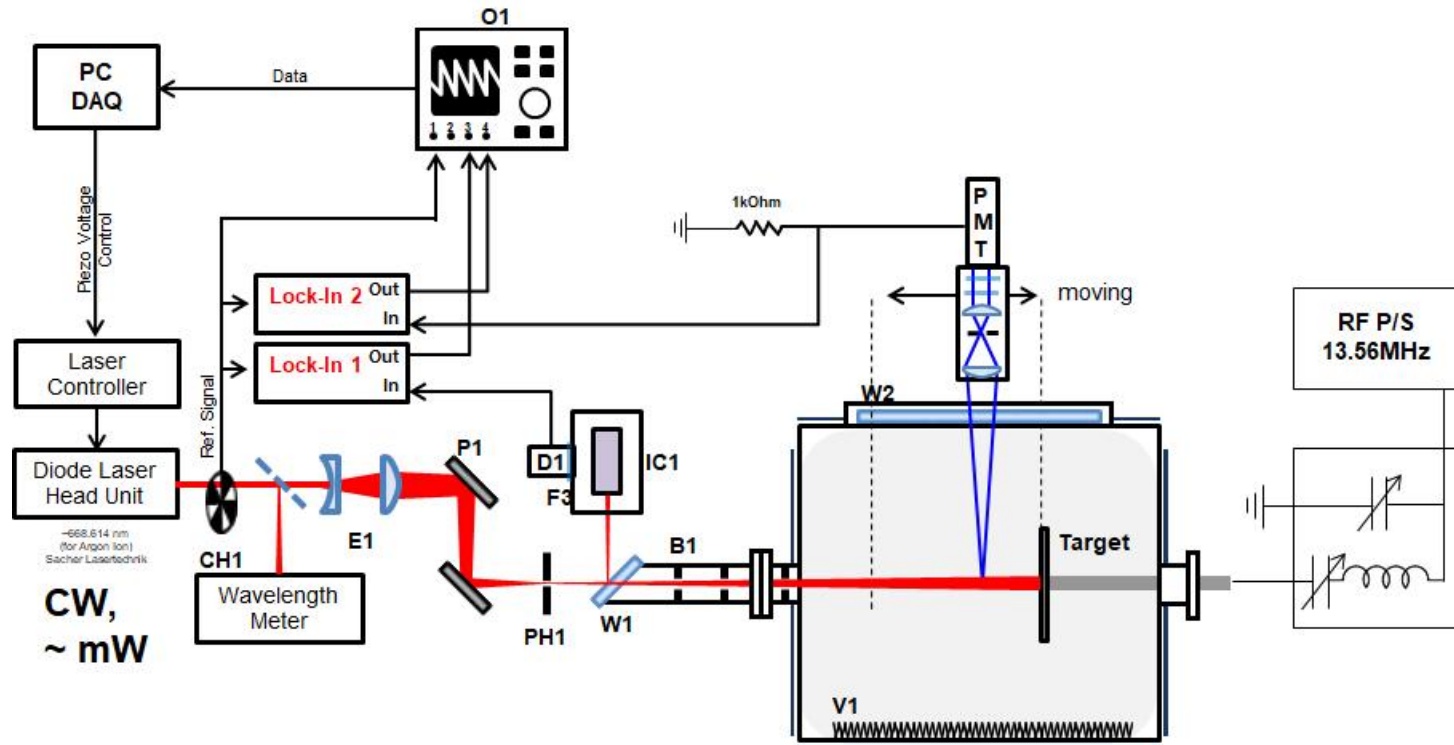


Figure 3.16. Experimental apparatus for the laser-induced-fluorescence ion velocity measurement by using a tunable diode laser. Because of the weak laser power (~ 10 mW), the laser is modulated to the chopper frequency and the modulated LIF signal is amplified by using a lock-in-amplifier.

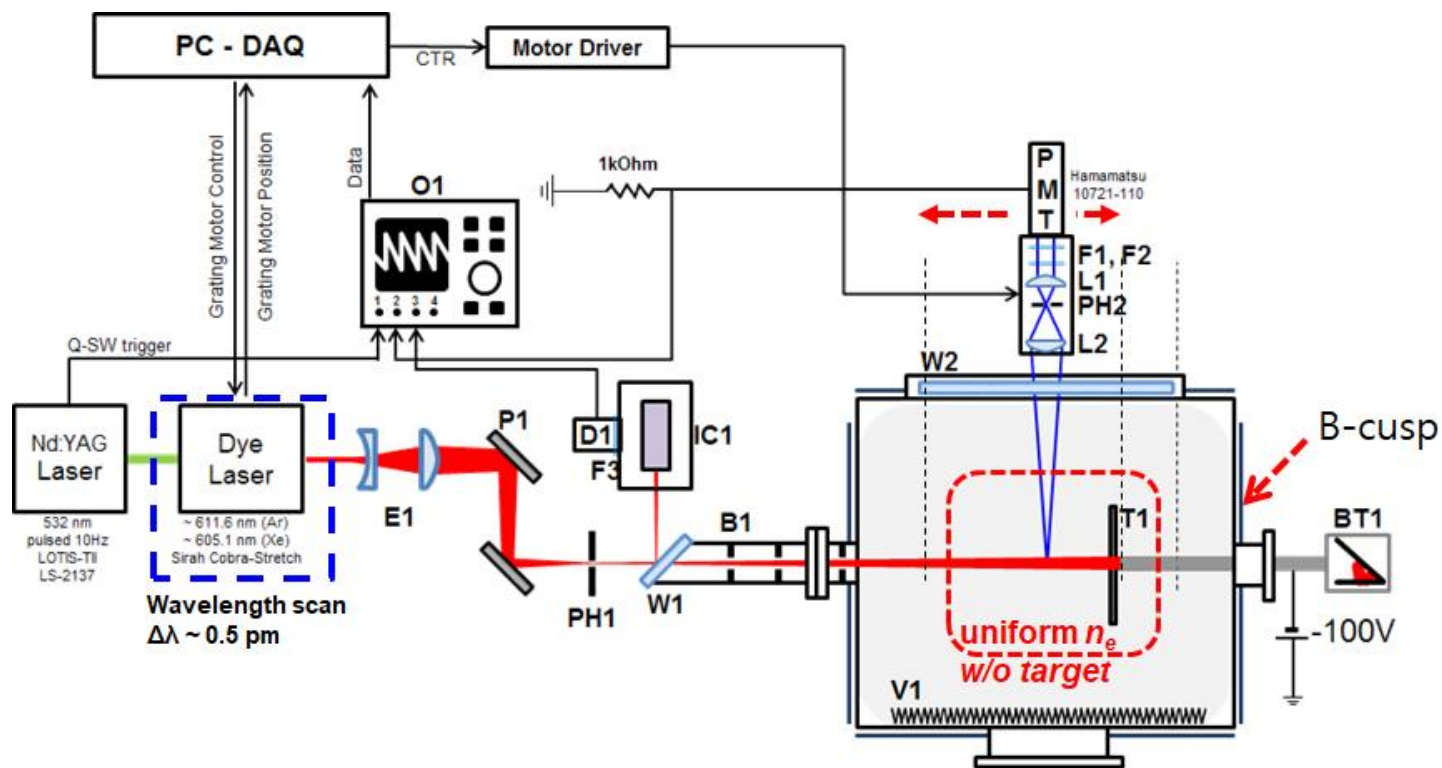


Figure 3.17. Experimental apparatus for the laser-induced-fluorescence ion velocity measurement by using a tunable dye laser. For the use of a high-power pulsed dye laser the LIF signal was averaged in a oscilloscope to achieve high signal-to-noise ratio, which corresponds to the boxcar average method.

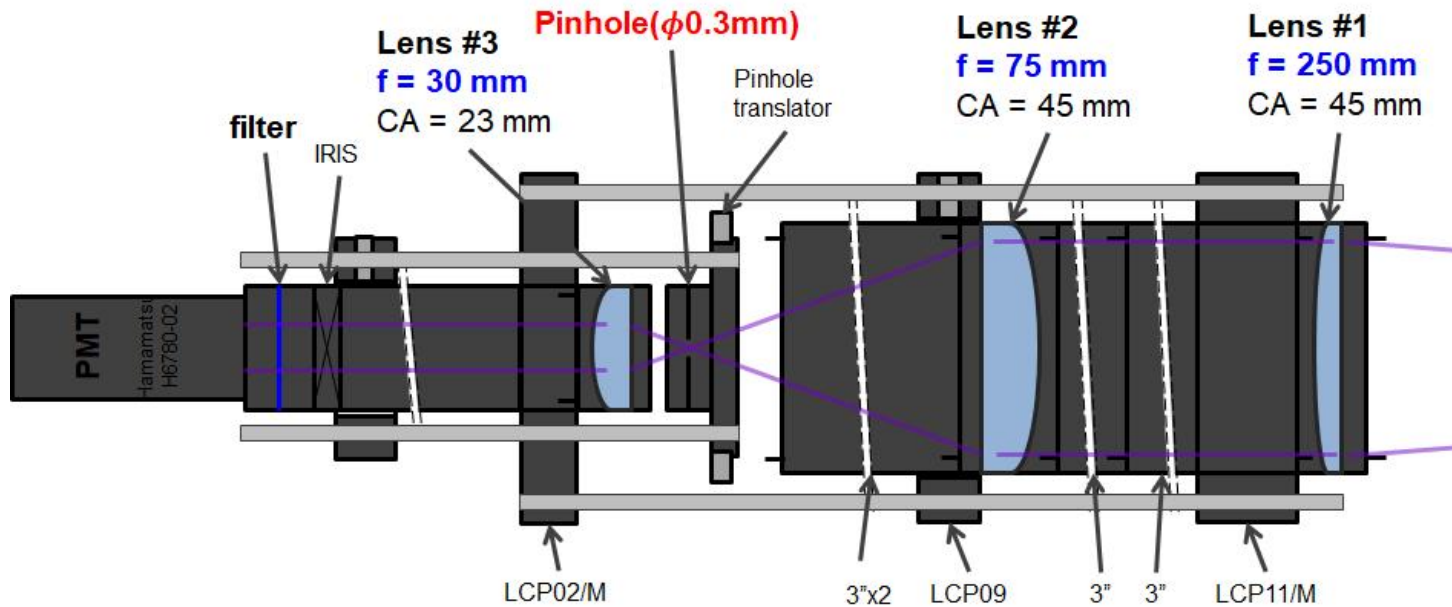


Figure 3.18. Optical detection module used for LIF measurement in our experiment. By using aspheric lenses, spatial resolution can be achieved. A slit ($0.3 \text{ mm} \times 3 \text{ mm}$) can be used instead of pinhole and it enhances signal-to-noise ratio without changing 1-dimensional spatial resolution along the target axis.

The detection module of the LIF measurement can be shown in figure 3.18. Because the photo-multiplier detector collects total incident light, the detection module was configured to be 3-f configuration, in which one end of the detector has infinite focal length and the other end has a focal length relevant to the position of the detection object. We used 2-inch lens to collect fluorescence light and the final size of the collection area was designed to become the same size of the entrance window of the photo-multiplier tube. A pinhole or a slit was placed at the second focal point between lens #2 and lens #3 in the figure 3.18 to make good spatial resolution. The spatial resolution of our detector module was calculated as around 1 mm theoretically. An optical bandpass filter whose wavelength was centered at the wavelength of the fluorescence light and the bandwidth of 0.6 nm was installed in front of the photo-multiplier tube in order to reduce background light coming from the plasma and ambient.

3.4. Material probe for ion incident angle measurement

The ion incident angle on a plasma-facing surface was measured by analyzing the etching profile on a graphite by incident hydrogen ions. When the graphite surface is exposed to hydrogen plasmas, the energetic hydrogen ions and neutral hydrogen atoms can etch the surface through a physical and chemical reaction [61] while nano-scale tips are formed on the surface as seen in Figure 3.19. The mechanism of such tip formation is not fully understood yet [62-65]. However, we found that when the graphite surface was exposed to the helium plasma instead, nano-scale tips were not formed on the surface. This means that these conical tips are formed by reactive ion etching mechanism, by which the surface morphological pattern is formed along the incidental direction of ions. Therefore, by measuring the inclined angle of nano-tips, the ion incident angle can be determined.

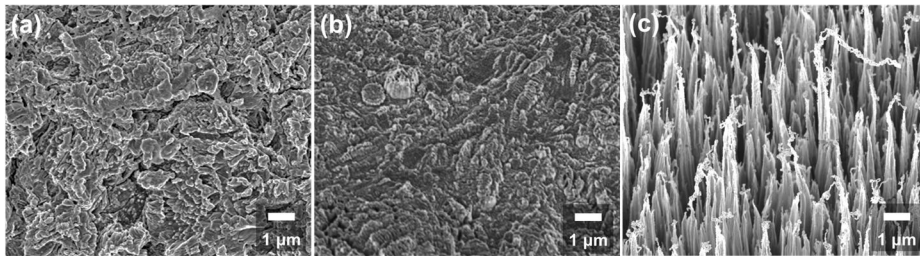


Figure 3.19. Scanning electron microscope (SEM) images of the surface of (a) pristine, (b) helium ion irradiated, and (c) hydrogen ion irradiated graphite targets. Images are taken with the tilt angle of 30° with respect to surface normal direction.

The inclined angle of nano-scaled tips was measured from scanning electron microscope (SEM) images. Images were taken with the tilt angle of 30° with respect to surface normal direction of the target. The seeming angle (for example, seen at Figure 3.19(c)) is not the morphological tilt angle of nano-tips because nano-tips that are formed along the ion incidental direction have 3-dimensional shape with respect to the magnetic field line, the surface normal direction, and the $E \times B$ direction. Therefore, we took SEM images of nano-tips in two orthogonal directions as shown in Figure 3.20. The two seeming tilt angles of nano-tips, θ_1 and θ_2 , were measured to calculate the morphological tilt angle of nano-tips, θ_{tip} . Assuming that the direction vector of the nano-tip is (a, b, c) , vector elements a and b are related to θ_1 , θ_2 , and $\theta_{SEM} = 30^\circ$ as

$$\tan \theta_1 (a \cos \theta_{SEM} + \sin \theta_{SEM}) = b \quad (3.4)$$

and

$$\tan \theta_2 (b \cos \theta_{SEM} + \sin \theta_{SEM}) = a. \quad (3.5)$$

Here, the third vector element c is set to be unity. By solving Eqs. (3.4) - (3.5), the two vector elements, a and b , can be obtained and thus the 3-dimensional tilt angle of nano-tips, θ_{tip} , can be obtained as

$$\theta_{tip} = \tan^{-1} \left(\sqrt{a^2 + b^2 + 1} \right). \quad (3.6)$$

Tilt angles of nano-tips were measured over hundreds of nano-tips and the average angle was used in this paper.

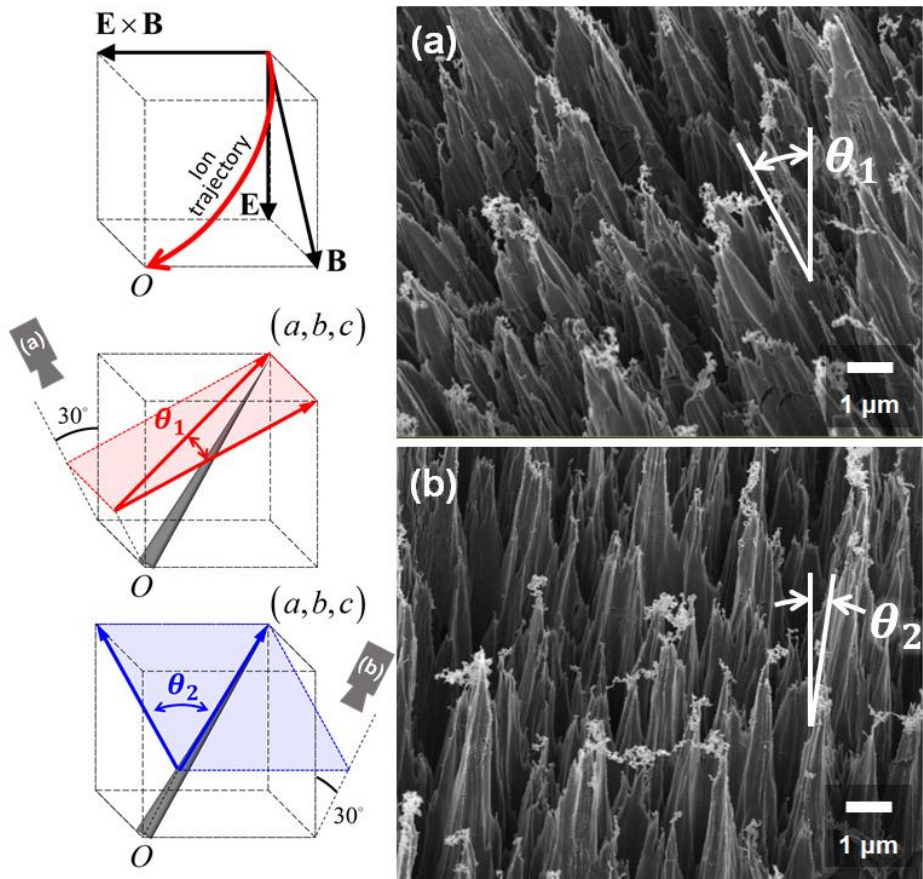


Figure 3.20. Scanning electron microscope images taken in two orthogonal directions. The tilt angle of nano-scaled tips, θ_{ip} , can be obtained from the seeming tilt angles, θ_1 and θ_2 , that are taken at two orthogonal imaging directions.

3.5. Ion acoustic wave measurement for ion concentration

The ion concentration was measured by the ion acoustic wave measurement method (using Eq. (3.7)) with a support of a Langmuir probe measuring the electron temperature [66-72].

$$v_{ph} = \sqrt{\frac{n_1}{n_e} C_{s1}^2 + \frac{n_2}{n_e} C_{s2}^2} = \sqrt{\frac{a_1}{M_1} + \frac{1-a_1}{M_2}} T_e \quad (3.7)$$

For the accurate measurement of T_e , the probe tip was allowed to a sufficient positive bias voltage inside the plasma to cleanse the collecting surface. Then the probe tip surface was exposure to a sufficient amount of the electron current and impurities deposited on the tip were baked out. Burst wave having a few micro-second pulses with the repetition rate of 1 kHz was launched by a 5-cm diameter stainless steel grid (figure. 3.21). The amplitude of pulse was about + 8 V from the floating potential and it may not cause a significant perturbation to the bulk plasma density. The wave was monitored by a negatively biased (-45 V) ϕ 0.3-mm, 15-mm-long tungsten probe. The small perturbation (less than 0.1 %) of ion density could be obtained from the voltage difference taken in between both ends of the sensing resistor 500 k Ω . The signal was averaged over 3000 times to reduce the white noise sufficiently. The distance between receiver and launcher was varied from 4 cm (outside the presheath) to 8 cm at increments of 0.5 cm and ion current profile is shown in figure. 3.22-(a). The ion acoustic wave velocity (i.e. the common system sound velocity, c_s) is directly measured from the slope of distance from the launcher vs. the arrival time of the peak signal as shown in figure. 3.22-(b). The c_s measured by the ion acoustic wave measurement was compared to the Bohm velocity calculated from T_e measured by Langmuir probe in a single-ion-species plasma. Then it has been confirmed that the each results agree well before carrying the calculation of Eq. (3.7).

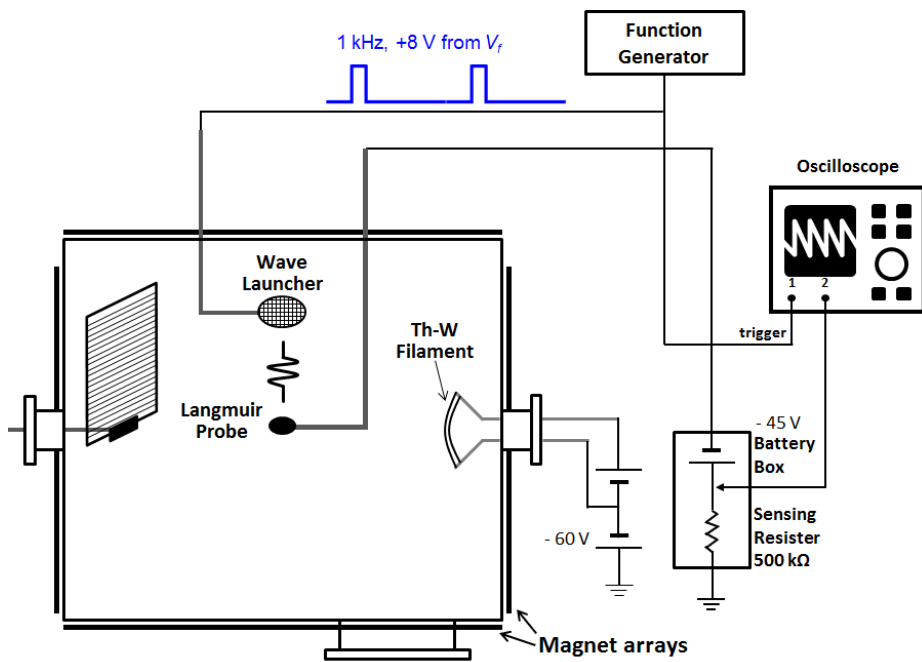


Figure 3.21. A schematic diagram of the multi-dipole plasma source and the ion acoustic wave measurement system. The plasma is generated by the energetic primary electrons, emitted from negatively biased hot filaments. The ion acoustic wave launcher and receiver are installed inside the uniform bulk plasma.

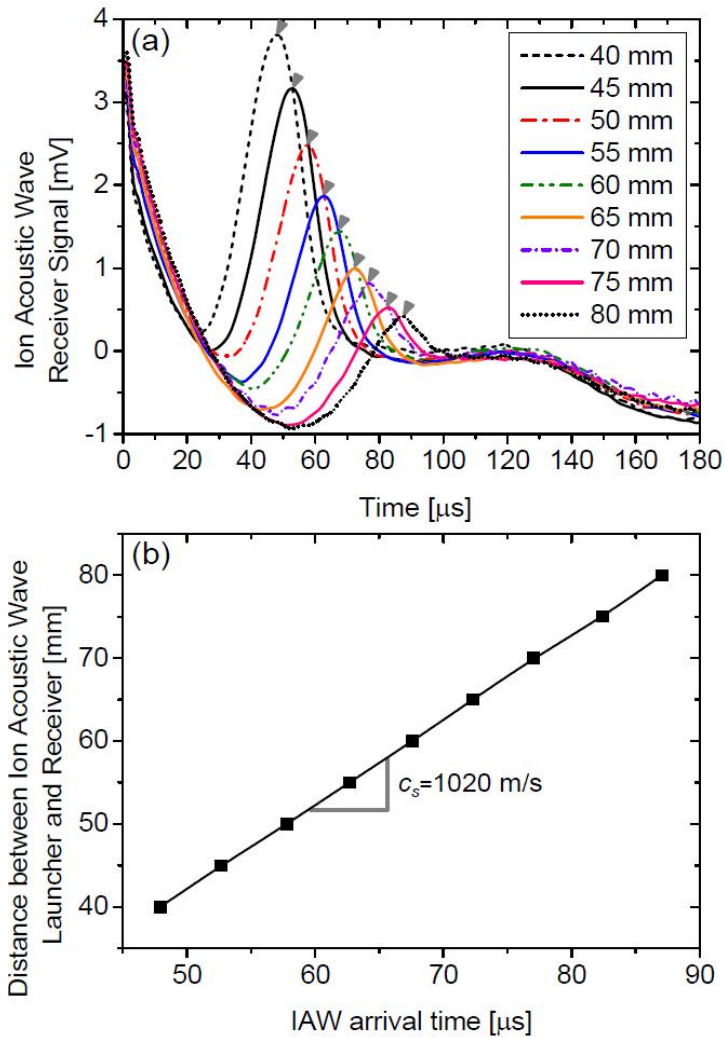


Figure 3.22. Ion acoustic wave measurement. (a) The signal of the ion acoustic wave received at various positions near the wave launcher and (b) the arrival time of the ion acoustic wave vs. the position of the receiver from the wave launcher. Data were obtained from the Ar/Xe (= 50/50) mixture gas discharged plasma. The arrival time of the ion acoustic wave was determined by the arrival time of the peak signal. The common system sound velocity is obtained from the slope of the graph.

Chapter 4. Characteristics of ion dynamics in presheath of collisional plasmas

4.1. Characteristic of ion dynamics in ion-neutral collisional presheath

Although it has been found that the presheath potential varies about $1 T_e$ within a single ion-neutral collisional mean-free-path, it has not been observed yet whether the ion enters the sheath edge with the Bohm velocity or not [73]. The analysis of the sheath structure relying only on the potential structure is quite useful to study the sheath physics but the lack of the observation of ion dynamic characteristics in the structure make it hard to achieve a comprehensive understanding on the sheath phenomenon. Because the original Bohm criterion is defined as the position where the ion velocity becomes the Bohm velocity, without observing the spatial distribution of the ion velocity the analysis might lack a completeness.

An example showing a comprehensive sheath characteristic, which is formed under the existence of ion-neutral collision, is shown in the figure 4.1. The spatial profiles of ion velocity measured by using the LIF method and the space potential measured by using the EP are shown in the figure. Data were obtained in a pure argon plasma. n_e , T_e , and p_{Ar} were $5.8 \times 10^9 \text{ cm}^{-3}$, 1.43 eV, and 0.57 mTorr, respectively. The target bias voltage was set to be -150 V and it formed the sheath structure in front of the target. At the given condition, the theoretical Bohm velocity of Ar^+ was 1850 m/s. In the figure, hollow-squares represents the ion velocity in front of the target (right axis) and the hollow-triangle represents the space potential distribution. In the figure it is observed that the ions reach the Bohm velocity at

approximately 7.5 mm in front of the target. It can be assumed that the position where the ion velocity becomes the Bohm velocity is the sheath entrance position. It is postulated in the Bohm's theoretical model that the potential difference of $DF = 0.5T_e$ in presheath is enough to accelerate the ions to reach the Bohm velocity. But the observation reveals quite different result. The plasma potential, V_p , is formed at about 1.2 V. At the position where the potential difference is $DF = 0.5T_e \sim 0.7$ V, the ion velocity reaches only $\sim 0.5C_s$. Additional potential difference of $1.4T_e \sim 2$ V is needed to accelerate ions to reach the Bohm velocity. Therefore, the total potential difference of approximately $1.9T_e$ is observed to be needed to accelerated ions to reach the Bohm velocity. It is quite larger than the original Bohm's model which assumes the collision-less condition, thus the sum of total kinetic and potential energy of a species is conserved.

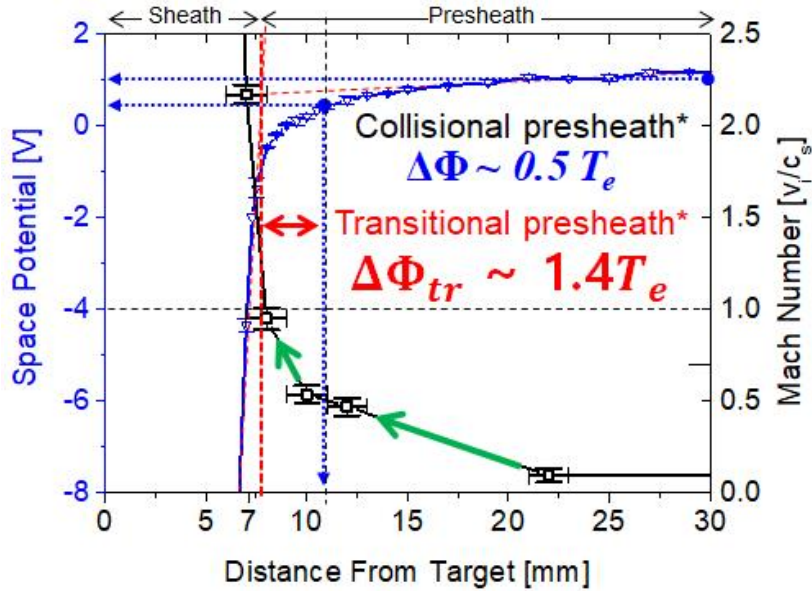


Figure 4.1. Spatial profile of the ion drift velocity and space potential obtained in a pure argon plasma.

The extra demand on the potential difference might be a result of the collisional effect between ion and neutral particles. Because the elastic collision between ion and neutral scatters directional kinetic energy of ions obtained from the potential difference in presheath toward a perpendicular direction of the surface normal direction, more potential energy is required to accelerate ions to reach the Bohm velocity in the presheath. The charge-exchange collisions, by which new ions at rest (or at thermal distribution of neutral gas species) are generated, also act as an energy loss source in the presheath. Therefore, it is quite reasonable that the potential difference should be larger than $0.5 T_e$.

The demand of extra potential difference to accelerate ions to the Bohm velocity in the presence of ion-neutral collision can be qualitatively estimated from Eq. (1.40) as

$$\frac{d}{dx} \left(\frac{T_i}{T_e} DF_{pr} \right) + \frac{E_k}{en_i} \frac{dR_{i,x}}{dx} = 0 \quad (4.1)$$

in which the existence of magnetic fields and the spatial variation of ion temperature was neglected. For the plasma condition of $T_e \gg T_i$, the left-hand side of Eq. (4.1) can be reduced to DF_{pr} . The first term on the left-hand side in Eq. (4.1) is the energy requirement to accelerate ions to the Bohm velocity and the integral over the distance of the total presheath region is comparable to the kinetic energy of ions at Bohm velocity, that is $0.5T_e$. The second term in the integrand in Eq. (4.1) is the energy loss due to the ion-neutral collision over the presheath region. The collisional friction terms, $R_{i,x}$, can be described by $R_{i,x} = m_i n_i (n_g s V_i) V_i$ and the Eq. (4.1) is reduced to

$$DF_{pr} + \frac{T_e}{2} \frac{m_i n_i (n_g s V_i) V_i}{n_i e} \frac{d}{dx} = \frac{T_e}{2} + a T_e. \quad (4.2)$$

Here, the length of the presheath is proportional to ion-neutral collisional mean-free-path, $l_{i-n} \sim 1/n_g s$, and the Bohm velocity was inserted to V_i as a characteristic velocity. Result shows that the potential difference in presheath should be larger than $0.5T_e$ in order to compensate the energy loss due to the ion-neutral collisions.

More rigorous calculation can be carried out by using fluid equations as follows.

$$V_i \frac{\partial n_i}{\partial x} + n_i \frac{\partial V_i}{\partial x} = 0 \quad (4.3)$$

$$m_i n_i V_i \frac{\partial V_i}{\partial X} + e n_i \frac{\partial \Phi}{\partial X} + k_B T_i \frac{\partial n_i}{\partial X} = -m_i n_i v_c V_i \quad (4.4)$$

Eq. (4.3) is the continuity equation without source or sink term. Eq. (4.4) is the momentum equation assuming constant collision frequency for ion-neutral collisions. By using dimensionless variables,

$$v_x = \frac{V_x}{V_{Ti}}, \quad t = \frac{T_e}{T_i}, \quad c_s = \frac{C_s}{V_{Ti}}, \quad \eta = \frac{X}{\lambda_{i-n}}, \quad \lambda_{i-n} = \frac{V_{Ti}}{v_c} \quad \text{and} \quad \phi = -\frac{e\Phi}{k_B T_e} \quad (4.5)$$

Eq. (4.4) can be simplified into

$$\left(v_x - \frac{c_s^2}{v_x} \right) \frac{\partial v_x}{\partial \eta} = -v_x, \quad (4.6)$$

and the potential distribution can be obtained from the Boltzmann relation and Eq. (4.3) as

$$\frac{\partial \phi}{\partial \eta} = \frac{1}{v_x} \frac{\partial v_x}{\partial \eta}. \quad (4.7)$$

Here, the Bohm velocity is defined as $C_s^2 = k_B (T_e + T_i) / m_i$ and the ion-neutral mean-free-path is defined as $\lambda_{i-n} = V_{Ti} / v_{i-n}$. In the integration of Eq. (4.7), the range of integration should be identified. Integration of Eq. (4.7) over distance yields

$$\Delta\Phi_{pr} \sim \frac{T_e}{2} \ln \left(1 + \frac{T_e}{T_i} \right). \quad (4.8)$$

Here, the integration range is forced to be $V_i \hat{=} [V_{Ti}, C_s]$. The result is shown in figure 4.2. The figure shows the variation of ion kinetic energy with respect to the potential difference in the presheath region. As the potential difference increases, the kinetic energy increases but not

conserving the total energy conservation. For ions reaching the Bohm velocity, the potential energy demand is found to be $1.96 T_e$.

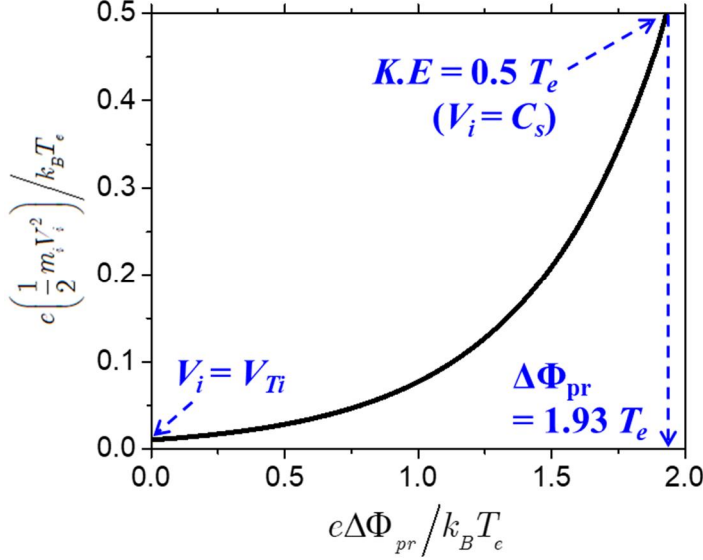


Figure 4.2. Normalized potential versus kinetic energy of ions in presheath.

Eq. (4.6), on the other hand, shows an interesting point on the characteristic of the potential difference in the ion-neutral collisional presheath, which is that the spatial variation of the ion velocity, is uniquely defined as a function of normalized length variable, $h = x/l_{i-n}$. Therefore, the potential distribution is also uniquely defined as a function of velocity following Eq. (4.7). i.e. the potential difference of the presheath region is determined regardless of the collisionality between ion and neutral particles. This seems contradict to our previous postulation that the energy requirement to accelerate ions to the Bohm velocity is larger than $0.5 T_e$ because of the kinetic energy loss of ions by ion-neutral collision while the ions traversing the presheath region. But the truth is quite simple. As the

collision between ion and neutral species becomes sparse, the collision frequency becomes small while the presheath size whose characteristic length is the ion-neutral mean-free-path becomes large, thus the total collisional energy loss becomes constant for all pressure conditions.

For a plasma source which has a finite size, however, the collisional mean-free-path can be much longer than the chamber size at a low-pressure condition. At the circumstance, the collisional energy loss within the chamber would be smaller than the above calculation result. Therefore, it can be postulated that if the chamber size is smaller than at least one ion-neutral collisional mean-free-path, the potential energy drop in the presheath would be smaller. This effect can be called the finite boundary effect regarding ion-neutral mean-free-path. At the experimental condition of 0.5 mTorr, the effect of the ion neutral collision is revealed as the potential drop of $2 T_e$ in the presheath region.

4.2. Characteristic of ion dynamics in ion-ion collisional presheath under existence of ion-neutral collision

To investigate the collisional effect on the instability, the total pressure of argon and xenon mixture gas was controlled in the range of 0.5 ~ 2 mTorr by mass flow controllers. In figure 2.4, four chosen pressure conditions (crosses) are marked with theoretical pressure threshold (solid line) of the two-stream-instability which is calculated by Eq. (2.3), considering ion-neutral collisions. Because T_e was different for all our experimental conditions, the threshold is obtained as a function of T_e , while the ion temperature is approximately fixed as 0.038 eV, which was measured by using a tunable diode laser induced fluorescence in the same device. Among the four pressure conditions, plasmas at 0.52, 0.73, and 1.04 mTorr conditions lie in the unstable region and the plasma condition at 2.1 mTorr lies in the stable region. For the experiment, the discharge current from filaments was controlled in the range of 50 ~ 130 mA, in order to ensure that the electron density, n_e , would be maintained close to $6 \times 10^9 \text{ cm}^{-3}$ for all pressure conditions. However, the electron temperature, T_e , decreased in the range of 0.5 ~ 1 eV as the total pressure increased. The density ratio of argon ions and xenon ions, $n(\text{Ar}^+)/n(\text{Xe}^+)$ was set to be near unity in all pressure conditions, at which the growth rate of the instability would be maximum [8-9]. The details for controlling the ion density ratio in a two-ion-species mixture plasma can be found in reference [19]. The experimental conditions and plasma parameters are summarized in table 4.1.

Table 4.1. Plasma parameters

No.	p_{tot}	p_{Ar}	p_{Xe}	n_e	n_{Ar^+}/n_{Xe^+}	T_e
	[mTorr]	[mTorr]	[mTorr]	[cm^{-3}]	[%/%]	[eV]
1	0.52	0.37	0.15	6.0×10^9	50/50	1.04
2	0.73	0.57	0.16	5.8×10^9	50/50	1.04
3	1.04	0.73	0.31	6.6×10^9	58/42	0.98

4 2.10 1.46 0.54 5.6×10^9 50/50 0.54

Figure 4.3(a) shows the spatial profiles of the drift velocity of the Ar^+ and Xe^+ , and the space potential in front of the negatively biased target when the total pressure is 0.52 mTorr ($p_{\text{Ar}} = 0.37$ mTorr and $p_{\text{Xe}} = 0.15$ mTorr). n_e and T_e are $6.0 \times 10^9 \text{ cm}^{-3}$ and 1.05 eV, respectively. In the figure, it is observed that for Ar^+ , the measured drift velocity at the sheath edge, 1440 m/s, is much slower than its theoretical Bohm velocity, $C_{\text{Ar}} = 1580$ m/s. However, for Xe^+ , the measured drift velocity is 1060 m/s, which is much faster than its theoretical Bohm velocity, $C_{\text{Xe}} = 880$ m/s. Rather, the measured velocities are similar with the modified Bohm velocities given by Eq. (2), which are 1350 m/s for Ar^+ and 1100 m/s for Xe^+ . This result is consistent with previous researches [11,12] showing that two-stream-instability occurred near the sheath edge of two-ion-mixture plasmas.

Whether the instability occurred in the given condition or not is identified by observing a ‘locking’ of relative ion drift velocity. Once the onset condition of the two-stream-instability on relative ion velocity ($\Delta V \geq \Delta V_c$) is reached, the strong momentum transfer between the ion species induces the relative velocity to become constant [8]. As shown in figure 4.3(b), the relative velocity between Ar^+ and Xe^+ initially increases as the ions are accelerated inside the presheath toward the sheath. Because of mass difference, Ar^+ gains more speed than Xe^+ while traversing the presheath. After the relative velocity reaches nearly 300 m/s at 14 mm in front of the target, it remains constant from 14 mm to 9 mm where the sheath edge locates. If the motion of each ion is governed only by the potential difference, the relative velocity should have increased continuously because the potential decreased continuously within the region. Besides, the experimentally observed critical velocity for the onset of the instability, 300 m/s, is consistent to the theoretically estimated [8] critical velocity for our experimental condition, $\Delta V_c = 325$ m/s, within the experimental error. Because of these features, the constant-relative-velocity region is hereafter

termed the ‘instability region’.

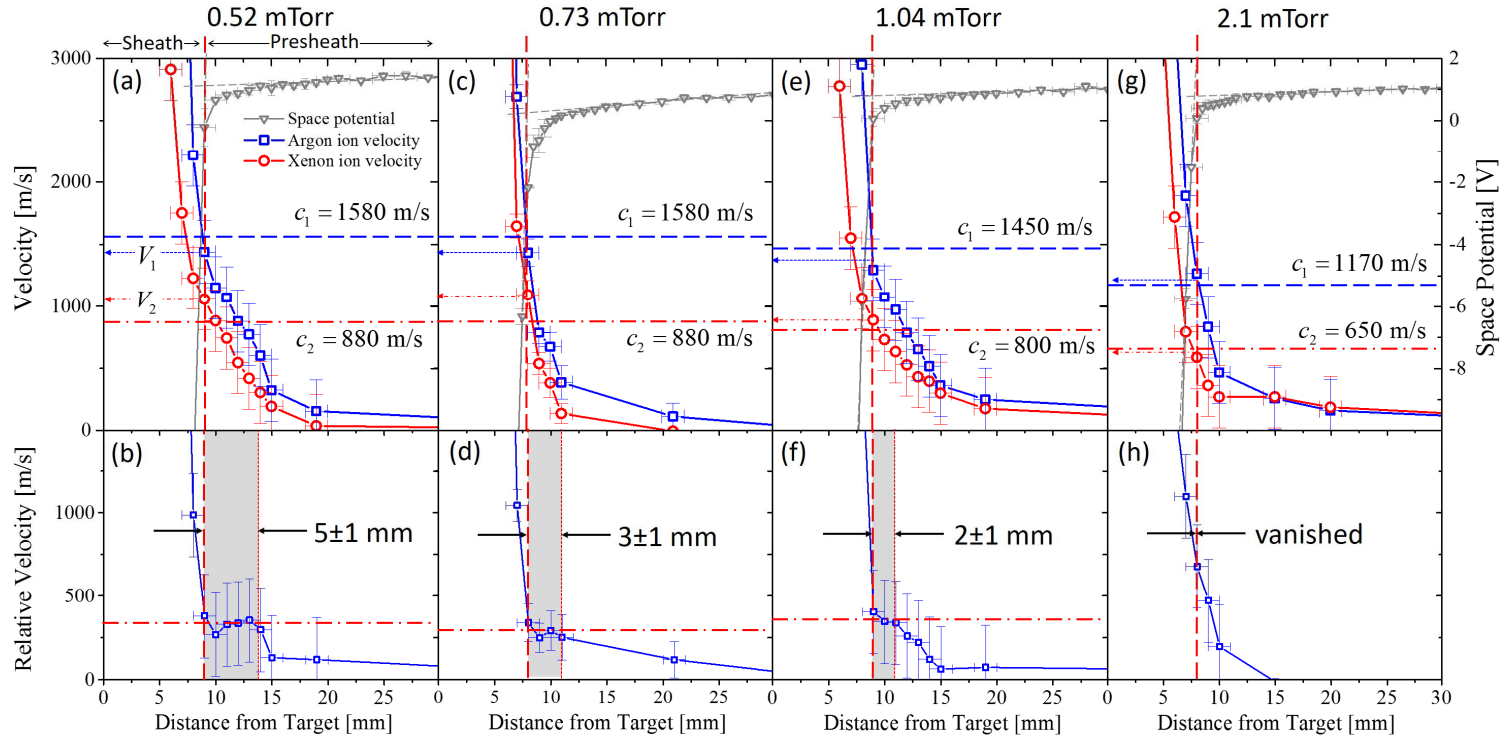


Figure 4.3. Spatial distribution of argon and xenon ions' velocity and their relative velocity for pressure conditions of ((a) and (b)) 0.52 mTorr, ((c) and (d)) 0.73 mTorr, ((e) and (f)) 1.04 mTorr, and ((g) and (h)) 2.1 mTorr.

To investigate the ion-neutral collision effect on the instability, the above two features (*i.e.* ion drift velocities at the sheath edge and the locking of the relative velocity) are observed with increasing total pressure. The data in figures 4.3(b), (d), (f) and (h) show the spatial variation of the ion velocities and the relative velocities obtained at 0.73, 1.04, and 2.1 mTorr conditions. In figures 4.3(c) and (e), the speed of Ar^+ at the sheath edge is slower than its own Bohm velocity. At the same time, the speed of Xe^+ at the sheath edge is faster than its own Bohm velocity. In figures 4.3(d) and (f), the constant-relative-velocity region is also observed near the sheath edge. At the 2.1 mTorr condition, however, it is observed that the ions exit the plasma boundary at almost their individual own Bohm velocity (figure 4.3(g)), and the relative velocity increases continuously without leaving the constant-relative-velocity region (figure 4.3(h)). This means that the two-stream-instability does not occur above the 2.1 mTorr condition.

Figure 4.4 summarizes the measured ion drift velocities at the sheath edge. Velocities are normalized by each ion's own Bohm velocity as

$$M_i = \frac{V_{SE,i}}{C_{s,i}}. \quad (4.9)$$

Drift velocities of Ar^+ are plotted as unfilled squares and the velocities of Xe^+ are plotted as unfilled circles. It is apparent that, under the conditions of 0.5 ~ 1 mTorr, the drift velocity of Ar^+ is slower than its own Bohm velocity and the drift velocity of Xe^+ is faster than its own Bohm velocity. For the condition of 2.1 mTorr, however, the ions exit the plasma boundary with their individual own Bohm velocity. This corresponds to our initial assumption that the ion-neutral collisions would limit the activation of the two-stream-instability, and therefore the ion velocity at the sheath edge becomes their individual Bohm velocity, even when the density ratio of two ion species is unity.

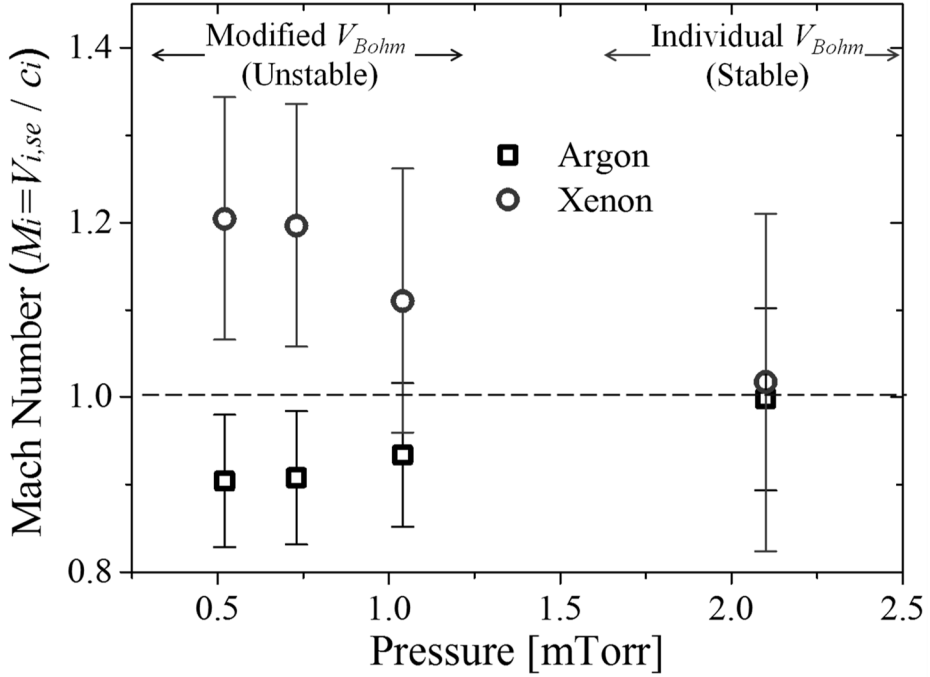


Figure 4.4. Drift velocities of argon and xenon ions normalized by individual own Bohm velocity.

Interestingly, the length of the instability region decreases as the pressure increases, as shown in figures 4.3-(b), (d), and (f). The measured length of the instability region is summarized in figure 6, as unfilled squares. As the pressure increases from 0.52 mTorr to 1.04 mTorr, the length of the instability region decreases from 5 ± 1 mm to 2 ± 1 mm and it finally vanishes at 2.1 mTorr. In the figure 4.5, the characteristic wavelength of the instability, λ_{inst} , which is calculated as $\lambda_{inst} = 2\pi/k$ is plotted together as a solid line. Here, k is the wavenumber of the instability at the maximum

growth rate, γ_{\max} . The characteristic wavelength of the instability when the ion-neutral collision is not considered in ($\nu_{i-n} = 0$), is also drawn as a dashed line. It is worth noting that the data follows the solid line rather than with the dashed one, especially at the pressures below 1 mTorr. This means that the ion-neutral collisions play an important role in determining the characteristic wavelength of the instability in real plasmas even when the ion-neutral collisions are very rare.

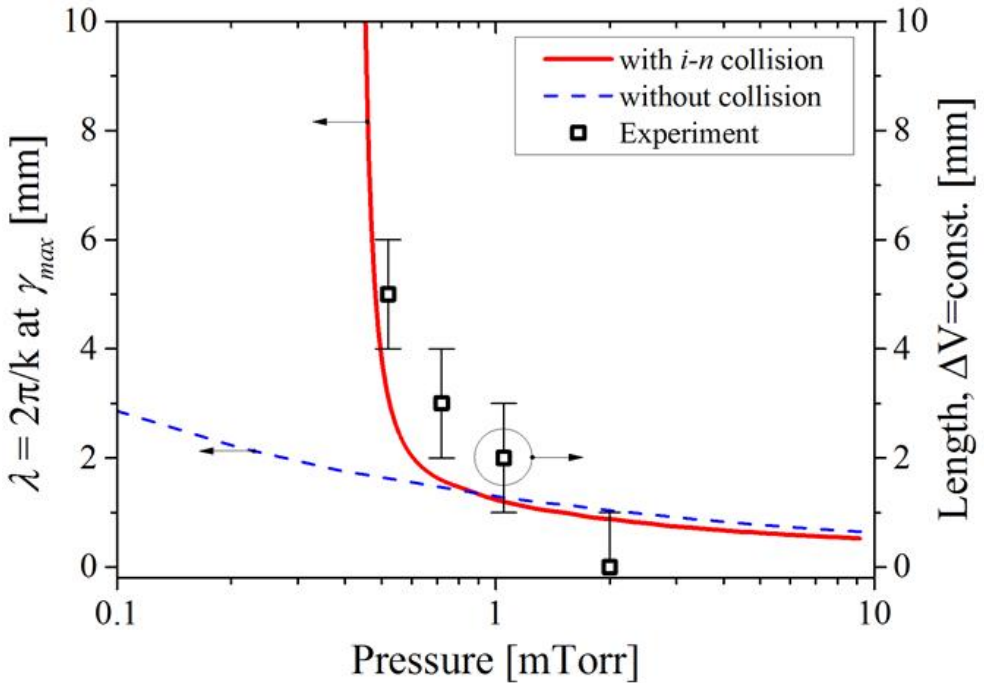


Figure 4.5. Characteristic wavelength of the instability with (solid-red-line) and without (dotted-blue-line) the consideration of the ion-neutral collisions. Unfilled (-black) squares represent the experimental length of the instability region.

4.3. Characteristic of electric potential in collisional presheath

In this section, the characteristic of the electric potential in the collisional presheath will be briefly discussed. The characteristic of the electric potential in an ion-neutral collisional presheath has been analyzed in section 4.1. The presheath potential under the ion-neutral collision is found to be few T_e , which corresponds to the summation of the directional ion kinetic energy toward the target at the sheath edge ($0.5T_e$) and the energy requirement to compensation the energy loss due to the ion-neutral collisions ($\sim T_e$). It is found that the total potential difference in the presheath is also dependent on the size of the chamber compared to the presheath size which is comparable to the ion-neutral collisional mean-free-path. For our chamber geometry, the potential difference of the ion-neutral collisional presheath was approximately $2T_e$.

For all pressure conditions in figure 4.3, it is observed that the potential difference of the presheath region is approximately $2T_e$, which is a similar result with the observation in ion-neutral collisional presheaths. Whether the two-stream-instability occurs or not, seems not to affect the presheath potential structure. It is because the momentum and energy transfer triggered by the two-stream-instability between two-ion-species is an energy conserving mechanism as

$$\mathbf{R}^{a-b} = -\mathbf{R}^{b-a} \quad (4.10)$$

and

$$\int d^3v \frac{1}{2} m_a v^2 C(f_a, f_b) + \int d^3v \frac{1}{2} m_b v^2 C(f_b, f_a) = 0. \quad (4.11)$$

Thus, the total energy requirement for the acceleration of ions until the ions reach the sheath edge, which corresponds to the total potential drop in the presheath region, does not changed from the ion-neutral collision conditions.

4.4. Summary

In this chapter, we investigated the pressure condition in terms of whether or not the ion-ion two stream instability was activated by observing the spatial variation of the ions' motion near the sheath-presheath boundary. The pressure is used as an index of ion-neutral collisions. When the instability occurs, it triggers a brisk momentum transfer between two ion species so that the relative ion drift velocity remains constant and the modified Bohm velocities of the ions are at the sheath edge, as originally suggested by Baalrud [13-15]. However, the ion-neutral collisions suppress the occurrence of instability. This is because the ion-neutral collisions disturb the direct field interaction between different ion species. From the dispersion relation considering the ion-neutral collisions, we found that some pressure conditions exist where the instability cannot occur, even though the other conditions are required to activate the instability, such as the ion density ratio or the critical relative velocity. Experimentally, two distinguishing features on the spatial distribution of the ion velocity were used as an indicator to observe whether the instability occurs near the sheath-presheath boundary. One of these features is the existence of the constant-relative-velocity region and the other is the ions' drift velocity at the sheath edge. Experimental results clearly demonstrate that the instability cannot be activated when the pressure is higher than the theoretically estimated pressure threshold (Eq. (2.4) in Section 2.1.2). In addition, it is demonstrated that, at the condition where the instability cannot increase, the ions exit the plasma boundary with their individual Bohm velocities, even in a two-ion mixture condition. From the observation of the presheath potential difference, it has been found that the ion-neutral collision governs the electrical property of the ion-ion collisional presheath regardless of whether the two-stream-instability occurs or not because of the conservative interaction between two-ion-species.

Chapter 5. Characteristics of ion dynamics in presheath of magnetized plasmas

In this chapter, characteristics of the ion motion in the magnetic plasma presheath and the characteristics of the potential difference in the region will be analyzed. First, a fluid model introduced in the section 2.2 will be verified by comparing the ion incident angle at the wall with the model estimation. For the experiments, plasma condition was chosen to have $\lambda_c \sim \lambda_m \gg \lambda_d$ (i.e., weakly-collisional and weakly-magnetized condition) so that effects of electric and magnetic fields on ion motion would dominate over collisional effects. Experiments were carried out in an electron cyclotron resonance (ECR) hydrogen plasma device that had few hundreds gauss of static magnetic field. After the verification, the characteristics of the ion motion and will be analyzed in various plasma conditions by using the fluid model.

5.1. Validation of theoretical magnetic sheath model

Figure 5.1 shows ion incident angle on a surface with respect to the geometrical magnetic field angle between the magnetic field line and the surface normal direction. Experimental data were taken from the inclined angle of the nano-tips (red-square dots), described in Section 3.4. As shown in the figure, the ion incident angle on a surface was much smaller than the geometrical magnetic field angle. At a magnetic field angle of 60° , the ion incident angle on a surface becomes $8.5 \pm 1.5^\circ$, meaning that the ion trajectory is quite vertical to the wall surface. The larger the angle between the magnetic field and the surface normal direction, the larger the incidence angle of ions at the time of impact. When the magnetic field angle was

increased to 85° (grazing to the surface with a tilt angle of 5°), the ion incident angle on a surface became about 17°.

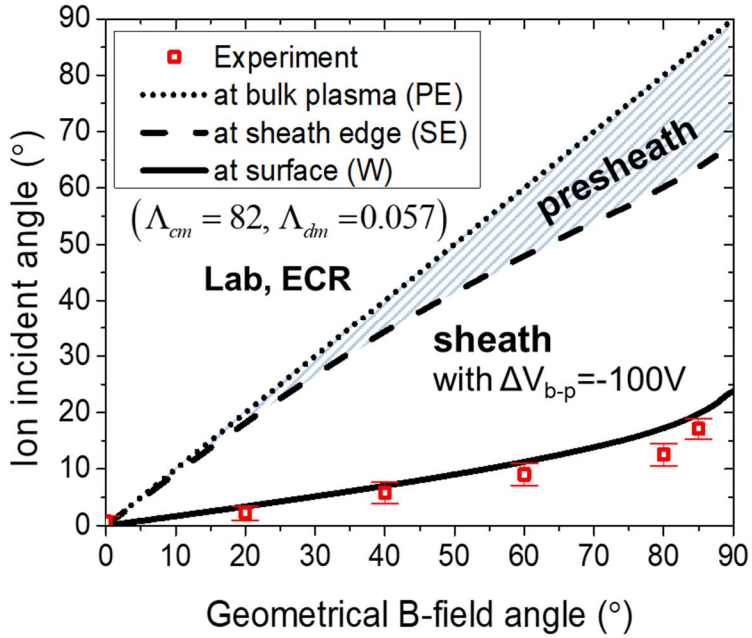


Figure 5.1. Ion incident angle on a target surface with respect to the geometrical oblique magnetic field angle between the magnetic field line and the surface normal direction. Experimental data are taken from the inclined angle of nano-tips (dots). Model-estimated ion incident angle (dashed line) is calculated with corresponding plasma parameters used in the experiments.

The solid-black line in the figure 5.1 shows the ions incident angle at the plasma-facing wall surface, which was calculated based on the fluid model we described in the section 2.2. As shown in the figure, the experimental data fit well to the model estimation. Here, the incident angle was calculated with $\Lambda_{cm} = 82$ and $\Lambda_{dm} = 0.057$ which corresponds to the plasma condition of the experiment. This is the first experimental

verification of the Ahedo's [30] fluid model for the magnetic sheath and presheath. The fact that the model we introduced in the section 2.2 fits well with the experimental data reveals that the ion motion in the presheath has 3-dimensional property. The ions are accelerated toward the wall surface along the electric fields while they drift toward the $E \times B$ direction in the presheath region. The ion velocity in surface-normal direction becomes the Bohm velocity at the sheath edge and the Bohm criterion holds for only 1-dimensional direction regardless of the velocity component in other directions.

5.2. Characteristic of ion dynamics in magnetic presheath

By analyzing the fluid model ion motion in sheath and presheath regions can be distinguished. Figure 5.1 also shows how much ions are deviated from the magnetic field line while they start to traverse from the bulk plasma through presheath and sheath regions to the wall surface. The shaded region in the figure corresponds to the presheath region while the unshaded region corresponds to the sheath region in the domain of the magnetic field - ion incident angle space. The dashed line and the solid line represent the sheath-presheath boundary (or the sheath edge) and the wall surface, respectively. For instance, when the magnetic field angle is 60° , ions will enter the presheath with the incident angle same to the magnetic field angle. After ions pass through the presheath region, the ion incident angle at the sheath-presheath boundary becomes 45° with respect to surface normal direction. The ion trajectory becomes much shallower when ions traverse through the sheath region while the ion incident angle reaches approximately 8.5° at the wall surface. This is because the electric fields inside the presheath and the sheath deviating the trajectory of ions from the magnetic

field line. Electric fields can accelerate ions along the field line and result in the formation of $E \times B$ drift motion of ions.

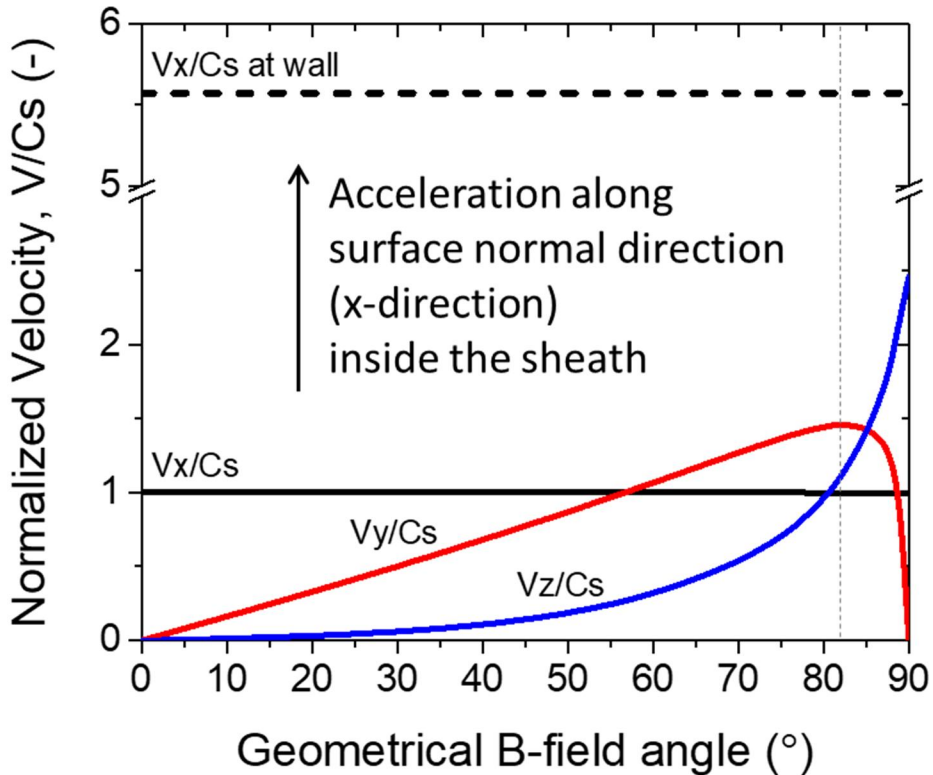


Figure 5.2. Variation of ion velocity at the sheath edge and the wall surface vs. geometrical magnetic field angle with respect to surface normal direction. Ions can only gain energy toward surface normal direction inside the sheath region (from the sheath edge to the wall surface).

Figure 5.2 depicts ion motion inside the presheath region with respect to the angle between the magnetic field and surface normal direction. Solid lines denote vector components of the ion drift velocity which is normalized

to Bohm velocity, $C_s = \sqrt{(k_B T_e + k_B T_i)/M_i}$, at the sheath-presheath boundary. One can confirm that the normalized velocity in x -direction is unity in the figure. This is analogous to the Bohm sheath criterion that the sheath-presheath boundary is defined as the position where the ion drift velocity in x -direction (i.e., the velocity component vertical to the surface) becomes the Bohm velocity.

It is the presheath electric field, E_{pre} , that accelerates the ion from the zero-drift velocity to the Bohm velocity. The electric field originates from a small difference in density between ions and electrons due to different thermal mobility between them, even though the quasi-neutrality is satisfied at the same time. The electric field only forms along the x -direction as shown in Figure 2.5(a) due to homogeneity in y - and z -directions in our coordinate system. Therefore, the presheath electric field can accelerate ions only in x -direction. This non-symmetric acceleration of the electric field is one reason that makes the trajectory of ions deviate from the magnetic field line.

The other effect of the electric field on ion trajectory inside the presheath is the $E \times B$ drift. In our coordinate system, the z -direction represents $E \times B$ direction because the presheath electric field, E_{pre} , forms along the x -direction while the magnetic field line lies on the x - y plane. As shown in the figure, ion drift velocities in z -direction, V_z , are not zero at the sheath edge. The velocity gradually increases as the magnetic field angle increases. This corresponds to the $E \times B$ drift phenomenon. When the electric field forms an angle to the magnetic field, the perpendicular vector component of the electric field to the magnetic field line makes the gyrating center of ions move along the $E \times B$ direction (z -direction in figure 2.5(a)) with $E \times B$ drift velocity, $\mathbf{V}_{E \times B} = \mathbf{E} \times \mathbf{B}/B^2$. Since the magnitude of the drift velocity is proportional to $\sin \psi$, the ion trajectory becomes more deviated

from the magnetic field line as the magnetic field forms a grazing angle with the surface.

On the other hand, the velocity in y -direction at the sheath edge shows a maximum at $\psi \sim 80^\circ$. Since the potential difference inside the whole presheath region, i.e., from bulk plasma to sheath-presheath boundary, is revealed to be constant for all magnetic field angles (not shown in this paper), the increase of the $E \times B$ drift velocity in z -direction causes y -directional velocity to decrease.

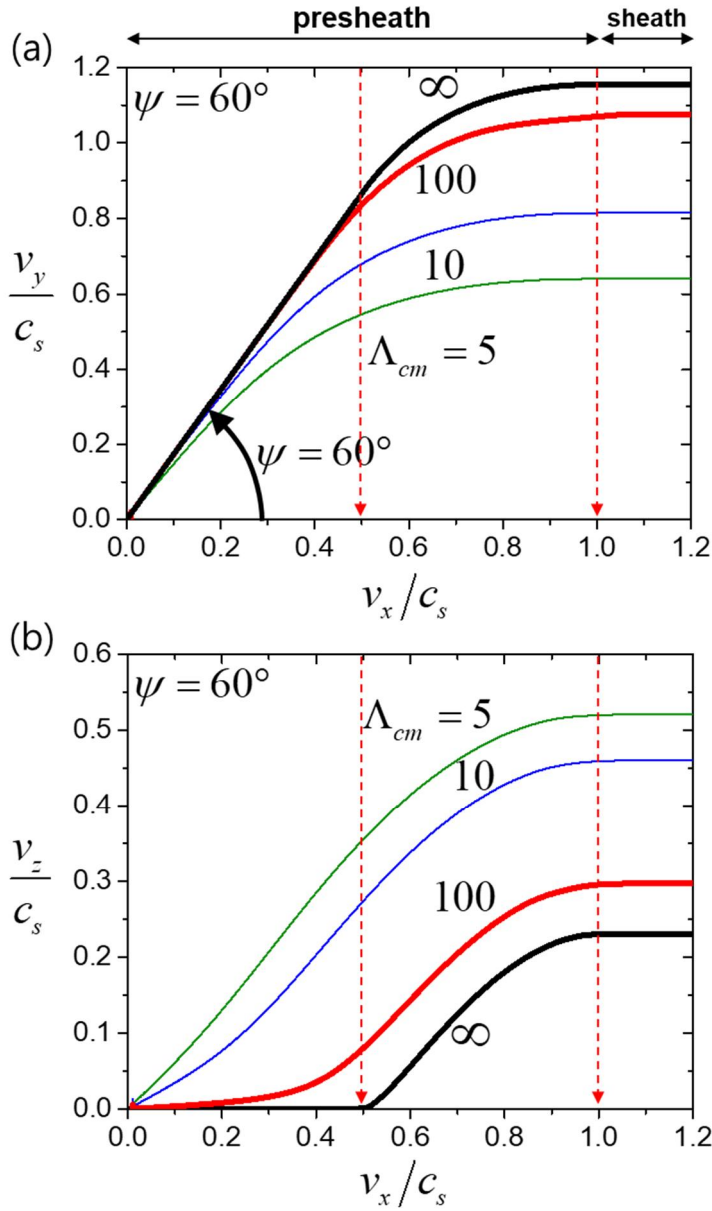


Figure 5.3. Ion velocity for $\psi = 60^\circ$ and $\Lambda_{cm} = 0.01, 0.1, 0.5, 1, 5, 10, 100$. The velocities are normalized over the Bohm's velocity, C_s . The sheath edge is where $V_x/C_s = 1$.

The variation of the ion velocity components for $\psi = 60^\circ$ and various Λ_{cm} are shown in figure 5.3. All the velocity components are normalized over the Bohm's velocity, C_s . The sheath edge is where $V_x/C_s = 1$. In the figure, $\Lambda_{cm} = \infty$ corresponds to the collision-less condition. As shown in the figure, it can be postulate that the presheath region can be divided into two distinctive regions under the collision-less condition. For $V_x/C_s < 0.5$, only the velocity component in y -direction increases until the ion speed becomes the Bohm velocity along the magnetic field line. As the velocity increases, $V_x/C_s > 0.5$, the velocity component in z -direction becomes increased until the ion velocity in x -direction reaches the Bohm velocity. This is analogous to the Chodura's [25-27] magnetic sheath model that divide the presheath into the plasma presheath and the magnetic presheath. However, Chodura's model is quite idealized since the collision-less condition cannot be achieve in practical plasmas. When the collisionality increases (decreasing Λ_{cm}), the separation between two distinctive region becomes ambiguous and the $E \times B$ drift velocity continuously increases from the beginning of the presheath due to the electric field in the presheath is increased (see section 4.1) when the ion-neutral collision becomes severe.

Figure 5.4 shows the effect of the ion-neutral collisions on the ion incident angle at the sheath edge and the wall surface with respect to the magnetic field angle, γ . In the calculation, parameters other than Λ_{cm} are assumed to be the same as our experimental conditions. As shown in Figure 5.4(a), the ion incident angle to the surface normal direction becomes small (more vertical to the surface) at the sheath edge with decreasing Λ_{cm} . Because the electric field in the sheath accelerates ions only toward the wall surface, the angle becomes much smaller at the wall surface (see Figure 5.4(b)). This is due to the following reason. In Eqs. (2.16) - (2.18), one can notice that as Λ_{cm} diminishes, the term regarding the $E \times B$ drift vanishes and the dragging effect (terms, $-V_{x,y,z}$) dominantly affects the spatial variation

of the ion motion. With increasing collisionality, ions can only drift along the electric field line that is parallel to the surface normal direction.

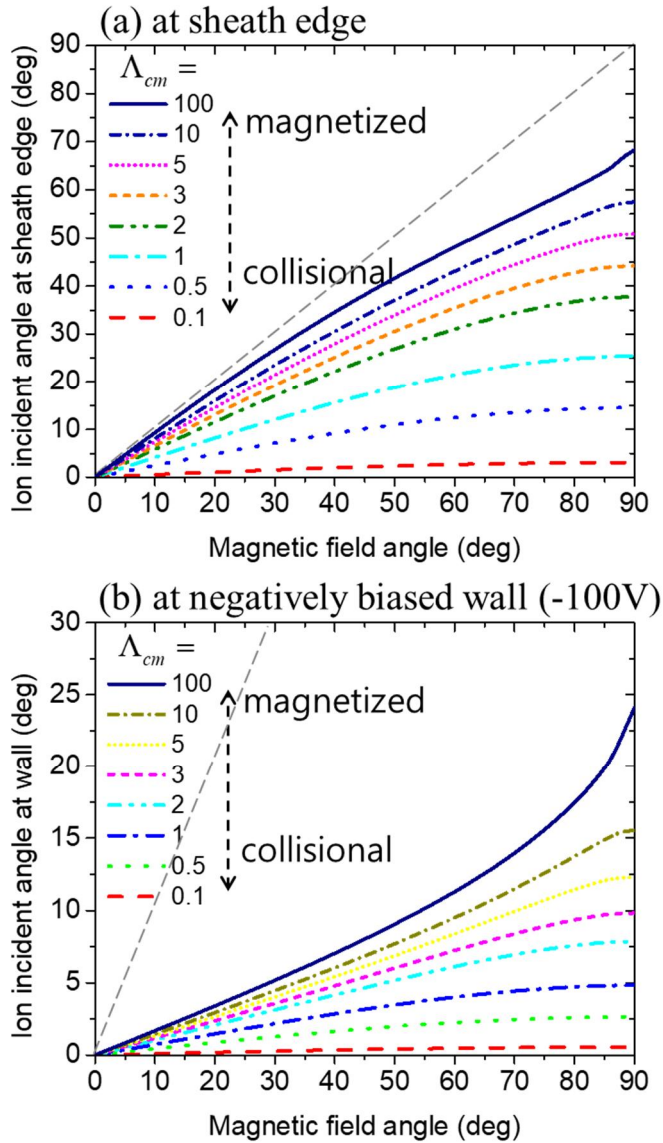


Figure 5.4. Variation of the ion incident angle vs. geometrical magnetic field angle with various Λ_{cm} (a) at the sheath edge and (b) at the negatively biased wall. As the collisionality increases (smaller Λ_{cm}), the ion incident angle decreases. (i.e., ions enter the surface following the surface normal direction).

5.3. Characteristics of electric potential of magnetic presheath

Figure 5.5 shows the variation of the potential difference and the length of the presheath region with respect to the ion-neutral collisionality, Λ_{cm} , for $y = 60^\circ$. In the calculation, experimental plasma parameters were assumed to be constant under the various pressure condition. Figure 5.5(a) reveals that the total potential drop in the whole presheath region is constant over the pressure variation. In the figure, each portion on the total potential drop is also depicted in the figure based on the following relation originated from Eq. (1.40).

$$e\Delta\Phi_{pr} \approx \int m_i V_{ix} \frac{dV_{ix}}{dx} + m_i v_c V_{ix} + eV_z B \sin\psi dx \quad (5.1)$$

Each portion of the ion-neutral collision and the $E \times B$ drift motion among the total potential difference in the presheath seems constant over the pressure variation. This fact is analogous to the fact that the total presheath length is approximately proportional to the ion-neutral mean free path as shown in figure 5.5(b). i.e., the ion-neutral collision determines the major characteristics of the magnetized presheath.

Figure 5.6 shows the variation of the potential difference and lengths of the presheath region with respect to the geometrical magnetic field angle for a constant pressure condition. As shown in the figure, it is found that as the magnetic field angle increases, the total presheath size becomes smaller. This is because the collisional portion of the presheath potential drop becomes smaller as the $E \times B$ effect becomes severe with the increase of the field angle. In order to maintain the constant total potential, the total length of the presheath size should be decreased with the increase of the magnetic field angle. As the effect of the $E \times B$ dominates, the shortened presheath length makes the collisional effect becomes much weaker and the $E \times B$ effect dominates much more.

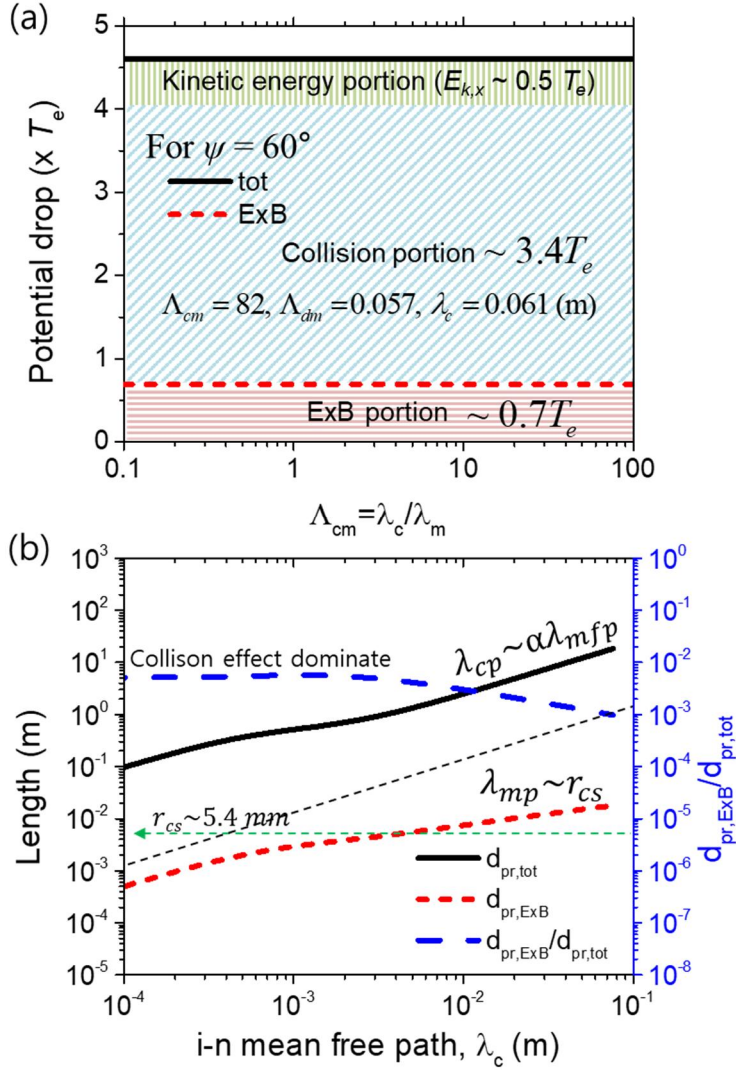


Figure 5.5. (a) potential drop in presheath for various Λ_{cm} . (b) total length of the presheath (black-solid line), length of the presheath where $E \times B$ motion dominates (red-short-dashed line), and the ratio between the two lengths (blue-dashed line) versus ion-neutral collisional mean-free-path

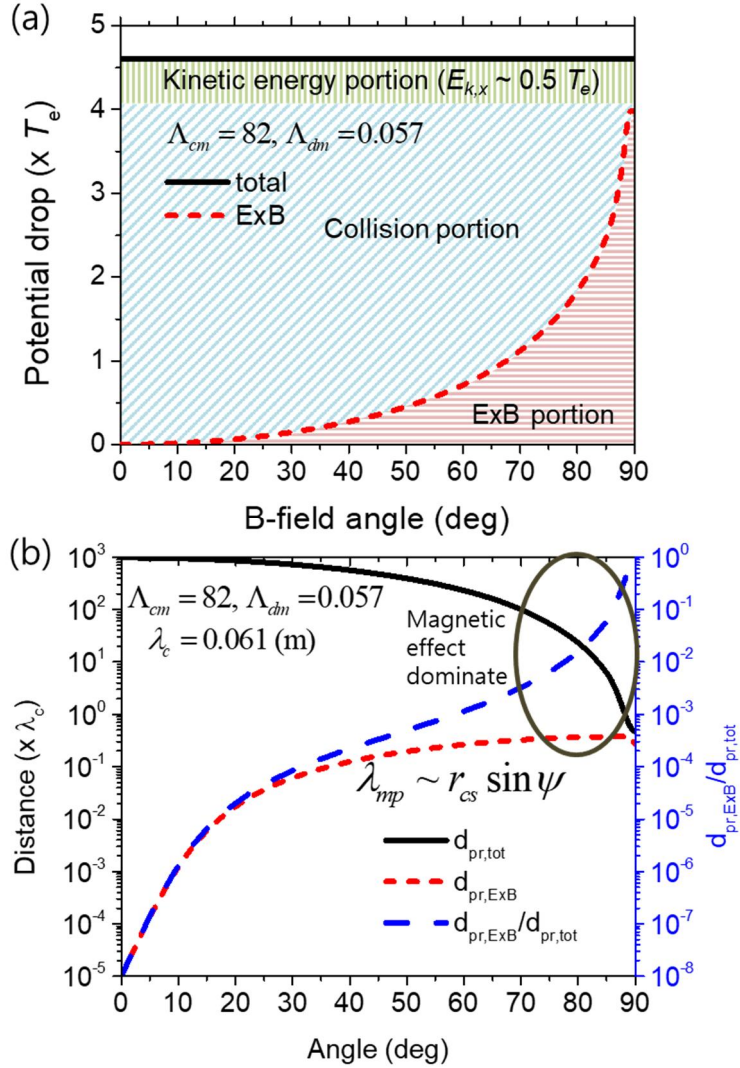


Figure 5.6. (a) Potential drop in presheath for various magnetic field angle, ψ . (b) Total length of the presheath (black-solid line), length of the presheath where $E \times B$ motion dominates (red-short-dashed line), and the ratio between the two lengths (blue-dashed line) versus magnetic field angle, ψ . Lengths are normalized over the ion-neutral mean free path.

5.5. Summary

The mechanism regarding how the ion incident angle on a wall surface can be changed from the geometrical angle between the magnetic field and the surface was investigated in this study. A fluid model for describing ion motion inside magnetized and weakly-collisional presheath and the Debye sheath was introduced. The model analysis on the ion incident angle at the wall surface was verified by comparing with the ion incident angle on an oblique target immersed in an electron-cyclotron-resonance plasma source. Both results showed good agreement.

From the model analysis, it can be concluded that the discrepancy between the ion incident angle on a surface and the magnetic field angle is due to 3-dimensional change of the ion motion which is affected by the electric field inside the presheath and the sheath. The electric field inside the magnetized presheath caused both $E \times B$ drift motion and acceleration toward the surface. The electric field was found to be inversely proportional to the ion-neutral collisional mean-free-path, which reveals that the overall characteristic of the magnetized presheath was determined by the collisional property of the plasma. Unlike the Chodura's postulation, the magnetized presheath is found to consist of a unified single geometry, in which the $E \times B$ drift motion occurred together.

Our results regarding the collisionality provided insights into ion dynamics inside the magnetized and weakly-collisional presheath. As collisionality increased severely, the magnetized character of the plasma presheath, i.e., the $E \times B$ drift motion, weakened due to the dragging effect on ion motion. The ion motion became 1-dimensional with vertical direction to the plasma-facing surface. These results provide important information to improve interpretation of the plasma-surface interaction phenomena in a

thermonuclear fusion device wall while providing valid boundary conditions for plasma simulations

Chapter 6. Characteristics of ion dynamics in presheath of RF plasmas

6.1. Variation of IVDF under DC presheath electric field

Before we investigate the effect of radio-frequency (rf) wave launched by a rf-biased electrode on the ion dynamics in the presheath, we first observed the characteristics of the spatial variation of ion velocity distribution (ivdf) in the presheath region in front of DC-biased target.

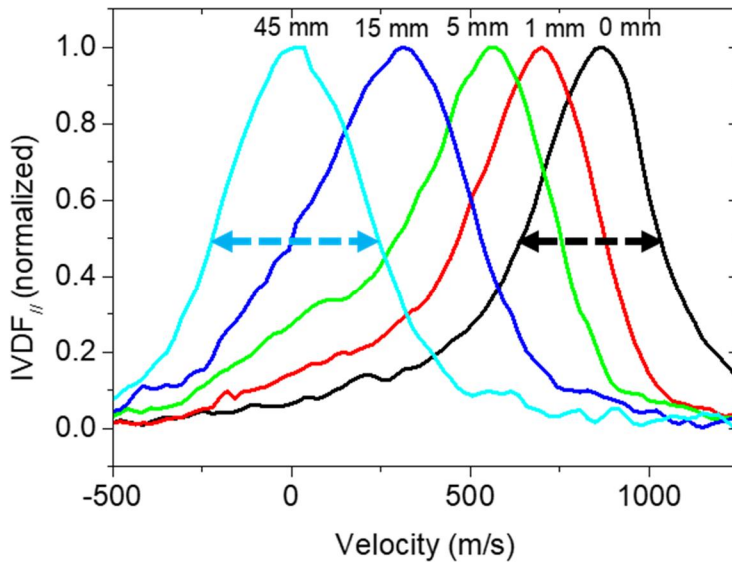


Figure 6.1. Ion velocity distribution in front of DC biased target immersed in xenon plasma. $p = 0.18$ mTorr, $n_e \sim 3 \times 10^9$ cm⁻³, $T_e \sim 1.1$ eV, $C_{s,Xe} \sim 900$ m/s, $V_{bias,DC} = -100$ V, $V_p \sim 3$ V

Figure 6.1. shows 1-dimensional xenon ion velocity distributions (v_z) at different positions in front of a target biased at $V_b = -100$ V . A multi-dipole source operated at a xenon neutral pressure of $p = 0.18$ mTorr was utilized in the experiment. The electron density, n_e , was 3×10^9 cm⁻³, the electron temperature, T_e , was 1.1 eV, and the plasma potential, V_p , was 3 V. The Bohm velocity at the given plasma condition was $C_{s,Xe} \sim 900$ m/s. The position, depicted in the figure, represents a distance from the sheath edge. The sheath edge was identified as a position where the ion fluid velocity becomes the Bohm velocity. In the figure, it can be observed that the 1-dimensional ion velocity distribution varies over the whole region of the presheath.

The detailed characteristics of the spatial variation of the ion velocity distribution are shown in figure 6.2. Figure 6.2-(a). shows the spatial variation of the ion fluid velocity. The fluid velocity at 60 mm away from the sheath edge was nearly zero. As the ions are accelerated by the presheath electric field the ion drift velocity increases, and the ion velocity finally reaches the Bohm velocity. Figure 6.2-(b) shows the variation of the longitudinal (axial direction) full width at half maximum (FWHM_{||}) in the presheath region. At the beginning of the ion acceleration (far away from the sheath edge) the FWHM_{||} increases slightly, meaning that the increase of ion temperature. However, as the ion fluid velocity increases further, the FWHM_{||} decreases and reaches a minimum at the sheath edge.

The increasing of the FWHM_{||} is due to the collision between ion and neutral particles at low ion velocity regime [Birdsall***]. When the ion velocity is low the ion induces a polarization of neutral species and thus directional energy can be converted into the thermal energy of ions. By this mechanism, the acceleration of the ions by weak presheath electric fields can heat the ions. As the velocity of ion increases, on the other hand, the polarization of neutral species does not occur and the FWHM_{||} of ion velocity distribution does not increase any more.

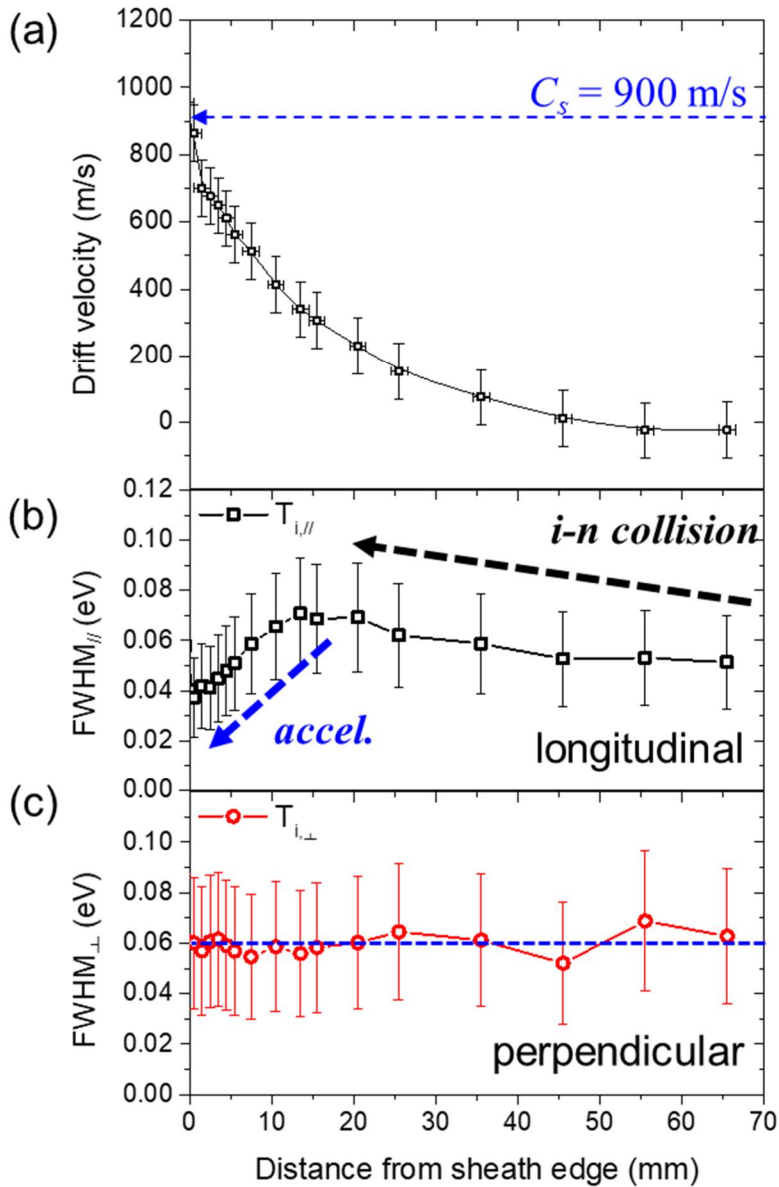


Figure 6.2. Variation of (a) ion drift velocity, (b) FWHM of IVDF in longitudinal direction, (c) FWHM of IVDF in perpendicular direction in front of DC-biased target

The decreasing of FWHM_{\parallel} at higher velocity is an intrinsic effect of the ion acceleration by the presheath electric fields. Eq. (3.1) is a collision-less Boltzmann equation (Vlasov equation) for an ion species.

$$\frac{\partial f}{\partial t} + \mathbf{v} \cdot \nabla f + \frac{eE}{m_i} \frac{\partial f}{\partial v} = 0 \quad (3.1)$$

Here, we neglect the effect of magnetic fields and collisions. By assuming 1-dimensional variation in x and v_z , Eq. (3.1) can be written as

$$\frac{\partial f}{\partial x} + \frac{eE_{pr}}{m_i} \frac{1}{v_z} \frac{\partial f}{\partial v_z} = 0 \quad (3.2)$$

As one can see in Eq. (3.2), the spatial variation of the ion velocity distribution is inversely proportional to the ion velocity at the position. That means that the population increase of higher-velocity-ions is less than the population decrease of lower-velocity-ions. This fact corresponds to the fact that velocity increase of higher-velocity-ions is smaller than lower-velocity-ions for the same amount of energy gain from the field. Thus, the acceleration by the presheath electric fields can sharpen the ion velocity distribution and make FWHM_{\parallel} smaller. Because this effect is proportional to the intensity of the electric fields, as the ions traverse toward the sheath edge, the FWHM_{\parallel} continuously decreases. This is the intrinsic characteristic of the variation of the ion velocity distribution in a presheath. i.e. FWHM_{\parallel} decreases as ions approach the sheath edge in presheath.

At the same circumstance, the perpendicular (tangential direction of the target plane) FWHM_{\perp} does not vary in the whole presheath region in front of the target. This reveals that the variation of the ion velocity distribution by the acceleration of the longitudinal presheath electric fields has adiabatic property in 1-dimensional direction. This is a direct result that ends the old controversy regarding the ion flow characteristic in the presheath. [***

Riemann] For a weakly-collisional plasma, the ion flow is 1-dimensionally adiabatic, thus $\gamma=3$.

6.2. Variation of longitudinal IVDF by electrostatic wave in presheath

In section 6.1. we have observed the intrinsic effect of the presheath electric field on the evolution of the longitudinal ion velocity distribution function. Here, we will introduce the effect of longitudinal electrostatic wave on the longitudinal ion velocity distribution function in the presheath region. Figure 6.3. shows the variation of ion velocity distribution function in a presheath formed in front of the radio-frequency biased target. Experiment were carried out in an argon plasma generated in a multi-dipole plasma source. The operation pressure was $p = 0.4$ mTorr and the discharge current was $I_d = 150$ mA. The plasma density and the temperature were $n_e \sim 1.1 \times 10^9$ cm⁻³ and $T_e \sim 3$ eV, respectively and the ion plasma frequency was $f_{pi} = \omega_{pi}/2\pi = 1.1$ MHz at the given plasma condition. The Bohm velocity was 2800 m/s. In accordance with the characteristic of the damping rate, observed in section 2.3, the bias frequency of the radio-frequency electrode was set to 13.56 MHz, which is 11 times larger than the ion plasma frequency. At the frequency, the ion contribution on the damping of the electrostatic wave dominates. The Doppler-shifted phase velocity of the wave was about 500 m/s at the condition.

The results show how the damping of the electrostatic wave occurs in the presheath region. At $d = 60$ mm from the rf-biased target, shown in figure 6.3-(a), the ion velocity distribution is quite symmetrical over the velocity space. This means that the damping rate of the electrostatic wave is not large at the position. As the ions approach toward the target, at $d = 50$ mm from the target (figure 6.3-(b)) the ion velocity distribution at the velocity of Doppler-shifted phase velocity becomes flat. It is an obvious evidence that the Landau damping effect occurs there. As the ion velocity

increases the effect of the Landau damping is clearly distinguished in the ion velocity distribution function. Until the ions reach the sheath edge, at $d = 16$ mm (figure 6.4), the damping of the wave occurs continuously in the presheath.

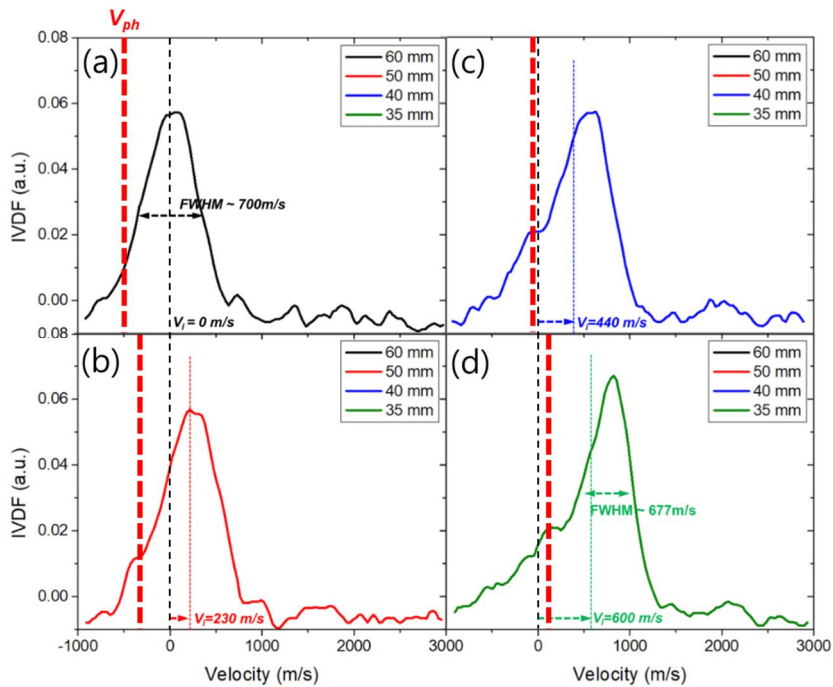


Figure 6.3. Variation of IVDF at various positions in a presheath formed in front of a rf-biased target. The Landau damping of the electrostatic wave changes the IVDF at the phase velocity of the wave.

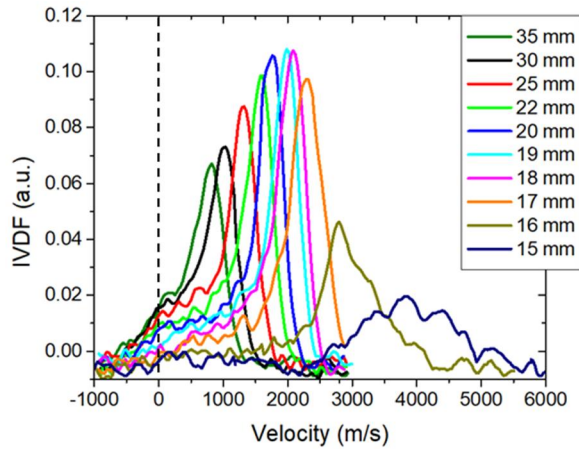


Figure 6.4. Spatial variation of the ion velocity distribution in front of the radio-frequency biased target.

While the Landau damping effectively heats up the ions, the FWHM_{\parallel} seems to continuously shrink over the whole region of the presheath because of the above-mentioned acceleration mechanism described in section 6.1. More detailed characteristics on the variation of the FWHM_{\parallel} are shown in figure 6.5. Figure 6.5. shows spatial variations of FWHM_{\parallel} in presheaths formed in front of DC (black-hollow-square) and RF (blue-hollow-circle) biased targets. The experimental conditions for the RF bias were the same to the experimental conditions of the figure 6.3 or figure 6.4. The experimental conditions for the DC bias case were $p = 0.4$ mTorr, $I_d = 150$ mA, $n_e \sim 8.4 \times 10^8 \text{ cm}^{-3}$, $T_e \sim 1.8$ eV, and $V_{DC} = -40$ V.

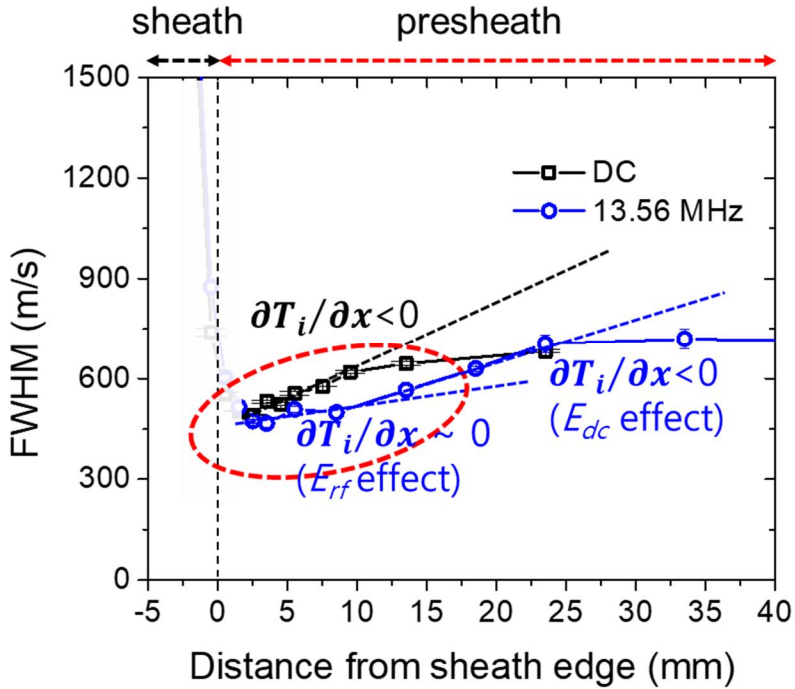


Figure 6.5. Spatial variation of full width at half maximum (FWHM) in presheaths formed in front of DC (black-hollow-square) and RF (blue-hollow-circle) biased targets.

The DC case in figure 6.5 shows a similar $\text{FWHM}_{//}$ to the variation shown in figure 6.2-(b). By the ions approaching the sheath edge, the electric field intensity increases and the $\text{FWHM}_{//}$ decreases due to the intrinsic acceleration effect on the ion velocity distribution function. However, the RF case in figure 6.5, $\text{FWHM}_{//}$ decreases far away from the sheath edge, but not near the sheath edge. Even though the time-averaged electric field becomes stronger near the sheath edge, the variation of $\text{FWHM}_{//}$ becomes weaker. This is an obvious evidence of the Landau damping effect of electrostatic wave. Because of the heating mechanism, the decrease of $\text{FWHM}_{//}$ in a presheath becomes weaker.

6.3. Characteristic of ion dynamics and electric potential in RF presheath

Figure 6.6. shows the electric potential distribution of the sheath and presheath in front of a radio-frequency biased target at various frequencies. The experiments were carried out in an argon plasma generated in the multipole plasma source with $p = 2$ mTorr, $I_d = 60$ mA, $n_e = 1.7 \times 10^9 \text{ cm}^{-3}$ and $T_e = 1.0$ eV. The radio-frequency bias voltage was, $V_{rf}^0 = 100$ V with a self-bias voltage, $V_{DC} = -100$ V. For the frequency of 13.56 MHz, the plasma density and temperature were slightly different from the other frequency conditions as $n_e = 1.5 \times 10^9 \text{ cm}^{-3}$ and $T_e = 1.86$ eV. The discharge current from a hot filament was 80 mA at that condition. The sheath-presheath boundary was defined by the position where the ion fluid velocity becomes the Bohm velocity.

In the figure it is quite interesting that the presheath potential difference is the same to $2T_e$ for all frequency conditions, which are the same result to the ion-neutral collisional presheath condition. It means that the effect of the

radio-frequency potential oscillation on the presheath does not severely change the sheath structure comparing the ion-neutral collisional sheath structure.

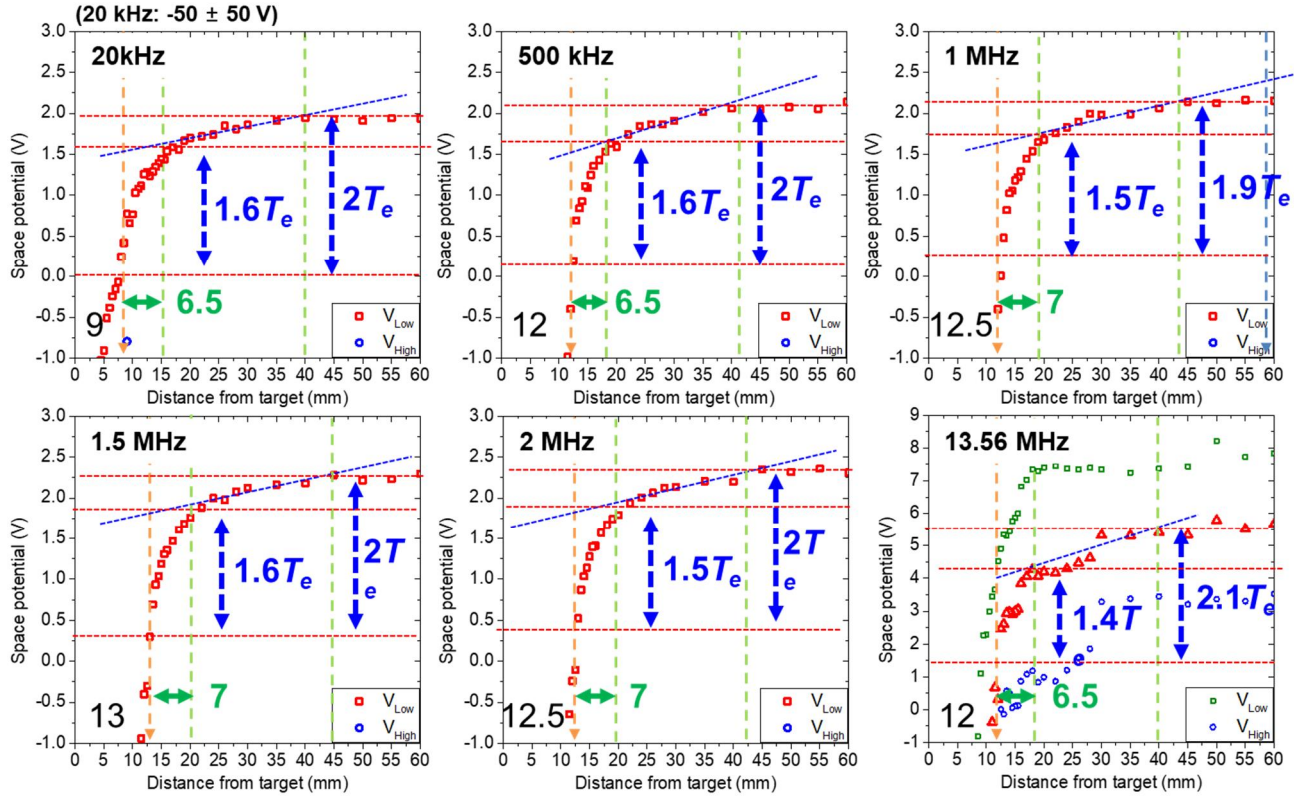


Figure 6.6. Space potential profiles versus distance from the radio-frequency biased target at various bias frequencies.

6.4. Summary

In this chapter, we have investigated the variation of the ion velocity distribution in the presheath formed in front of the DC and RF biased target. For the DC condition, an intrinsic variation of the ion velocity distribution has been found. As the ions are accelerated toward the biased target following the target electric field, the difference in the velocity gain between the faster ions and the slower ions lead the ion velocity distribution to become narrower and higher. Thus, the ion thermal temperature, which is represented as FWHM_{\parallel} , decreased while the ions traversing the presheath region. For the RF condition, it is found that the electrostatic wave could be launched from the target toward the plasma source. The phase velocity of the electrostatic wave, of which the frequency was much higher than the ion plasma frequency, was comparable to the ion thermal velocity and the wave can actively heat the ions by the mechanism of the Landau damping. It occurred in the presheath region of the RF plasmas and the decrease of the FWHM_{\parallel} , due to the time-averaged DC presheath electric field, was compensated near the sheath edge. The potential structure, however, did not changed severely from the potential structure of the DC presheath. $2T_e$ of potential difference was observed, which was the same potential drop observed in the ion-neutral collisional DC presheath of our multi-dipole plasma source. This observation is quite an important since the ion velocity distribution plays a significant role on determining the ion energy distribution at the radio-frequency biased electrode that is widely utilized in the semiconductor processing plasma source.

Chapter 7. Conclusion

For the characterization of the generalized Bohm sheath criterion derived in the section 1.4, we have investigated the characteristics of ion dynamics in presheath of collisional, magnetized and RF plasmas. The characteristics obtained from the observation of the ion motion and space potential in the presheaths of each plasma condition are summarized in table 7.1.

Table 7.1. Characteristics of ion dynamic, spatial and electric properties in presheaths of collisional, magnetized and rf plasmas.

	Ion dynamic property	Characteristic length of presheath	Potential property of presheath
ion-neutral collisional effect	• $\mathbf{R}^{i-n} = -m_i n_i v_{i-n} \mathbf{V}_i$	• $d_{pr} \sim \lambda_{mfp}$	• $\Delta\Phi_{pr,K} = 0.5 T_e = 0.5 m_i V_B^2$ • $\Delta\Phi_{pr,col} \sim T_e$ (<i>i-n</i> col.)
ion¹-ion² collisional effect	• $\mathbf{R}^{i-i'} = m_i n_i v^{i-i'} A$ $\exp(d_{TSI}/\lambda_D) \Delta V$ • $\mathbf{R}^{a-b} = -\mathbf{R}^{b-a}$	• $d_{pr} \sim \lambda_{mfp}$ • $d_{TSI} \sim \lambda_{inst}(p) < d_{pr}$	• $\Delta\Phi_{pr,K} \sim 0.5 T_e$ • $\Delta\Phi_{pr,col} \sim T_e$ (<i>i-n</i> col.) • $\Delta\Phi_{pr,col} \sim 0$ (<i>i¹-i²</i> col.)
Magnetic field effect	• 3-D motion (Accel. by $E_{pr} + \mathbf{E}_{pr} \times \mathbf{B}$)	• $d_{pr} \sim \lambda_{mfp}$ • $d_{mp} \sim r_{cs} \sin\psi < d_{pr}$	• $\Delta\Phi_{pr,K} = 0.5 T_e$ • $\Delta\Phi_{pr,col} \sim T_e$ (<i>i-n</i> col.) • $\Delta\Phi_{pr,E \times B} \sim T_e$
Ion Temperature effect	• Intrinsic change (dc) • Additional rf ion heating	• $d_{pr} \sim d_{DC/rf} \sim \lambda_{mfp}$	• $\Delta\Phi_{pr,K} = 0.5 T_e$ • $\Delta\Phi_{pr,col} \sim T_e$ (<i>i-n</i> col.) • $\Delta\Phi_{pr,Ti} \sim -T_i$ • $\Delta\Phi_{pr,Ti} \sim +T_i$ (rf heating)

The new findings in this thesis are as follows. First, the presheath potential drop in the presheath in the existence of ion-neutral collisions is found to be $2T_e$. The potential energy is consumed to compensate the kinetic loss of ions by the ion-neutral collision and to accelerate ions to reach the Bohm velocity at the sheath edge. For the variation of the pressure, however, it is found that the potential drop in the ion-neutral collisional presheath is not

changed from $2 T_e$, due to the fact that the ion-neutral collision frequency is proportional to the pressure while the total length of the presheath is inversely proportional to the pressure, thus the total collisionality is conserved. The boundary effects which might be considered when the collisional mean-free-path is much larger than the chamber dimension was also discussed.

Second, by generalizing the occurrence condition regarding the two-stream-instability between two ion species in the presheath with a consideration of ion-neutral collisions, we can observe the characteristic length scale of the two-stream-instability in the presheath. Because the collisional friction between two-ion-species is exponentially proportional to the length scale of the two-stream-instability, the instability can greatly modify the ion fluid velocities at the sheath edge from the conventional Bohm velocities. The total potential drop in the two-ion-species presheath, on the other hand, does not severely changed from $2T_e$, which is the same potential difference of the presheath under the existence of ion-neutral collisions. This is because the collisional interaction is an energy-conserving interaction that happens between two-ion-species.

Third, the effect of magnetic field on the 3-dimensional ion motion in the presheath region have been analyzed. Before the ions reaches the sheath edge with the Bohm velocity in the surface-normal direction, the $E \times B$ drift occurs in the presheath region and an additional presheath potential is needed to form the drift velocity. Unlike the previous studies which classifies the presheath region into the two-uniquely defined region, the collisional and magnetic presheath, it is found that the presheath cannot be separated into two regions but forms a unified region in which the collision and $E \times B$ motion co-exist.

Forth, it is found that the ion velocity distribution can be changed actively by the acceleration effect of the presheath electric field. As the ions are accelerated by the presheath electric field, the ion velocity distribution becomes narrower because of the increase of the velocity per the same potential difference is smaller for faster ions than slower ions. In this study,

we have firstly observed that the electrostatic waves launched by a radio-frequency biased target can actively heat ion in the presheath though the Landau damping mechanism. Thus, the heating effect by the Landau damping of the wave prevents the ion velocity distribution to become much narrower at the sheath edge.

In table 7.2, the scale laws for the characterization of the generalized Bohm criterion are summarized. Each term regarding the ion dynamic effect are compared to the electric field intensity at the sheath edge. The electric field at the sheath edge is assumed to be an order of T_e/l_{De} [Godyak ***].

On the right column in the table, the ratios are calculated for the plasma conditions of each experiment. By the results, only the ion-ion collision between two different ion species is revealed to have a considerable effect on the sheath edge condition, thus, the ion velocities of each ion species at the sheath edge could be modified.

Table 7.2. Scale laws for characterization of the generalized Bohm criterion by ion dynamic properties.

	Scale laws for effect of ion dynamics	Scaling (Exp. Condition)
ion-neutral collisional effect	• $\frac{R_{S,x}}{E_x} \sim \frac{e\lambda_D}{k_B T_e} \frac{R_{i-n,x}}{en_i} \sim \frac{e\lambda_D}{k_B T_e} \frac{m_i n_i (n_0 \sigma_{i-n} V_i)}{en_i} = \lambda_D n_0 \sigma_{i-n} = \frac{\lambda_D}{\lambda_{i-n}}$	10 ⁻³ Conventional Bohm velocity
ion¹-ion² collisional effect	• $\frac{R_{i-i,x}}{E_x} \sim \frac{\lambda_D}{T_e} \frac{R_{i-i,x}}{en_i} \sim \frac{e\lambda_D}{k_B T_e} \frac{m_i n_i v_{i-i} A \exp(\lambda_{TSI}/\lambda_D) \Delta V}{en_i}, \text{ for } \gamma_{TSI} > v_{i-n}$	1 Modification on ion velocity
Magnetic field effect	• $\frac{q_s n_s (\mathbf{V}_s \times \mathbf{B})_x}{E_x} \frac{e\lambda_D}{k_B T_e} (\mathbf{V}_i \times \mathbf{B})_x = \frac{\lambda_D}{T_e} V_z B \sin\psi \sim \frac{e\lambda_D}{k_B T_e} C_s B \sin\psi \sim \frac{\lambda_D}{r_{cs}} \sin\psi$	10 ⁻² Conventional Bohm velocity
Temperature effect	• $\frac{\lambda_D}{T_e} \frac{\partial T_i}{\partial x}, \frac{\lambda_D}{T_e} \frac{1}{en_i} \frac{\partial \pi_{i,xx}}{\partial x} \sim -\frac{\lambda_D}{T_e} \frac{T_i}{\lambda_{pr}}$ (DC) • $\frac{\lambda_D}{T_e} \frac{\partial T_i}{\partial x}, \frac{\lambda_D}{T_e} \frac{1}{en_i} \frac{\partial \pi_{i,xx}}{\partial x} \sim +\frac{\lambda_D}{T_e} \frac{T_i}{\lambda_{pr}}$ (additional RF)	10 ⁻⁵ Conventional Bohm velocity

From the investigation, the generalized Bohm criterion at the sheath edge, which is originate from the breaking condition of the quasi-neutrality can be extended to include ion dynamic characteristics in the presheath. This form of the generalized Bohm criterion is more robust than the former forms of the generalized Bohm criterions in that the ion dynamic effects under the magnetic fields and oscillating electric fields are included. The characteristic of ion dynamics in presheath were investigated under the existence of ion-neutral collisions, ion-ion collisions between two different ion species, external magnetic field with oblique geometrical angle and the radio-frequency electric fields. By considering the ion dynamic characteristics, the generalized Bohm criterion can be qualitatively analyzed. The analysis reveals that for the highly collisional, strongly magnetized, or highly damped plasma the ion velocity at the sheath edge must be different from the conventional Bohm velocity. The potential drop in the presheath of those plasmas provides kinetic energy for ions to satisfy the generalized Bohm sheath criterion at the sheath edge. Additional potential energy is found to be needed to compensate the ion dynamic effects. Therefore, the presheath potential is found to be the summation of the kinetic energy of ions at the sheath edge of $\sim 0.5T_e$ and the ion-dynamic-governing portion of the specific conditions of \sim few T_e .

Bibliography

- [1] K.-U. Riemann, Review article: The Bohm criterion and sheath formation, *J. Phys. D: Appl. Phys.* **24**, 492-518 (1991).
- [2] D. Bohm, Chapter 3 in *The Characteristics of Electrical Discharges in Magnetic fields*, edited by A. Guthrie and R.K. Wakerling (New York: McGraw-Hill, 1949).
- [3] K.-U. Riemann, The Bohm criterion and boundary conditions for a multicomponent system, *IEEE Trans. Plasma Sci.* **23**(4), 709 (1995).
- [4] K.-U. Riemann, The Bohm criterion and sheath formation, *J. Phys. D: Appl. Phys.* **24** (1991).
- [5] K.-U. Riemann, Plasma and sheath, *Plasma Source Sci. Technol.* **18**, 014006 (2009).
- [6] S.D. Baalrud and C.C. Hegna, Kinetic theory of the presheath and the Bohm criterion, *Plasma Sources Sci. Technol.* **20**, 025013 (2011).
- [7] S.D. Baalrud and C.C. Hegna, Reply to comment on ‘Kinetic theory of the presheath and the Bohm criterion’, *Plasma Sources Sci. Technol.* **21**, 068002 (2012).
- [8] R. N. Franklin, The plasma–sheath and its stability in a quiescent plasma containing two species of positive ion, *J. Phys. D: Appl. Phys.* **36**, 1806 (2003).
- [9] J.T. Gudmundsson and M.A. Lieberman, Ar⁺ and Xe⁺ velocities near the Presheath-Sheath Boundary in an Discharge, *Phys. Rev. Lett.* **107**, 045002 (2011).
- [10] G.D. Severn, X. Wang, E. Ko, and N. Hershkowitz, Experimental studies of the Bohm criterion in a two-ion-species plasma using laser-induced fluorescence, *Phys. Rev. Lett.* **90**(14), 0145001 (2003).
- [11] D. Lee, G. Severn, L. Oksuz, and N. Hershkowitz, Laser-induced fluorescence measurements of argon ion velocities near the sheath boundary

- of an argon–xenon plasma, *J. Phys. D: Appl. Phys.* **39**, 5230 (2006).
- [12] D. Lee, N. Hershkowitz, and G.D. Severn, Measurements of Ar⁺ and Xe⁺ velocities near the sheath boundary of Ar–Xe plasma using two diode lasers, *Appl. Phys. Lett.* **91**, 041505 (2007).
- [13] S.D. Baalrud, C.C. Hegna, and J.D. Callen, Instability-enhanced collisional friction can determine the Bohm criterion in multiple-ion-species plasmas, *Phys. Rev. Lett.* **103**, 205002 (2009).
- [14] S.D. Baalrud and C.C. Hegna, Determining the Bohm criterion in plasmas with two ion species, *Phys. Plasmas* **18**, 023505 (2011).
- [15] S.D. Baalrud, T. Lafleur, W. Fox, and K. Germaschewski, Instability-enhanced friction in the presheath of two-ion-species plasmas, *Plasma Sources Sci. Technol.* **24**, 015034 (2015).
- [16] C.-S. Yip and N. Hershkowitz, Experimental test of instability-enhanced collisional friction for determining ion loss in two ion species plasmas, *Phys. Rev. Lett.* **104**, 225003 (2010).
- [17] N. Hershkowitz, C.-S. Yip and G. Severn, Experimental test of instability enhanced collisional friction for determining ion loss in two ion species plasmas, *Phys. Plasmas* **18**, 057102 (2011).
- [18] S.D. Baalrud, Influence of ion streaming instabilities on transport near plasma boundaries, *Plasma Sources Sci. Technol.* **25**, 025008 (2016).
- [19] M. Rosenberg, Ion–dust streaming instability in processing plasmas, *J. Vac. Sci. Technol. A* **14**(2), 631 (1996).
- [20] J.W. Sheldon, Correlation of Resonance Charge Exchange Cross-Section Data in the Low-Energy Range, *Phys. Rev. Lett.* **8**(2), 64 (1962).
- [21] M. A. Lieberman and A. J. Lichtenberg, Principles of Plasma Discharges and Materials Processing, 2nd ed., John Wiley & Sons, Hoboken (2005).
- [22] H. Gokan and S. Esho, Pattern fabrication by oblique incidence ionbeam etching, *J. Vac. Sci. Technol.*, **18**(1), 23 (1981).

- [23] T. Ono, M. Ono, K. Shibata, T. Kenmotsu, Z. Li, and T. Kawamura, Calculation of sputtering yield with obliquely incident light-ions (H^+ , D^+ , T^+ , He^+) and its representation by an extended semi-empirical formula, National Institute for Fusion Science, Toki, (2012).
- [24] W. Eckstein and J.P. Biersack, Reflection of heavy ions, *Z. Phys. B - Condensed Matter* **63**, 471 (1986)
- [25] R. Chodura, Numerical analysis of plasma-wall interaction for an oblique magnetic field, *J. Nucl. Mater.* **111&112**, 420 (1982).
- [26] R. Chodura, Plasma-wall transition in an oblique magnetic field, *Phys. Fluids* **25**(9), 1628 (1982).
- [27] Chodura R. Plasma flow in the sheath and the presheath of a scrape-off layer. In: Post D.E., Behrisch R. (eds) *Physics of Plasma-Wall Interactions in Controlled Fusion*. Springer, Boston, MA (1986).
- [28] K.-U. Riemann, Theory of the plasma–sheath transition in an oblique magnetic field, *Contrib. Plasma Phys.* **34**(2-3), 127 (1994).
- [29] K.-U. Riemann, Theory of the collisional presheath in an oblique magnetic field, *Phys. Plasmas* **1**(3), 552 (1994).
- [30] E. Ahedo, Structure of the plasma-wall interaction in an oblique magnetic field, *Phys. Plasmas* **4**(12), 4419 (1997).
- [31] G.-H. Kim, N. Hershkowitz, D.A. Diebold, and M.-H. Cho, Magnetic and collisional effects on presheaths, *Phys. Plasmas* **2**(8), 3222 (1995).
- [32] M.U. Siddiqui, C.D. Jackson, J.F. Kim, and N. Hershkowitz, Direct measurements of ion dynamics in collisional magnetic presheaths, *Phys. Plasmas* **21**(10), 102013 (2014).
- [33] M.U. Siddiqui, D.S. Thompson, C.D. Jackson, J.F. Kim, N. Hershkowitz, and E.E. Scime, Models, assumptions, and experimental tests of flows near boundaries in magnetized plasmas, *Phys. Plasmas* **23**(5), 057101 (2016).
- [34] M.A. Lieberman, Analytical solution for capacitive RF sheath, *IEEE Trans. Plasma Sci.* **16**(6), 638 (1988).

- [35] E. Kawamura, V. Vahedi, M.A. Lieberman and C.K. Birdsall, Review article: Ion energy distributions in rf sheath; review, analysis and simulation, *Plasma Sources Sci. Technol.* **8**, R45–R64 (1999)
- [36] M.M. Turner and P. Chabert, A radio-frequency sheath model for complex waveforms, *Appl. Phys. Lett.* **104**, 164102 (2014)
- [37] R. Limpaechar and K.R. MacKenzie, Magnetic Multipole Containment of Large Uniform Collisionless Plasmas, *Rev. Sci. Instrum.* **44** (1973)
- [38] K.N. Leung, T.K. Samec and A. Laam, Optimization of permanent magnet plasma confinement, *Phys. Lett.* **51A** (1975)
- [39] K. N. Leung, N. Hershkowitz and K. R. MacKenzie, Plasma Confinement by Localized Cusps, *Phys. Fluids* **19** (1976)
- [40] M.H. Cho and N. Hershkowitz, Particle and power balance of hot-filament discharge plasma in multidipole device, *J. Appl. Phys.* **67**, 3254 (1990)
- [41] M. A. Lieberman and A. J. Lichtenberg, Principles of Plasma Discharges and Materials Processing, 2nd ed. (John Wiley & Sons, Hoboken, 2005)
- [42] S.-R. Huh, N.-K. Kim, B.-K. Jung, K.-J. Chung, Y.-S. Hwang, and G.-H. Kim, Global model analysis of negative ion generation in low-pressure inductively coupled hydrogen plasmas with bi-Maxwellian electron energy distributions, *Phys. Plasmas* **22**(3), 033506 (2015).
- [43] J. R. Smith, N. Hershkowitz, and P. Coakley, Inflection point method of interpreting emissive probe characteristics, *Rev. of Sci. Instrum.* **50** (1979).
- [44] T. Lho, N. Hershkowitz and G.-H. Kim, Effect of harmonic rf fields on the emissive probe characteristics, *Rev. Sci. Instrum.* **72** (2000)
- [45] J. M. Sanders, A. R. Rauch, R. J. Mendelsberg and A. Anders, A synchronized emissive probe for time-resolved plasma potential measurements of pulsed discharges, *Rev. Sci. Instrum.* **82** (2011)
- [46] R. Schrittwieser, J. Adamek, P. Balan, M. Hron, C. Ionita, K. Jakubka,

- L. Kryska, E. Martines, J. Stockel, M. Tichyy and G. V. Oost, Measurements with an emissive probe in the CASTOR tokamak, *Plasma Phys. Control. Fusion* **44** (2002)
- [47] D. S. Lee, Y. H. Ting, L. Oksuz and N. Hershkowitz, Measurement of plasma potential fluctuations by emissive probes in CF₄ radio-frequency plasma, *Plasma Sources Sci. Technol.* **15** (2006)
- [48] E. H. Wilson, Jongtae Jeong, and N. Hershkowitz, An emissive probe with a rhenium filament for measuring plasma potential in a radio frequency oxygen plasma, *Rev. Sci. Instrum.* **73** (2002)
- [49] M. H. Cho, C. Chan, N. Hershkowitz, and T. Intrator, Measurement of vacuum space potential by an emissive probe, *Rev. Sci. Instrum.* **55** (1984)
- [50] D. Diebold, N. Hershkowitz, A. D. Bailey III, M. H. Cho and T. Intrator, Emissive probe current bias method of measuring dc vacuum potential, *Rev. Sci. Instrum.* **59** (1988)
- [51] N. Hershkowitz, Sheath: More complicated than you think, *Phys. Plasmas* **12** (2005).
- [52] N. Hershkowitz, How Langmuir Probe Works, in *Plasma Diagnostics, Discharge Parameters and Chemistry*, edited by O. Auciello and D. L. Flamm, Vol. 1, Chap. 3, Academic, Boston (1989).
- [53] J. P. Sheehan and N. Hershkowitz, Emissive probes, *Plasma Source Sci. Technol.* **20** (2011).
- [54] J. P. Sheehan, Y. Raitses, N. Hershkowitz, I. Kaganovich, and N. J. Fisch, A comparison of emissive probe techniques for electric potential measurements in a complex plasma, *Phys. Plasmas* **18** (2011).
- [55] X. Wang and N. Hershkowitz, Simple way to determine the edge of an electron-free sheath with an emissive probe, *Rev. Sci. Instrum.* **77** 043507 (2006)
- [56] K.N. Leung, T.K. Samec and A. Laam, Optimization of permanent magnet plasma confinement, *Phys. Lett.* **51A** (1975)
- [57] G. D. Severn, D. A. Edrich and R. McWilliams, Argon ion laser-

- induced fluorescence with diode lasers, *Rev. Sci. Instrum.* **69** (1998)
- [58] M. J. Geockner, J. Goree and T. E. Sheridan, Laser-induced fluorescence characterization of a multidipole filament plasma, *Phys. Fluids B* **3** (1991)
- [59] M. J. Geockner, J. Goree and T. E. Sheridan, Saturation broadening of laser-induced fluorescence from plasma ions, *Rev. Sci. Instrum.* **64** (1993).
- [60] R.L. Merlino, Understanding Langmuir probe current-voltage characteristics, *Am. J. Phys.* **75** (2007)
- [61] M. Balden and J. Roth, New weight-loss measurements of the chemical erosion yields of carbon materials under hydrogen ion bombardment, *J. Nucl. Mater.* **280**, 39 (2000).
- [62] P. Sigmund, A mechanism of surface micro-roughening by ion bombardment, *J. Mater. Sci.* **8**, 1545 (1973).
- [63] E.A. Eklund, E.J. Snyder, and R.S. Williams, Correlation from randomness: quantitative analysis of ion-etched graphite surfaces using the scanning tunneling microscope, *Surf. Sci.* **285**, 157 (1993).
- [64] Q. Yang, T. Hamilton, C. Xiao, A. Hirose and A. Moewes, Plasma-enhanced synthesis of diamond nanocone film, *Thin Solid Films* **494**, 110 (2006).
- [65] Q. Wang, et al., General fabrication of ordered nanocone array by one-step selective plasma etching, *Nanotechnology* **25**, 115301 (2014).
- [66] I. Alexeff and W. D. Jones, Collisionless ion-wave propagation and the determination of the compression coefficient of plasma electrons, *Phys. Rev. Lett.* **15** (1965)
- [67] K. Lonngren, D. Montgomery, I. Alexeff and W. D. Jones, Dispersion of ion-acoustic waves, *Phys. Lett.* **25** (1967)
- [68] I. Alexeff and W. D. Jones, Excitation of pseudowaves in a plasma via a grid, *Phys. Rev. Lett.* **21** (1968)
- [69] T. Christensen, N. Hershkowitz, A. Scheller and K. E. Lonngren, Antenna properties of probes used in ion-acoustic wave experiments, *Radio*

Science, **12** (1977)

[70] W. Gekelman *et al.*, Ion acoustic wave experiments in a high school plasma physics laboratory, *Am. J. Phys.* **75** (2007)

[71] A. M. Hala and N. Hershkowitz, Ion acoustic wave velocity measurement of the concentration of two ion species in a multi-dipole plasma, *Rev. Sci. Instrum.* **72** (2001)

[72] N. Hershkowitz and Y. Kim, Probing plasmas with ion acoustic waves, *Plasma Sources Sci. Technol.* **18**, 014018 (2009)

[73] N. Hershkowitz, How Langmuir Probe Works, in *Plasma Diagnostics, Discharge Parameters and Chemistry*, edited by O. Auciello and D. L. Flamm, Vol. 1, Chap. 3, Academic, Boston (1989)

초 록

충돌성, 자화, RF 플라즈마에 대한 일반화된 Bohm 쉬스 경계조건 해석

김 남 균

서울대학교 대학원

에너지 시스템 공학부

본 연구에서는 충돌성, 자화, RF 플라즈마에서의 일반화된 Bohm 쉬스 경계조건 해석을 수행한다. 준중성의 플라즈마와 맞닿는 거의 모든 경계면에서는 강한 전기장의 플라즈마 쉬스 공간이 형성된다. 쉬스 내부의 강한 전기장은 플라즈마로부터 벽면 방향으로 형성되며, 전자의 손실을 지연시키고 이온의 유입을 증가시킴으로써 준중성의 플라즈마 물성이 유지되도록 기여한다. 쉬스 공간이 형성되기 위한 조건으로서 Bohm 은 쉬스 경계에서의 이온의 속도가 $V_{Bohm} = \sqrt{k_B T_e / m_i}$ 이상이 되어야 함을 주장하였으며, 해당 경계 조건은 플라즈마의 생성 및 소멸과 플라즈마를 활용하는 모든 응용 분야에서 널리 사용되고 있다. 이 쉬스 경계조건을 Bohm 조건이라 부른다. 그러나 해당 경계조건은 비충돌성, 단일이온 및 단일전하 조건, 자기장이 없는 이상화된 조건에서 유도가 되었다는

문제점이 있다. 실제로 지구상에서 생성되고 사용되는 거의 모든 플라즈마에 대해서는 위의 이상적 가정이 적용되기가 어렵다는 한계를 가진다. 본 연구에서는 플라즈마 조건에 대한 위의 이상적 가정을 적용하지 않은 일반화된 Bohm 쉬스 경계조건을 얻는다. 이는 이온과 중성기체 종간의 충돌, 서로 다른 이온종 간의 충돌, 비스듬한 임의의 각도를 가지는 자기장의 존재 및 이온의 속도 분포의 변화 등 기존에 무시되었던 가정들에 대한 일반화를 수행하고 이온 거동에 대하여 일반화된 Bohm 쉬스 경계조건을 구한다. 방법으로는 이온 거동에 관한 일반적 지배 방정식인 Boltzmann 방정식의 fluid moment 방정식을 활용한다. 새로이 구한 쉬스 경계 조건의 특징을 조사하기 위해 이온과 중성종, 이온과 이온의 충돌이 존재하는 경우, 비스듬한 자기장이 존재하는 경우, 및 이온 속도 분포의 변화를 유도할 수 있는 라디오 주파수의 전기장이 주어지는 경우에 대하여 쉬스 경계 근방 프리쉬스 영역에서의 이온 거동 특징 및 이온 거동에 에너지를 공급하는 프리쉬스 영역의 전위 구조 특징을 관찰한다. 이온의 움직임은 레이저-유도-형광 기법을 이용하여 측정하며, 전위 구조는 전자방출 정전탐침을 이용하여 측정한다. 실험 관찰을 통해 밝혀진 이온 거동의 특징과 쉬스 경계의 조건을 만족시키기 위해 이온을 가속하는 프리쉬스 공간의 특징을 활용하여 본 연구에서의 일반화된 Bohm 쉬스 경계조건의 특징을 정성적으로 해석한다. 본 연구의 해석 결과는 고충돌성, 고자화, 고전력의 RF 조건의 플라즈마에서 쉬스가 형성되기 위해서는 쉬스 경계에서의 이온의 속도가 기존 Bohm 속도가 아닌 수정된 Bohm 속도를 가져야 함을 함축한다.

주요어: 일반화된 봄 조건, 플라즈마 쉬스, 프리쉬스, 충돌성, 자화, 라디오주파수 전기장

학 번: 2013-30993

